Chem Soc Rev

Amorphous Inorganic Semiconductors for the Development of Solar Cell, Photoelectrochemical and Photocatalytic Applications

Journal:	*Chemical Society Reviews*
Manuscript ID	CS-SYN-08-2020-001134.R2
Article Type:	Review Article
Date Submitted by the Author:	17-Mar-2021
Complete List of Authors:	Wang, Bing; Nanjing University, Biesold-Mcgee, Gill; Georgia Institute of Technology, Materials Science and Engineering Zhang, Meng; Georgia Institute of Technology, Materials Science and Engineering; Shandong University, Energy and Power Engineering Lin, Zhiqun; Georgia Institute of Technology, Materials Science and Engineering

SCHOLARONE™
Manuscripts

Amorphous Inorganic Semiconductors for the Development of Solar Cell, Photoelectrocatalytic and Photocatalytic Applications

Bing Wang,[a,b#] Gill M. Biesold,[a#] Meng Zhang,[a] Zhiqun Lin[a*]

[a]School of Materials Science and Engineering, Georgia Institute of Technology, Atlanta GA 30332, USA.

[b]Eco-materials and Renewable Energy Research Center, National Laboratory of Solid State Microstructures, School of Physics, Nanjing University, Nanjing 210093, People's Republic of China.

#: equal contribution

*: corresponding author; email: zhiqun.lin@mse.gatech.edu

Abstract

Amorphous inorganic semiconductors have attracted growing interest due to their unique electrical and optical properties that arise from their intrinsic disordered structure and thermodynamic metastability. Recently, amorphous inorganic semiconductors have been applied in a variety of new technologies, including solar cells, photoelectrocatalysis, and photocatalysis. It has been reported that amorphous phases can improve both efficiency and stability in these applications. While these phenomena are well established, their mechanisms have long remained unclear. This review first introduces the general background of amorphous inorganic semiconductor properties and synthesis. Then, the recent successes and current challenges of amorphous inorganic semiconductor-based materials for applications in solar cells, photoelectrocatalysis, and photocatalysis are addressed. In particular, we discuss the mechanisms behind the remarkable performances of amorphous inorganic semiconductor in these fields. Finally, we provide insightful perspectives into further developments for applications of amorphous inorganic semiconductors.

1. Introduction

The design of advanced semiconductors is critical to meet the increasing demands for enhanced performance needed in a variety of future technologies. Although most studies have scrutinized the properties of crystalline semiconductors, there is growing interest in exploring amorphous semiconductors.[1-5] The intrinsic disordered structure and thermodynamic metastability of amorphous semiconductors enable unique physical attributes which make them an intriguing material with diverse applications in solar energy conversion,[1, 6] photocatalysis,[7-9] and photoelectrocatalysis.[3, 10-12] The coordination of constituent atoms in amorphous semiconductors deviates from that of crystalline phases (8 valence electrons rule), which can induce higher surface energy and provide more active sites.[13] The compositions in amorphous phase can be tuned over a wider range, which holds promise for adjusting electronic structures and further designing appropriate active centers. The relatively smoother surfaces and reduced grain boundaries of amorphous semiconductors have been found to better facilitate electron transfer.[7, 14] Due to their chemical homogeneity, amorphous materials lack grain boundaries, dislocations and other defects that easily trigger chemical corrosion, enabling the growth of a protective layer to retard ionic transport.[15] The improved corrosion resistance of amorphous phases make them excellent candidates for use in photoconversion devices or photochemical reactions. In addition, amorphous semiconductors are usually prepared under mild conditions without annealing or sintering, which can reduce their production cost. The unique electrical and optical properties of amorphous inorganic semiconductors, which have a great impact on their performance in solar cell, photoelectrocatalysis and photocatalysis, are briefly introduced

below.

1.1 Electrical Properties

Band tail states are localized electronic states near the valence and conduction band edges that are induced by the disorder structure (or defects like impurities or vacancies) of semiconductors and play an important role in the electrical properties of amorphous semiconductors (**Fig. 1**).[16] The boundary that separates delocalized states from an exponential distribution of localized band tail states is called the mobility edge. According to the band theory of solids, all states of a periodic crystal are delocalized because the electrons in these states have an equal probability of being found near each equivalent atom.[17] In amorphous semiconductors, however, band tails have an enhanced impact because of the increase in localized states from the lack of periodicity of the disordered structures. The state density determines the electrical properties of an amorphous semiconductor. While electrons in the band tail states do not have significant mobilities, they are primarily responsible for electrical conductivity because these electrons can easily be excited into a high-mobility (conduction band) state by very small amounts of additional energy, easily supplied by the thermal lattice vibrations.[17] Generally there are two type of conduction in amorphous semiconductors, band conduction in delocalized states and hopping conduction tunneling between localized states or between localized and delocalized state.

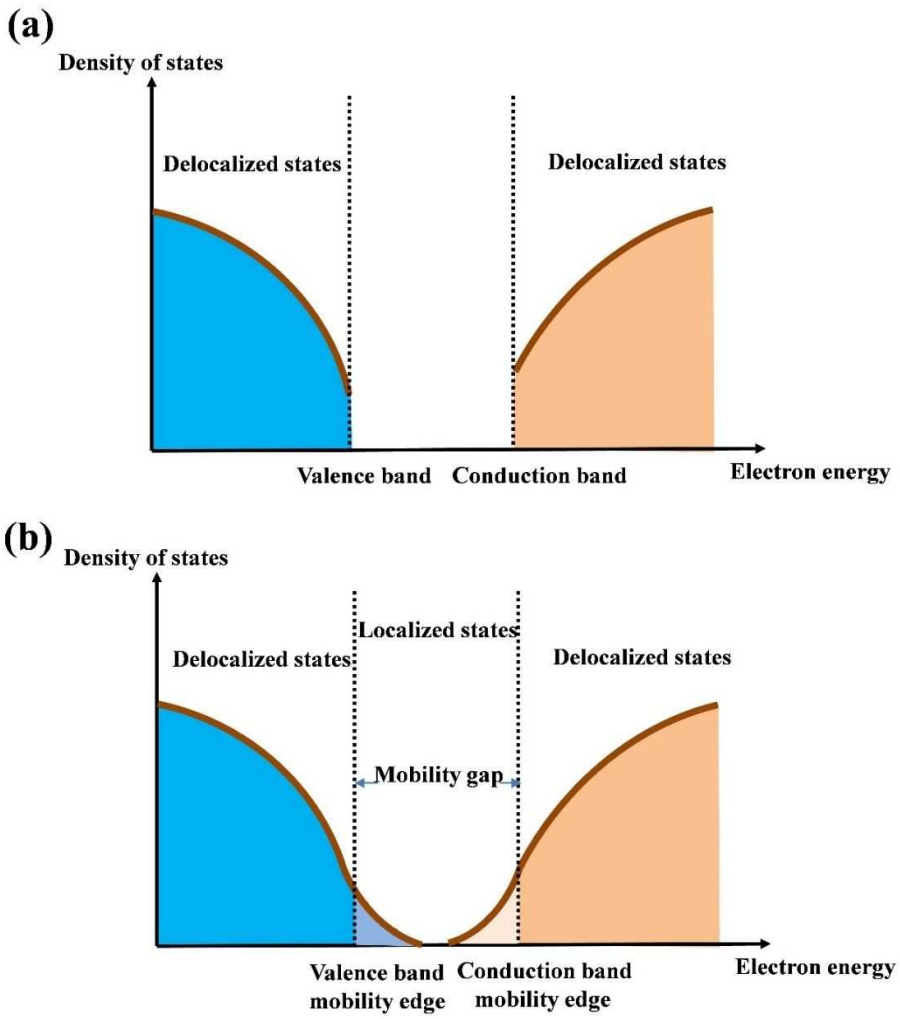

Fig. 1 Schematic density of states diagrams for (a) Crystalline semiconductors and (b) amorphous semiconductors.

Recent reports have revealed that amorphous TiO_2 might actually be more advantageous due to its electric "leakiness".[3, 18] The formation of oxygen vacancies and the reduction of Ti^{4+} cations to Ti^{3+} in amorphous TiO_2 were found to enhance conductivity via n-type doping. This doping has been observed to increase photocurrent by suppressing tunneling barriers and decrease the required overpotential for oxidation-reduction reactions.[19, 20] These distinct

electrical properties have allowed amorphous TiO_2 to be successfully used in various solar-energy-conversion devices[3, 21, 22] and as an interlayer or active component in photocatalytic reactions.[5, 23-26]

1.2 Optical Band Gap

Optical absorption and luminescence in amorphous semiconductors occur by the transition of electrons and holes between electronic states, including valence and conduction bands, tail states, and gap states. There are three distinct regions of optical absorption of amorphous semiconductors. The first is the high absorption region (absorption coefficiency: $\alpha \geq 10^4$ cm^{-1}) which is governed by the optical band gap between the valence band and conduction band. The second is the Urbach's exponential tail region (with $\alpha = 10^2$–10^4 cm^{-1}), which is governed by the optical transitions from localized tail states above the valence band to delocalized states in the conduction band and/or from the delocalized states in the valence band to localized states below the conduction band. The third is the low energy absorption region ($\alpha \leq 10^2$ cm^{-1}) that follows Tauc's relation and is governed by the optical transitions from one delocalized state to another delocalized state. Optical absorptions in the latter two regions appear at energies lower than the optical gap, and thus the electronic states of the band tail in amorphous semiconductors may contribute to the optical absorption in the visible range.[27]

In addition, electron-phonon coupling, which is a mediator of light-induced structural changes in semiconductors, has a great impact on the optical responses of materials to light and

charge-carrier dynamics[28] and is significantly larger for localized states than for delocalized states. Thus, amorphous semiconductors have a stronger photo-response due to their larger electron-phonon coupling that more strongly modulates light energy.[29, 30]

Based on the unique electrical and optical properties of amorphous semiconductors, this review summarizes the recent advances and current challenges in amorphous inorganic semiconductor materials, with a particular emphasis the fundamental properties and mechanisms of amorphous TiO_2-based materials and their applications in solar cells, photoelectrocatalysis, and photocatalysis. We hope to provide insightful perspectives on further developments for future applications of amorphous inorganic semiconductors. Notably, the electron energy in vacuum is usually used as a reference in solar cells, whereas the normal hydrogen electrode (NHE) scale is traditionally adopted in photoelectrocatalysis. As shown in **Fig. 2**, NHE lies at -4.5 eV with respect to the absolute vacuum scale, and we can convert these two energy scales *via* the equation: $E_{Vac} = -4.5-E_{NHE}$.

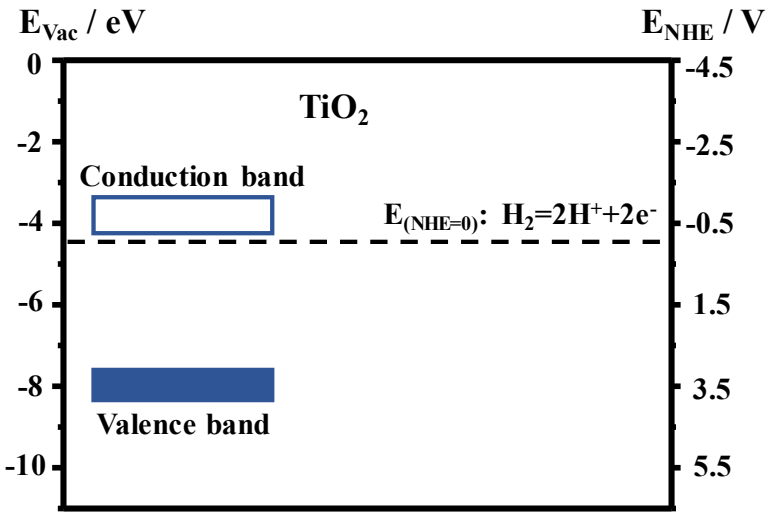

Fig. 2 TiO_2 energy level alignment on the vacuum energy scale and NHE scale.

2. Synthesis of Amorphous Inorganic Semiconductors and Black TiO_2

2.1 Synthesis of Amorphous Inorganic Semiconductors

2.1.1 Atomic Layer Deposition

Atomic layer deposition (ALD) is a vapor phase technique used in industrial semiconductor device fabrication to produce a variety of large-scale thin films.[31] Generally, the ALD process consists of sequentially alternating pulses of gaseous chemical precursors that react with a substrate until an appropriate film thickness is achieved. ALD processes are typically conducted at modest temperatures below 350°C,[32] but amorphous TiO_2 layers with uniform coverage have been obtained at much lower temperatures (~60 °C).[33] A wide range of amorphous semiconductor materials have been grown via ALD in previous studies.[3, 12, 18, 23, 34-36] Compared with chemical vapor deposition (CVD) and various physical vapor deposition (PVD) techniques, ALD offers superior control over the morphology, thickness, and composition of amorphous semiconductor materials. Depositing an amorphous thin film by ALD on a substrate with nano-sized roughness has been reported to increase surface smoothness.[37] Increased surface smoothness has been found to result in an increased Schottky barrier height due to decreased surface state density,[38] which reduces leakage current across the interface.[37] This stands in sharp contrast to thicker films which typically have a rougher surface and thus a reduced Schottky barrier height. For example, when ALD fabricated amorphous SnO_2 was used as the electron transport layer in perovskite solar cells, almost no

hysteresis was observed. This lack of hysteresis may be attributed to the smooth SnO_2 layer, which reduced charge trapping centers and increased the Schottky barriers at the atomic-layer-deposited SnO_2/perovskite interface.[1,39] In addition to their smoothness, amorphous ALD semiconductor films possess a low leakage current because they lack grain boundaries that act as sinks, sources for impurities, and sites for non-uniform charge conduction.[40] Many ALD-prepared amorphous inorganic semiconductors like ZnO[41] and TiO_2[42] have shown good density, smoothness, and low leakage current, making them good candidates for high performance solar-energy-conversion devices. However, ALD is a high-cost technique due to its low material utilization efficiency. It is reported that approximately 60% of precursor dosage is wasted in the ALD process.[43] Moreover, the requirement of vacuum conditions further increases the cost. Another drawback of ALD is its time-consuming operation due to the low deposition rate. However, this challenge can be partially overcome by using spatial atmospheric ALD.[44]

2.1.2 Reactive Magnetron Sputtering

Reactive magnetron sputtering (RMS) is another technique that can easily form thin compound semiconductor films via the sputtering of metallic targets in the presence of a reactive gas.[10, 45, 46] It is widely applicable for the fabrication of many kinds of semiconductors, including nitrides, oxides, and carbides. For example, amorphous carbon nitride, a well-known hard coating material, has been successfully prepared on both ultrathin Si and SiO_2 substrates by RMS using a graphite target and pure nitrogen gas.[47-49] However, the deposition rate of

compound semiconductor films drops abruptly when the reactive gas flowrate is increased. To synthesize high-quality amorphous semiconductor films using RMS, it is imperative to maintain precise control over the preparation parameters.

To date, RMS has been employed to deposit amorphous layers for solar cells and other optical components.[50] For example, amorphous chromium oxide (Cr_2O_3), a hole transporting layer (HTL) for organic solar cells, was synthesized by RMS on FTO-coated glass substrates.[46] The optical properties (e.g. transmittance, band gap energy, etc.) and electrical resistivity of the Cr_2O_3 film were found to be critically dependent on the RMS preparation conditions. A 10 nm thick Cr_2O_3 film (deposited at a temperature of 473 K with an oxygen flow ratio of 40%) showed the best performance as a solar cell HTL due to the increased p-type conductivity and optimized band-energy structure of Cr_2O_3 for hole-transport and electron blocking.[46] A thicker Cr_2O_3 layer was found to increase the series resistance and hinder carrier transport, while thinner ones induced larger leakage current. Another study looked at photoanodes made from Cr and N co-doped amorphous $Ti(Cr)O_{2-x}$:N thin films created in a mixed gas atmosphere containing nitrogen, argon, and oxygen at constant total pressure of 0.69 Pa.[51] The amorphous $Ti(Cr)O_{2-x}$:N exhibited a sufficient flat band potential, high width of the depletion layer at the electrode/electrolyte interface, and good performance for hydrogen production due to its appropriate electronic structure and morphology.[51] Additionally, an amorphous carbon nitride film with a graded band gap structure was created by controlling the substrate temperature from 450 ^{o}C to 600 ^{o}C.[49] Such a graded band energy structure was found to absorb a wider range of solar energy than a single band gap.[49] Notably, low temperature RMS-deposited films generally

contain defects and pinholes. To create high quality amorphous films without these defects, the films should either be made sufficiently thick or treated at proper processing temperatures.[10]

2.1.3 Electrochemical Deposition

Electrochemical deposition is a widely used technique to fabricate coatings. Electrochemical deposition can achieve extremely thin films (as small as a few nanometers thick). It has been widely adopted in nanotechnology due to its relatively low energy needs and ability to shape materials into three-dimensional geometries.[52, 53] Electrochemical deposition also creates strong bonds between materials, bestowing the final product with impressive durability.[52] Amorphous TiO_2 was electrodeposited on $W:BiVO_4/F:SnO_2$ to block undesired back reduction of photo-oxidized intermediates on the conductive substrate and improve the photoelectrocatalytic performance of the photoanode toward the oxidation of water.[52] The optimal thickness of amorphous TiO_2 overlayers was determined to be 80-120 nm, formed from 15-30 s of electrodeposition. Despite not being photoactive, the amorphous TiO_2 layer was observed to simultaneously provide sufficient surface coverage and minimize resistance to charge transfer to the solution.[52] Amorphous iron sulfide thin films were deposited with ZnO using the electrochemical deposition method. [54] 0.5 μm-thick iron sulfide films were formed with a deposition time of 3 min and a deposition potential of -1.0 V vs SCE. The heterojunction of ZnO and iron sulfide showed clear rectification properties and light responsivity.[54] Thin amorphous WO_3 films were also successfully prepared by sol-gel electrogalvanostatic deposition, which may be very promising for applications in optical devices.[55] It is notable that

electrodeposition of the W- or Mo- containing solutions generally requires a solute prepared by oxidative 'dissolution' of powdered metal in H_2O_2.[56] One drawback of the electrodeposition method is its tendency towards the non-uniform thickness of coatings.[57] Electrodeposited coatings tend to be thickest near the anode, with a gradual decrease as distance from the anode increases.

2.1.4 Chemical Bath Deposition

Chemical bath deposition (CBD) has been widely used as a simple and convenient process for the large-area deposition of many semiconductors.[1, 58, 59] Amorphous films can be fabricated by CBD without the need for annealing or sintering. The morphology of the final products can be controlled via tuning the concentration of precursors, solution temperature and pH, and deposition time. For example, amorphous TiO_2 films with thickness ranging from 40~190 nm were crafted from titanium and stoichiometric oxygen by varying the deposition time from 1 h to 12 h at pH=2.2.[60] As the deposition time increased from 0.5 h to 8 h, the film surface was observed to roughen.[60] Notably, homogeneous films were observed with a deposition time of 2 h. Recently, an amorphous SnO_2 electron transport layer (ETLs) for perovskite solar cells was prepared by CBD at a very low temperature (55 °C) using a simple nontoxic aqueous bath of tin chloride. The energy-level alignment between the SnO_2 and the perovskite light absorber facilitated easy electron extraction and effectively blocked hole transport.[1] Amorphous MoS_2 thin films made using ammonium tetrathiomolybdate as a single source precursor for Mo and S and hydrazine hydrate as the reducing agent were deposited on glass and quartz substrates

by CBD at 60°C and pH=10. The deposited film showed good adherence to the substrate and excellent transmission in the visible range.[61] It is worth noting that the thickness of films grown from CBD is limited due to the solution supersaturation phenomenon.[62] This problem can, however, be addressed by performing the synthesis process in several runs.[63]

2.1.5 Chemical Vapor Deposition

Chemical vapor deposition (CVD) is a technique in which a thin film is produced by chemical reactions on the surface of a substrate using one or more gaseous compounds or elements containing thin film elements. It involves the dissociation and/or chemical reactions of gaseous reactants in an activated (heat, light, plasma) environment, followed by the formation of a stable solid product.[64] A unique feature of CVD over other deposition techniques is its ability to coat components with complex geometries. Both ALD and CVD can provide precise control over doping and laminate formation as interlayers in devices. The versatility of CVD has led to its rapid growth for a wide range of applications, such as semiconductor-based devices for optoelectronics and energy conversion. CVD can create uniform and conformal amorphous semiconductor films with high chemical purity on substrates by optimizing deposition rates and temperatures.[65, 66] However, when the surface reactions become faster, non-uniform films with pinholes and resistive grain boundaries can also easily form. The optical and electrical properties of CVD semiconductor films depend strongly on the deposition rate and time (or film thickness).[67] It is important to control the deposition parameters for optimal properties.[68] An inherent drawback of the CVD process is its need to use high temperatures, which limits

possible substrates to only those which can survive such high temperature environments. This problem can be addressed by coupling plasma, which can trigger chemical reactions at relatively low-temperatures, allowing for synthesis of thin films.[69] Amorphous semiconductor structures allow the formation of films at low substrate temperatures where the low mobility of the reactive species is achieved to prevent species migration into more energetic sites for crystal nucleation. Amorphous Bi_2S_3 films were synthesized by room temperature CVD and used as an electron transport layer in hybrid perovskite solar cells.[65] The process was free of solvents, which minimized the potential for contamination. The obtained film was smooth and compact without pinholes or cracks, which enabled a conformal encapsulation of the hybrid perovskite. Thin (12~36 nm) and conformal TiO_2 amorphous interlayers with few pinholes were fabricated by CVD and used as electron collection contacts in inverted bulk heterojunction organic photovoltaics.[68] Notably, it is difficult to deposit multicomponent materials by CVD method due to the different vaporization rates of multiple precursors.

2.2 Synthesis of Black TiO_2

The wide band gap of crystalline TiO_2 (3.0 eV for rutile and 3.2 eV for anatase) allows it to absorb light only in the ultraviolet region. Very recently, introducing midgap states via disorder engineering has been proposed as a method to enhance the absorption efficiency of TiO_2 in the visible and near-infrared range.[70] A hydrogen-doped TiO_2 (TiO_2:H) crystalline core/amorphous shell structure with black color (black TiO_2) has triggered a surge of interest due to its high absorption in the visible and near-infrared wavelengths and its excellent

conductivity.[12, 45, 71] In contract to the synthesis methods of amorphous semiconductors summarized in section 2.1, the reported methods for preparing hydrogenated amorphous-based TiO_2:H focuses mainly on hydrogen thermal treatment,[72, 73] hydrogen plasma,[74] chemical reduction,[73] and electrochemical reduction.[73] Hydrogenation treatment induces oxygen vacancies on the surface that create localized states in the bandgap. These localized states have observed to shift the bandgap of TiO_2:H to around 1.5 eV, with an optical onset around 1.0 eV.[75] Hydrogen thermal treatment is a simple and straightforward process in which TiO_2 is annealed in a H_2 atmosphere to reduce Ti^{4+} to Ti^{3+}. Hydrogenated black TiO_2:H can also be made in a thermal plasma furnace by inductively coupled hydrogen plasma at specific temperatures.[76] Strong reductants such as $NaHB_4$,[77] CaH_2,[78] Zinc powder,[79] and Aluminum[25] can also be used to craft TiO_2:H by creating disorder surfaces. Hydrogenated black TiO_2:H nanotubes with tens of well-defined layers with long-range structural periodicity and visible light responsive bandgaps have been made using electrochemical deposition.[80] Depending on the synthetic methods, Ti^{3+} ions, oxygen vacancies, Ti-OH or Ti-H bonds can be observed experimentally, all of which could act as active sites in the applications of black TiO_2.[81, 82] The performance of black TiO_2:H in solar cell, photoelectrocatalytic and photocatalytic reactions will be discussed in the following sections.

3. Amorphous Inorganic Semiconductors for Solar Cells

The new generation of solar cells includes perovskite solar cells (PSCs), dye sensitized solar cells (DSSCs), organic solar cells (OSCs), and quantum-dot sensitized solar cells

(QSSCs).[83] Compared to conventional silicon solar cells these new cells are attractive due to their lower cost, thinner nature, and ability to be used in various lighting conditions. Nevertheless, several challenges remain to be addressed regarding the efficiency and stability of these new solar cells. To address these issues, numerous attempts have been made to incorporate amorphous semiconductors such as TiO_2[21] and SnO_2[1] into these devices due to the distinct electrical and optical properties of amorphous materials.

3.1 Perovskite Solar Cells

A typical PSC is an all-solid-state device that utilizes a bulk heterojunction architecture comprised of a perovskite absorber layer sandwiched between an electron transporting layer (ETL) and hole transporting layer (HTL) to create an n-i-p junction. The ETL, which is usually made of materials ranging from metal-oxide semiconductors to fullerene-based polymers, plays a vital role in PSC device performance. It not only extracts and transports photogenerated electrons from the perovskite to the electrodes, but it also blocks holes to suppress charge recombination. Crystalline compact TiO_2 is the most common choice for ETL in PSCs, but its necessary high-temperature processing (generally above 500 °C) significantly decreases its compatibility with substrates and the perovskite absorber, both of which have lower thermal budgets than crystalline TiO_2.[36, 84, 85] Furthermore, typical fabrication approaches of the crystalline TiO_2 compact layer (e.g. spin-coating or spray pyrolysis) result in numerous pinholes and grain boundaries, which can lead to deleterious direct contact between the perovskite absorber and electrodes. Using a low-temperature-processed amorphous compact

layer instead of a crystalline one provides an intriguing route to prevent devices from forming grain-induced inhomogeneities and diffusion pathways. [36, 65, 84-88] Table 1 summarizes the performance of PSCs using low-temperature-processed amorphous semiconductor as the ETLs, which will be discussed in detail in this section. Martinson et al. utilized thermal ALD to synthesize pinhole-free amorphous TiO_2 compact layers at or below 120 °C using tetrakis-(dimethylamino)titanium and H_2O as precursors.[36] The 12 nm thick films were then employed as ETLs in planar PSCs (**Fig. 3a**). In order to eliminate the negative effects of carbon impurities (i.e. organic remnants from the low temperature thermal ALD process may serve as charge recombination centers at the interface between ETLs and perovskite absorber) on the performance of PSCs, as-deposited TiO_2 ETLs were post-treated with ultraviolet-ozone (UV-O_3). For comparison, anatase compact TiO_2 layers (annealed at 500 °C) were also synthesized. The amorphous TiO_2 with post-treatment of UV-O_3 and the annealed anatase resulted in similarly improved performance of the devices (**Fig. 3 c** and **3d**, respectively).[36] The crystallization-free improvement to short-circuit current (J_{sc}) and fill factor (FF) from room temperature UV-O_3 treatment was attributed to the removal of some defects that can cause deep level states (**Fig. 3b**) and then result in carrier recombination. Our group further proved that samples treated with O_3 plasma treatment can retain bulk vacancies while effectively eliminating surface vacancies, which act as surface trap sites that facilitate charge carrier recombination.[6]

Table 1 The best photovoltaic parameters of PSCs with amorphous inorganic semiconductors

as ETLs.

ETLs	V_{oc} (V)	J_{sc} (mA·cm^{-2})	FF (%)	PCE (%)	Ref.
TiO_2 NPs	0.82	10.0	21.8	1.8	36
TiO_2 NPs	0.91	22.6	66.0	13.7	88
TiO_2 NPs	1.02	24.6	71.0	17.8	6
TiO_2 NPs with UV-O_3 treatment	0.86	25.6	45.2	10.0	36
TiO_2 NWs	0.96	20.7	74.0	14.7	84
Nd-doped TiO_2	1.08	23.9	74.0	19.0	87
WO_x	0.71	21.8	58.0	9.0	85
WO_x	1.06	24.8	79.1	20.8	89
WO_x/TiO_x	0.89	23.1	71.0	14.5	90
WO_x/C_{60}	0.93	22.2	78.0	16.1	91
SnO_2	1.05	21.3	66.3	14.8	1
SnO_2	1.17	23.9	76.5	21.4	92
SnO_x	1.05	22.8	66.2	15.8	93
Nb_2O_5	1.04	22.9	72.0	17.1	94
NbO_x	1.12	22.42	76.0	19.1	95
$InGaZnO_4$	1.14	22.7	66.8	17.4	96
$ZnSnO_4$	1.04	24.7	78.0	20.0	97
NbOH	1.16	23.0	79.0	21.1	98
Bi_2S_3	0.95	18.6	74.2	13.1	65

Note: NPs: nanoparticles; NWs: nanowires; V_{oc}: open-circuit voltage; J_{sc}: short circuit current; FF: fill factor; PCE: photoelectric conversion efficiency.

Higher average oxidation states on the surface of amorphous TiO_2 have been shown to significant enhance the performance of PSC.[36] This conclusion was verified by Caruso et al.

who used amorphous TiO_2 nanowires as the ETL in PSCs.[84] PSCs made with these hydrothermal amorphous TiO_2 yielded a stabilized PCE of approximately 14%, which is comparable to that of high-temperature annealed analogues.[84] The porous hydrothermal TiO_2 nanowire network was found to both form a larger interfacial contact area for effective electron extraction and provide a direct pathway for better electron transport and charge collection.[99]

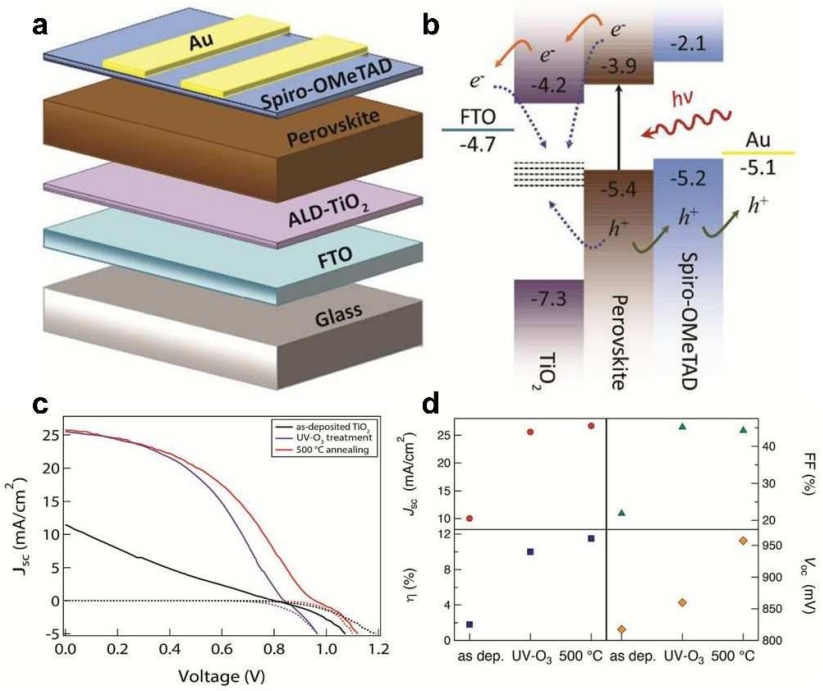

Fig. 3 (a) Device structure of a planar PSC and (b) the corresponding energy level diagram. (c) J-V characteristics of the PSC with TiO_2 ETLs post-treated under various conditions. Dotted lines represent curves obtained in the dark. (d) Characteristic properties of PSCs as a function of post-treatment on TiO_2 ETLs. Reproduced from ref. 36 with permission from American Chemical Society, copyright 2016.

In addition to TiO_2, tungsten oxides (WO_x) have also been recognized as another attractive candidate for efficient ETLs in PSCs due to their chemical stability, good light transmittance, wide band gaps (2 to 3 eV) and high electron mobility (10-20 $cm^2 \cdot V^{-1} \cdot s^{-1}$).[100, 101] Low temperature-processed amorphous WO_x ETLs in PSCs have also been reported.[85, 90, 91] To improve the intrinsically high charge recombination and relatively lower (to TiO_2) Fermi level of pure WO_x (which can result in low V_{oc} and FF,[90, 91, 102]), WO_x-based amorphous composites such as WO_x-TiO_x (**Fig. 4a**)[90] and WO_x/C_{60} thin films [91] were fabricated. The addition of TiO_x into WO_x has been shown to raise the Fermi level and suppress charge recombination due to optimal band energy alignment.[90] The WO_x-TiO_x composite ETLs showed favorable optical characteristics as more than 90% of the photons from 400 nm to 1000 nm were permitted to pass through.[90] Compared with amorphous and crystalline TiO_2 ETLs, these composite ETLs can more easily extract photo-generated electrons due to their enhanced electrical conductivity of the WOx-TiOx . A notable increase in photovoltaic performance was observed in PSCs made with the amorphous WO_x-TiO_x composite ETL, as evidenced by their constant photocurrent of 20.00 mA cm^{-2} and a PCE of 11.9% for 2000 seconds in an ambient atmosphere and under a bias voltage of 0.6 V, as shown in **Fig. 4b**.[90] A fullerene (e.g. C_{60}) layer is commonly used as an ETL because of its excellent electron mobility (1.6 $cm^2 \cdot V \cdot s^{-1}$) and conductivity ($2.3 \times 10^{-3}$ $S \cdot cm^{-1}$). Additionally, fullerene has been shown to passivate grain boundaries, suppress the ion migration in perovskite,[91, 103-105] and reduce trap state density and hysteresis of PSCs.[106, 107] Adding C_{60} to the WO_x resulted in ETLs with better electron extraction and transfer between the perovskite and WO_x layer, both of which were attributed

to optimized energy-level alignment (**Fig. 4c**) and superior electrical contact. As a result, amorphous WO_x/C_{60} ETL-based devices showed superior performance to that of WO_x ETL-based devices (**Fig. 4d**).[91]

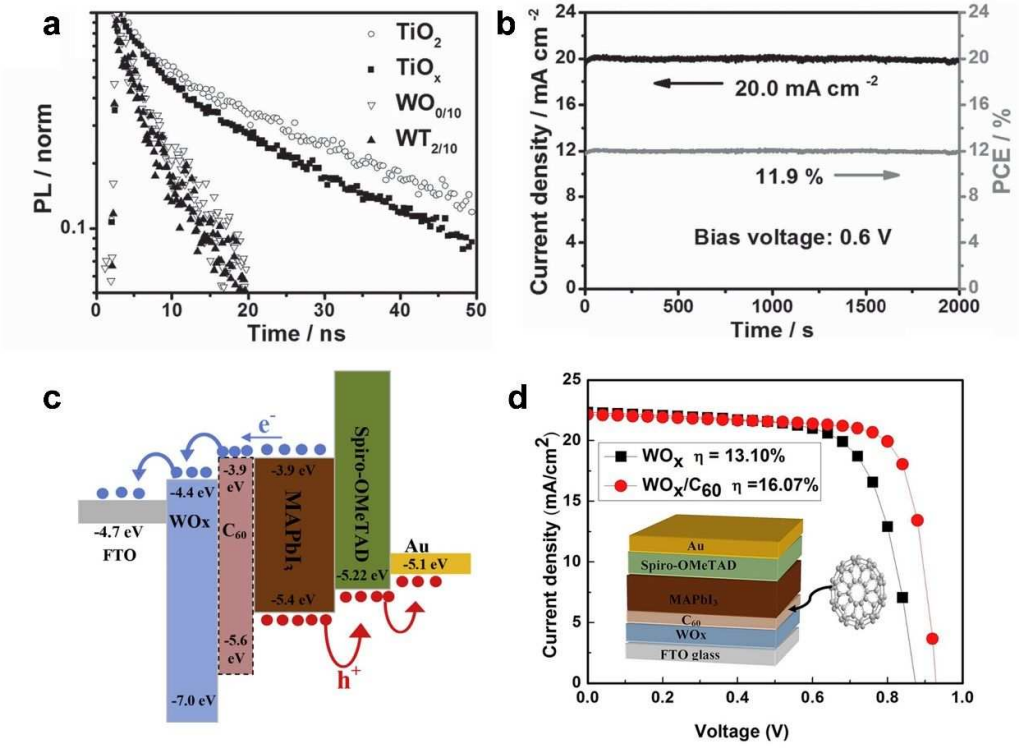

Fig. 4 (a) Time-resolved photoluminescence measurements on samples with the device architecture of FTO/different ETL/$CH_3NH_3PbI_3$. The legend TiO_2, TiO_x, $WO_{0/10}$,$WT_{2/10}$ represent crystalline TiO_2, amorphous TiO_2, pure amorphous WO_x, and amorphous WO_x-TiO_x with the molar ratios of titanium to tungsten 2/10, respectively; (b) Steady power conversion efficiency (PCE) and current output for the PSCs based on $WT_{2/10}$ as the ETL. Reproduced from ref. 90 with permission from John Wiley and Sons, copyright 2015. (c) Energy band diagram of planar WO_x/C_{60} ETL-based PSC; (d) J-V curves of WO_x and WO_x/C_{60} ETL-based

devices. Reproduced from ref. 91 with permission from Elsevier, copyright 2017.

Tin oxide (SnO_2) has also attracted significant interest as an alternative ETL in PSCs recently due to its higher band gap (~3.7 eV), high electron mobility (100~200 $cm^2 \cdot V^{-1} \cdot s^{-1}$), deeper valence-band maximum, and stability.[73, 108, 109] Efficiencies greater than 22% have been reported for PSCs with SnO_2 ETLs.[110, 111] However, most of the reported works have utilized crystalline SnO_2 films with tetragonal rutile structures that need to be annealing at 180-200°C,[112] and studies using amorphous SnO_2 ETLs prepared at low-temperatures are still limited. Tietze and Gobbo et al. synthesized amorphous SnO_2 (**Fig. 5a**) by a one-step CBD method at low temperature without an annealing process.[1] The amorphous SnO_2 ETLs were resistant to UV radiation and moisture, and thus were less susceptible to surface chemical and energetic alterations.[1] The amorphous SnO_2-based films were able to be stored for several days in air without any moisture or UV degradation. Efficient electron transfer from perovskite to the amorphous SnO_2 ETLs was achieved by optimizing the energy-level alignment via the following device structure: ITO/amorphous SnO_2/$CH_3NH_3PbI_3$/spiro-OMeTAD (Full name of spiro-OMeTAD is 2,2',7,7'-Tetrakis[N,N-di(4-methoxyphenyl)amino]-9,9'-spirobifluorene, **Fig. 5b**). Although the CBD-processed SnO_2 showed lower electron mobility (1.5×10^{-8} $cm^2 \cdot V^{-1} \cdot s^{-1}$) than its crystalline counterparts, the favorable band alignment between the amorphous SnO_2 ETLs and the perovskite absorber overcame the potential resistive losses.[1] Compared to the crystalline TiO_2- or SnO_2-based references, amorphous SnO_2-based devices displayed improved performance (**Fig. 5c**) due to their higher transmittance in the UV and visible

ranges.[93] A planar $(FAPbI_3)_{0.85}(MAPbBr_3)_{0.15}$-based ($MA=CH_3NH_3^+$; $FA= CH(NH2)^{2+}$) perovskite solar cell employing low-temperature processed amorphous SnO_x as the ETL showed a PCE up to 15.8% with a V_{OC} of 1.05 V.[93] However, the device was reported to have strong hysteresis effects due to charge accumulation in trap states at the SnO_2 ETL/perovskite interface[113] and the low conductivity of SnO_2.[93, 114-116] Fullerenes have been used to passivate defects that originate from grain boundaries in the perovskite film.[104, 117] [6,6]-phenyl-C_{60}-butyric acid methyl ester ($PC_{60}BM$) was introduced as an interlayer at the amorphous SnO_2 ETL/perovskite interface to passivate both the surface trap states and perovskite grain boundaries. In addition, such an interlayer can prevent the migration of I^- in the perovskite film which was found to reduce hysteresis in SnO_2 ETL-based PSC devices.[1] Recently, Yang et al. found that an ethylene diamine tetra-acetic acid (EDTA)-complexed amorphous SnO_2 (E-SnO_2) electron-transport layer in PSCs can also effectively suppress hysteresis and achieve a record efficiency of 21.60% (**Fig. 5d**).[118] Adding EDTA was found to enhance the hydrophilicity of the E-SnO_2 surface which decreased the Gibbs free energy favoring heterogeneous nucleation of the perovskite film, leading to better crystallinity, full surface coverage, and increased grain size.[118]

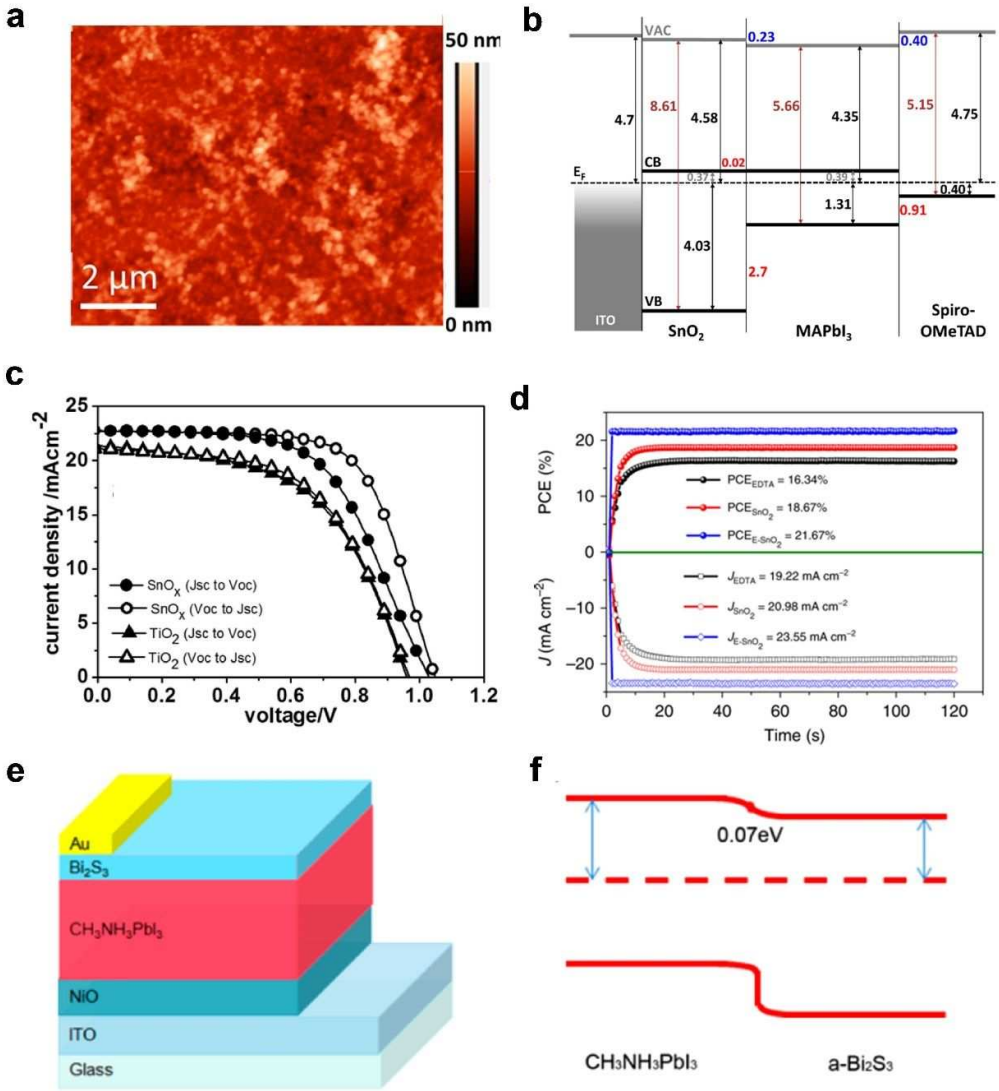

Fig. 5 (a) 10×10 μm^2 AFM image of amorphous SnO_2 on ITO; (b) The corresponding energy-level diagram of the ITO/amorphous SnO_2/perovskite/spiro-OMeTAD device architecture. Reproduced from ref. 1 with permission from American Chemical Society, copyright 2017. (c) J-V curves of the best-performing PSCs with amorphous SnO_2 or compact TiO_2 as ETLs and mixed $(FAPbI_3)_{0.85}(MAPbBr_3)_{0.15}$ perovskite as the photoactive layer, respectively. Reproduced from ref. 93 with permission from The Chemical Society of Japan, copyright 2017.

(d) Current density and PCE measured as a function of time for the EDTA, SnO_2, and E-SnO_2-incorporated devices biased at 0.85 V, 0.89 V, and 0.92 V, respectively. Reproduced from ref. 118 with permission from Springer Nature, copyright 2018. (e) Schematic demonstration of the inverted ITO/NiO/$CH_3NH_3PbI_3$/amorphous Bi_2S_3/Au device, and (f) band diagram of $CH_3NH_3PbI_3$/amorphous Bi_2S_3 devices. Reproduced from ref. 65 with permission from American Chemical Society, copyright 2016.

Tang et al. introduced an amorphous bismuth trisulfide (Bi_2S_3) ETL into inverted hybrid PSCs (**Fig. 5e**).[65] Bi_2S_3 was chosen because of its intrinsically higher electron concentration and carrier mobility (257 $cm^2 \cdot V^{-1} \cdot s^{-1}$) and its better hydrophobic nature relative to the traditional $PC_{61}BM$ ETL.[119-121] In contrast to other amorphous inorganic semiconductor films with numerous defects (such as vacancies and dangling bonds), because amorphous Bi_2S_3 is composed of one-dimensional $(Bi_4S_6)_n$ ribbons stacked together through van der Waals forces, amorphous Bi_2S_3 possesses few dangling bonds and low defect density.[122] As shown in **Fig. 5f**, there is a 0.07 eV conduction band offset between the perovskite absorber and the amorphous Bi_2S_3 ETLs, enabling efficient separation of photogenerated carriers.[65, 123] Simultaneously, such a small interfacial energy barrier between perovskite and amorphous Bi_2S_3 was found to suppress charge trapping and interface accumulation, which resulted in reduced scanning hysteresis of the devices.[65] Additionally, the good conductivity of Bi_2S_3 and the efficient charge separation at the amorphous Bi_2S_3/perovskite interface enabled comparable performance between amorphous Bi_2S_3 ETL-based devices and $PC_{61}BM$ ETL-based devices.

Improved humidity and photo stabilities of the devices with the amorphous Bi_2S_3 as ETLs were also observed and attributed to its hydrophobic nature and high light stability.[65]

3.2 Organic Solar Cells

Organic solar cells (OSCs) are generally constructed similarly to PSCs, with the following layers: a conductive transparent glass or plastic substrate, a hole-collection interlayer (cathode buffer layer), an active absorber layer (conjugated polymers), a thin electron conducting layer (anode buffer layer), and a reactive metal top contact.[68, 124] In a typical structure, indium tin oxide (ITO) is widely used as the transparent conducting anode, poly(3,4-ethylenedioxythiophene)-poly(styrene sulfonate) (PEDOT:PSS) is the electron blocking layer, lithium fluoride (LiF) is the hole blocking layer, and aluminum (Al) is used as the anode (**Fig. 6a**).[125-127] Notably, inverted OSCs usually place a hole blocking layer (e.g. ZnO) between the ITO and the active layer, and an electron blocking layer (e.g. PEDOT:PSS) is deposited on top of the active layer, as shown in **Fig. 6b**.[128] Both the conventional and inverted structures require proper energy level alignment and a low work function metal electrode for electron extraction.[124] Although currently the PCE of OSCs lags behind that of inorganic solar cells,[129] OSCs hold promise due to their lightweight and flexible nature and their possibility for low-cost high-throughput roll-to-roll processing.[130] Stability of OSCs has been reported as a key challenge towards their widespread application.[31, 131, 132] PEDOT:PSS has been found to undergo fast degradation because of its acidic nature.[133] Photodegradation of polymers at the indium tin oxide (ITO) and the metal electrodes has also been reported, and was attributed to

reactions with oxygen and water.[128] Thus, it is currently a challenge to achieve OSCs with high performance and superior stability. To address these issues, amorphous inorganic semiconductors have been applied in OSCs, example of which will be discussed individually.

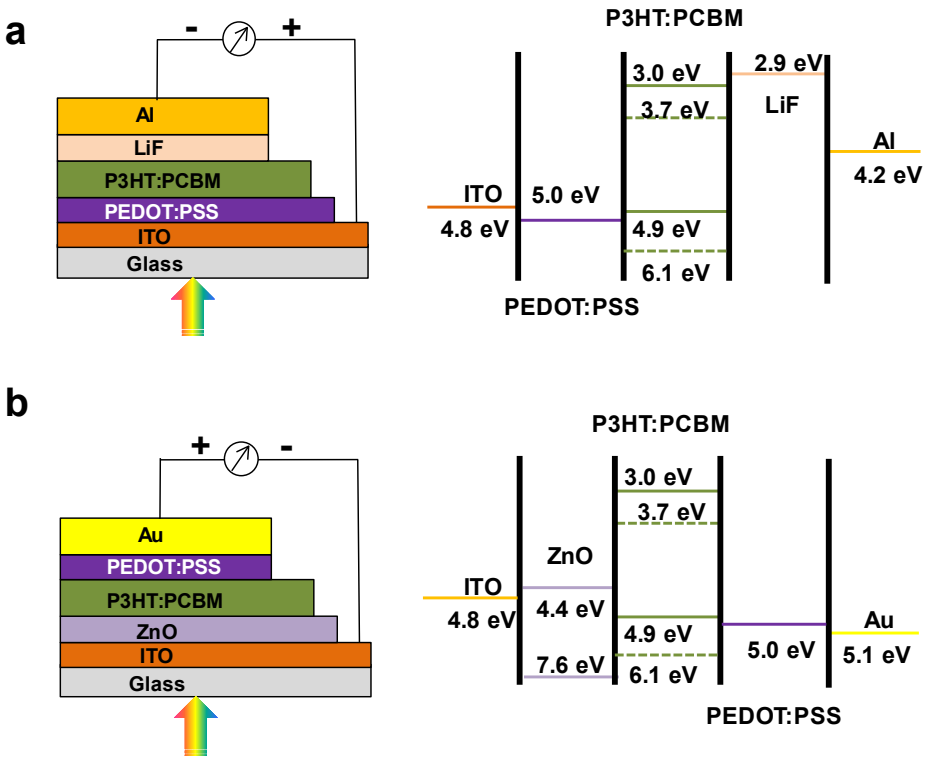

Fig. 6 Schematic and energy band structures of (a) a regular and (b) an inverted organic solar cell (OSC).

3.2.1 Amorphous Electrodes

ITO, a transparent conducting oxide, is one of the most commonly used transparent electrodes due to its excellent electrical and optical properties and environmental stability. However, its mechanical flexibility is limited because of cracks formed at grain boundaries which increase sheet resistance and deteriorates electrical performance of the film. Hence,

more suitable flexible transparent electrodes are urgently needed to realize flexible OSCs. Amorphous transparent electrodes, which can be synthesized at low temperatures, possess superior flexibility and promise to be a viable alternative to conventional ITO.[134, 135] Although partially replacing In and Sn in ITO with Zn, Cd, and Si has been reported to produce promising cost-efficient amorphous electrodes for use in OSCs,[136-140] it is desirable to explore In-free multilayer electrodes with low sheet resistance and high transparency comparable to those of crystalline ITO electrodes due to the scarcity and high cost of indium. A structure of amorphous $ZnSnO_3$ /Ag/ amorphous $ZnSnO_3$ (ZTO/Ag/ZTO) with a nano-scale Ag layer sandwiched between two amorphous ZTO layers was used as an alternative electrode in inverted OSCs.[141] Due to its low sheet resistance and high optical transmittance, the OSC devices made using ZTO/Ag/ZTO electrodes displayed comparable PCE to that of an ITO cell.[141] Additionally, OSCs made with amorphous ZnO/Ag/ZnO electrodes were found to possess power conversion efficiencies 20% higher than that of indium tin oxide electrodes.[142] The enhanced performance was attributed to the low sheet resistance and high optical transmittance of ZnO/Ag/ZnO electrodes in the visible region. No significant degradation in the performance of the OPVs was measured after 400 cycles of continuous bending, which demonstrated the superior mechanical stability of OPVs made with the amorphous ZnO/Ag/ZnO.[142] Nevertheless, the studies on the OSCs with amorphous In-free electrodes are still rare and need to be further explored for cost-efficient devices.

3.2.2 Amorphous Electron Collection Interlayer

Insertion of interfacial layers between electron transport layers and organic semiconductors can significantly improve the performance of OSCs. In order to integrate new generations of photoactive materials into OSCs, the energy level difference between the electrodes and organic components must be incrementally tuned.[143] TiO_2 is usually used as an electron-selective interlayer in OSCs because its conduction band energy level is suitable to harvest electrons and its valence band energy is large enough to block holes and suppress surface recombination.[144, 145] Optimal energy level alignment can be achieved by implementing an amorphous electron-selective TiO_2 interlayer film in the inverted bulk poly(3-hexylthiophene):[6,6]-phenyl-C_{61}-butyric acid methyl ester (P3HT:$PC_{61}BM$) configuration OSCs, as shown in **Fig. 7a**. An amorphous TiO_2 interlayer prepared by CVD was found to possess a low concentration of the defects and suppress carrier recombination, especially near the maximum power point.[68] Regardless of the thickness of the TiO_2 layer, devices made with the amorphous film exhibited higher FF, V_{OC}, J_{SC}, and overall performance compared to OSCs made with bare ITO (**Fig. 7b**).[68] Amorphous TiO_2 was also prepared using CBD, and the resulting film was used as an electron collection layer/hole blocking layer between ITO and PCBM:P3HT in inverted OSCs.[146] The amorphous titanium interlayers were synthesized with various stabilizers (e.g. ethanolamine, diethanolamine, or acetyl acetone). The stabilizers used in TiO_x formation played a key role in reducing resistance in the bulk and at the TiO_x/conjugated polymer interface.[146] The PCE of OSC with ethanolamine-stabilized TiO_x was observed to be 2.5 times higher than that without the TiO_x layer (**Fig. 7c**).[146] The relatively efficient charge transport of electrons was ascribed to the superior conduction properties of

TiO_x.[147, 148] Inverted OSCs with amorphous TiO_x showed high durability due to the protection of the PCBM:P3HT blend from photo-degradation, which occurs *via* permeation of oxygen and moisture. The amorphous TiO_x inhibited the permeation of air into PCBM:P3HT blend layer, which prevented direct contact between the blend layer and oxygen/moisture. Cell performance decreased to 63.8% of the maximum PCE when the amorphous TiO_x electron collection interlayer was replaced with anatase TiO_2.[146] A similar study demonstrated that electron selective interfacial layers made from crystalline TiO_2 (instead of amorphous) caused PCE to drop in inverted OSCs.[149] Oxygen defects have been observed to increase resistance in amorphous ALD-crafted TiO_2 films, but they can be removed by light soaking.[149] Devices with 15 nm-thick amorphous-TiO_2 layers showed a better performance (PCE=3.31%) than those with polycrystalline TiO_2 of the same thickness (PCE=2.59%). This decrease in performance was attributed to the grain boundaries in crystalline TiO_2 which facilitate easier hole collection by the cathode, leading to a higher carrier recombination.[149] It's worth noting, however, that some report that OSCs using crystalline TiO_2 yield higher mobility.[150] Thus, detailed theoretical and mechanistic studies are needed to fully understand how the electronic interactions between conjugated polymer and amorphous TiO_2 enhance electron collection and charge separation.

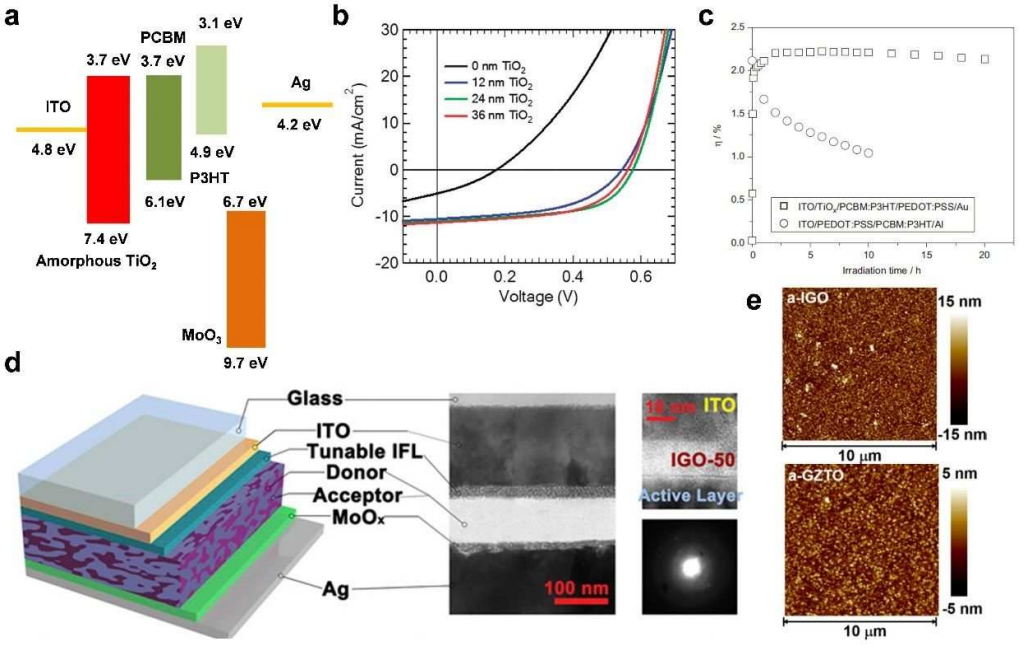

Fig. 7 (a) A proposed energy level diagram of an inverted OSC incorporating CVD-prepared amorphous TiO_2. (b) J-V curves for ITO/CVD-TiO_2/P3HT:$PC_{61}BM$/MoO_3/Ag bulk heterojunction OSCs. Reproduced from ref. 68 with permission from The Royal Society of Chemistry, copyright 2013. (c) Irradiation time-dependent PCE for the ITO/TiO_x/PCBM:P3HT/PEDOT:PSS/Au inverted OSC with an amorphous TiO_x interlayer and for conventional ITO/PEDOT:PSS/P3HT:PCBM/Al OSC. Reproduced from ref. 146 with permission from Elsevier, copyright 2008. (d) A schematic and cross-sectional TEM image of an ITO/amorphous IGO/PTB_7:$PC_{71}BM$/MoO_3/Ag solar cell.[143] Insets show higher-resolution TEM image and nanobeam electron diffraction pattern of amorphous IGO. (e) Representative AFM images of amorphous IGO and GZTO films. Reproduced from ref. 143 with permission from National Academy of Sciences, copyright 2015.

ZnO-SiO_2 (ZSO) is a recently reported amorphous ternary oxide semiconductor with a

work function of ~3.4 eV.[151, 152] It exhibits good electron injection/transport properties, and has been used an alternative to TiO_2 as a cathodic buffer layer in inverted OSC devices. Ar plasma-treated ZSO (Ar-ZSO) and oxygen plasma-treated ZSO (O-ZSO) films have also been investigated.[151] It was found that O-ZSO is more suitable for use in OSCs owing to its higher exciton dissociation efficiency at the polymer (P3HT)/ZSO interface and the smaller work function difference for O-ZSO-based solar cells. OSCs using amorphous O-ZSO as the n-type interlayer showed a better PCE (from 0.03 % to 0.12 % after O_2-plasma treatment).[151] Despite the low PCE, the improved performance signified that amorphous ZSO may function as a viable alternate ETL in OSCs. Recently, Facchettic and Marks et al. reported using other uniform amorphous semiconducting oxide alloys, In-Ga-O (IGO) and Ga-Zn-Sn-O (GZSO) as the ETLs for inverted OSCs (**Fig. 7d** and **7e**, respectively).[143] Amorphous phase IGO and GZSO semiconductor alloys have excellent mechanical flexibility, optical transparency, uniform surface morphology, and good electron mobility.[153, 154] Continuous tunability of conduction band minima over a broad range of 3.5~4.6 eV can be achieved by alloying two or more electronically dissimilar oxides such as IGO and Ga-Zn-Sn-O oxide (GZTO).[143] The low tail and midgap state densities in the amorphous phase were found to suppress charge recombination,[153, 154] and the localized O 2p-based valence bands blocked hole injection from the HOMO of the organic donor.[155] Thus, enhanced PCE, excellent chemical/environmental stability, and good electron mobility of amorphous alloy-based OSCs can be achieved.

3.2.3 Amorphous Hole Collection Interlayer

Metal oxides have been considered to be attractive hole collection interlayers due to their excellent chemical stability. WO_3 has been identified as a promising hole-injection layer due to its good photostability, a long hole-diffusion length (~150 nm).[156-158] As shown in **Fig. 8a**, a thermally-evaporated uniform amorphous WO_3 film was used as a cathode buffer layer in a conventional P3HT:$PC_{60}BM$ OSC.[66] The efficient hole collection of these samples was attributed to the well-matched HOMO levels of WO_3 and P3HT. Notably, the LUMO level of WO_3 also provided a sufficient energy barrier to prevent back-collection of photogenerated electrons. Compared to ITO-based cells, amorphous WO_3-based OSC devices exhibited superior FF, V_{OC}, and PCE, (**Fig. 8b**) possessed significantly better batch-to-batch consistency due to their uniform surface morphology, and displayed improved hole mobility.[66]

Amorphous Cr_2O_3 is another excellent candidate as a cathode buffer layer because of its optimal 3.7 eV band gap.[159] P-type amorphous Cr_2O_3 films were synthesized using the sputtering method and used in FTO/Cr_2O_3/P3HT:PCBM/Al solar cells.[46] PCEs of 3.28% and 2.91% were achieved under AM1.5G 100 mW/cm^2 illumination for devices with and without the Cr_2O_3 layer, respectively. The PCE enhancement for devices with the Cr_2O_3 layer was attributed to the improved of p-type conductivity, enhanced hole collection, and electron blocking from the wide band-gap Cr_2O_3.[46] Notably, the Cr_2O_3 tends to hydroxylated due to water dissociation after its exposure to air. The hydroxyl groups at the surface of amorphous Cr_2O_3 films affected the humidity stability, which can degrade performance of the OSC devices. In this regard, making nitrogen-doped amorphous Cr_2O_3 film may resolve this problem since N in amorphous Cr_2O_3 film could prevent water dissociation and hydroxylation of the Cr_2O_3

film surface. Nitrogen-doped amorphous Cr_2O_3 films were synthesized by radio frequency sputtering.[160] Compared with pure Cr_2O_3, the nitrogen doped amorphous Cr_2O_3 (NACO) had a smoother surface (**Fig. 8d**). The smoother surface resulted in a smaller contact area at the NACO/air interface, which simultaneously prevented water dissociation and hydroxylation. Devices that used NACO as an HTL were observed to possess improved stability, as shown in **Fig. 8e**.[46, 160]

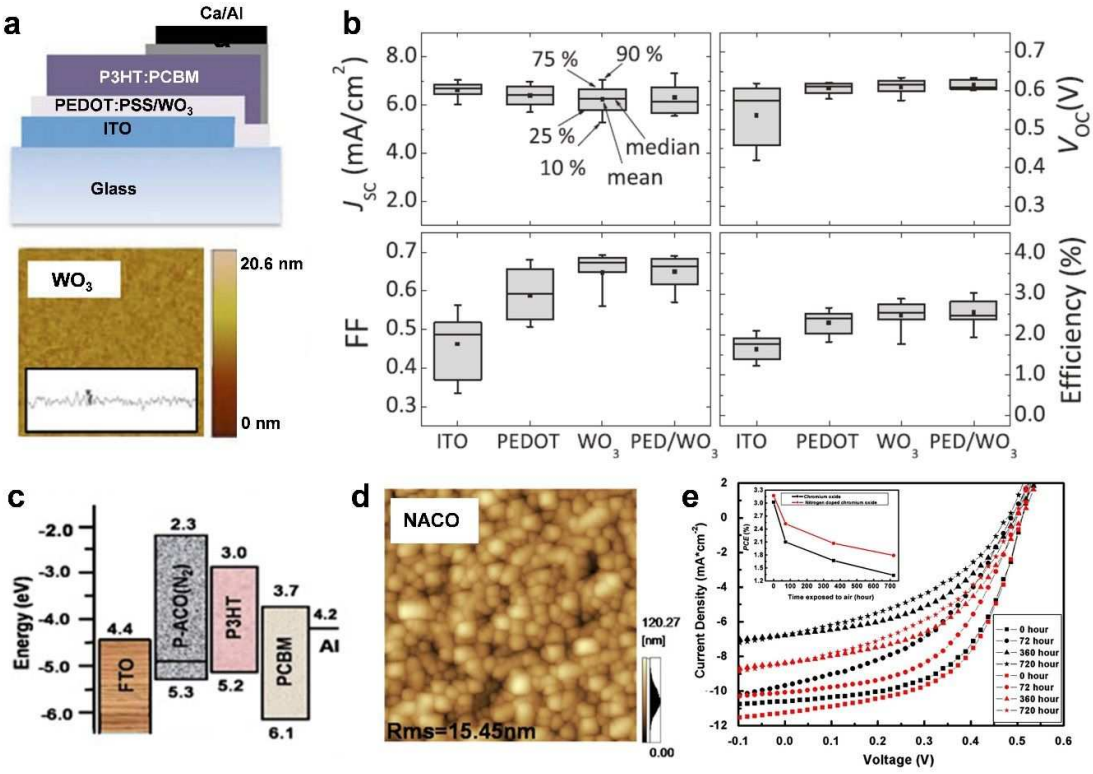

Fig. 8 (a) Schematic device architecture of OSC, and an AFM image of the surface and the cross-sectional profile of WO_3 on ITO. Inset: AFM image of the amorphous WO_3 film. (b) Statistical box graphs for J_{SC}, V_{OC}, FF, and efficiency of devices with various hole collection buffer layers. Reproduced from ref. 66 with permission from Elsevier, copyright 2009. (c) The energy level diagrams of device components referenced to the vacuum level. (d) AFM image

of NACO film on FTO. (e) J-V curves of the OSCs with the ACO or NACO films exposed to air for different hours. Inset: Influence of the air exposure time of the ACO or NACO films. Reproduced from ref. 160 with permission from Elsevier, copyright 2011.

3.3 Dye-Sensitized Solar Cells

Dye-sensitized solar cells (DSSCs) typically consist of a semiconductor photoanode, a counter electrode, a light-sensitizer (a dye molecular), and an electrolyte containing a redox couple such as I_3^-/I^-.[161] Under illumination, the dye molecules are elevated from the ground state to the excited state. The excited-state dye molecules inject electrons into the conduction band of the semiconductor. Then, the electrons are diffused to a conductive substrate and flow into an external circuit. The dye in the oxidation state is reduced and regenerated by the electrolyte, which is subsequently reduced after receiving electrons from the counter electrode, thus completing a cycle. Semiconductor films (e.g., TiO_2, ZnO and WO_3) are the key component of DSSC photoanodes, which are coated onto a conductive substrate.[162] The typical device architecture and working mechanisms of TiO_2-based DSSCs are shown in **Fig. 9**.[163] The TiO_2 photoanode functions as both support for the sensitizers, and a transporter for photo-excited electrons from the dye sensitizer. The absorbed dye molecules generate excited electrons under illumination, which are subsequently injected into the conduction band of the semiconductor photoanodes and travel to the external circuit through the conductive substrate, thus completing a photochemical cycle.[164] Due to the inherent issues of DSSCs, such as low electron mobility, slow transport, and recombination of photo-excited electrons, several studies

have focused on creating more effective nanostructured electrode materials and morphologies.[165-167] A number of these published studies are concerned with the preparation of amorphous semiconducting films to improve DSSC performance. The following sections will examine the recent advances in incorporating amorphous semiconductors into DSSCs.

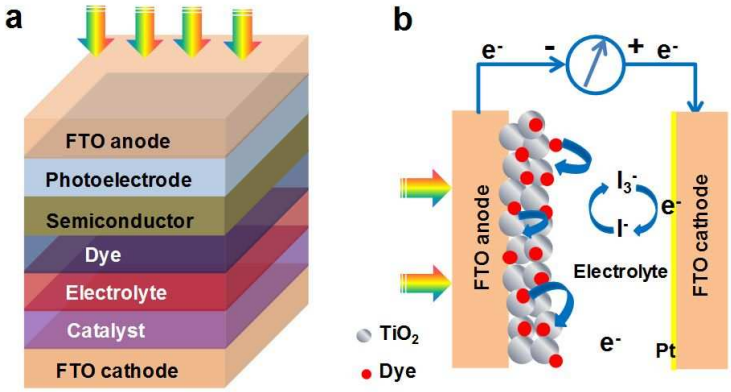

Fig. 9 Schematic representation of a TiO_2-based DSSC: (a) Device architecture and (b) working mechanism.

3.3.1 Amorphous Semiconductor-Based Photoanodes for DSSCs

TiO_2 is the most commonly used photoanode material in DSSCs, but it typically requires a high annealing temperature and can contain a high defect density. Eithiraj and Geethalakshmi[168] compared the electronic structure of an amorphous TiO_2 cluster to that of crystalline anatase TiO_2 by density functional theory and time dependent density functional theory calculations. Both the anatase and amorphous TiO_2 showed similar HOMO-LUMO gaps and singlet-singlet lowest excited state energies (**Fig. 10a** and **10b**). There was also a similar energy-level alignment between the dye molecules and both the amorphous and anatase TiO_2, with the energy difference being less than 0.1 eV.[168] This suggested that amorphous TiO_2 may

be a good alternative for use as a photoelectrode in DSSCs. However, some experimental data has indicated that the use of amorphous TiO_2 can lead to a relatively lower dye packing density (compared to crystalline phases) because the adsorption of dye molecules is strongly correlated to surface facets of semiconductor photoanodes.[169-171] Thus, the incorporation of both amorphous and crystalline TiO_2 into DSSCs was studied. Mixed phases of crystalline and amorphous TiO_2 were found to improve the conversion efficiency of DSSCs.[172] Zhang et al. synthesized a nanocrystalline/amorphous, core/shell nanostructured TiO_2 electrode at low temperature, and, due to large surface area of the nanostructured film, it showed improved adsorption of N3 dye (i.e. cis-bis(isothiocyanato)bis(2,2′-bipyridyl-4,4′-dicarboxylato)ruthenium(II)) compared to pure amorphous TiO_2.[173] Notably, the electron collection of amorphous TiO_2-based photoanode was still unsatisfactory. Kang and Jeon et al. fabricated a shell of amorphous ALD-TiO_2 layer on the inner walls of antase TiO_2 nanotube (NT) electrodes.[174] The thin amorphous TiO_2 layer was dissolved after soaking in water for 48 h and converted into nanoparticles by a classic dissolution-precipitation path. The amorphous TiO_2 layer dissolves to form hydroxytitanium complexes ($Ti(OH)_n^-$) and then precipitates on the TiO_2 layer to form TiO_2 nanoparticles.[175, 176]. These amorphous TiO_2 nanoparticles offer more charge injection sites at the interfaces, and thereby enhance the charge injection efficiency. The nanostructured TiO_2 electrode with a nanocrystalline core/amorphous shell exhibited less transport resistance (~0.5 Ω), which implied that the electrode was capable of conducting electrons from the injection site to the substrate. In addition, this core-shell architecture facilitated dye adsorption on the surface, ensuring adequate carrier generation.

Interestingly, debate exists over whether or not the use of the amorphous TiO_2-based photoanodes in DSSCs improves device performance. P25, a commercially available TiO_2 consisting of mixed anatase and rutile phases with average particle sizes of 25 nm, is a cheap source of TiO_2 nanoparticles that has been widely used in DSSC applications and has a substantial amount of amorphous content.[177] Kim et al. investigated the effect of removing the amorphous phase in P25 on DSSC performance[171] and found that the efficiency of devices based on samples without amorphous particles was enhanced by 44% (compared to those based on untreated P25). The increased efficiency was attributed to enhanced light harvesting because higher dye loading is achieved on crystalline phase than amorphous phase. This result shows that more studies are needed to understand amorphous phase TiO_2 and the mechanisms behind how the amorphous structure impact DSSC performance.

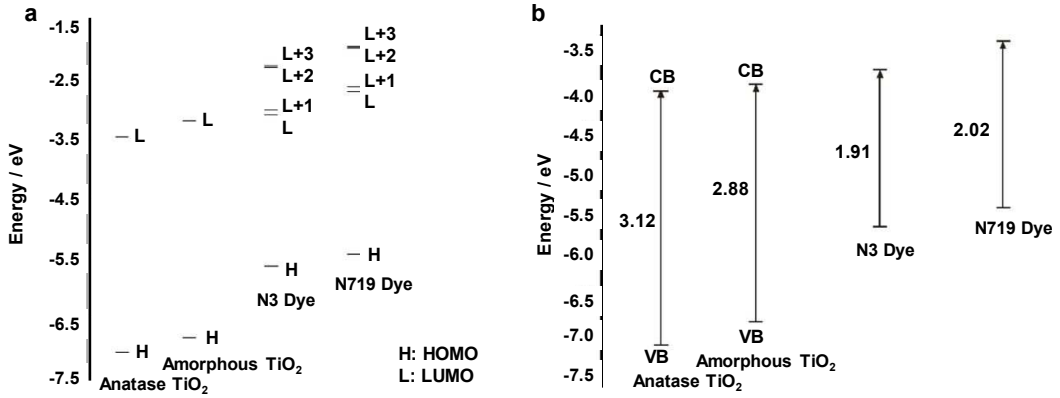

Fig. 10 (a) The HOMO and LUMOs energy level alignment of the anatase and amorphous TiO_2 clusters and dyes (N3 and N719). (b) Schematic representation of the ground and excited sate energy levels for the anatase and amorphous TiO_2 clusters as well as dye (N3 and N719). Reproduced from ref. 168 with permission from Elsevier, copyright 2013.

Doping metals into semiconductors has been proven to be an effective approach to optimize their electronic structure for efficient devices, and several studies have looked at the influence of the metallic dopants on the photovoltaic behavior of TiO_2 photoanodes in DSSCs.[178-180] TiO_2 electrodes fabricated with a bilayer of nano-crystalline TiO_2 and a Er^{3+} and Yb^{3+} -doped amorphous TiO_2 showed an increased DSSC efficiency of 15.6%. This improvement in power conversion efficiency was ascribed to the absence of grain boundaries, better light scattering, and higher dye packing density of the bilayer electrode.[181] Amorphous Ti^{3+}-TiO_2 nanoparticles grafted on anatase TiO_2 nanotube arrays were also investigated for use as photoanodes in DSSCs.[70] The TiO_2 nanotube arrays were immersed in TiO_2 nanoparticles-contained water. The amorphous TiO_2:Ti^{3+} nanoparticles were synthesized by ultraviolet pulsed laser ablation of the water. The amorphous Ti^{3+}-TiO_2 photoanodes facilitated better light absorption in the visible region, and its higher quasi-Fermi level (as compared with anatase TiO_2 nanotubes) resulted in increased V_{oc}.[70]

Though rarely reported, some multi-cation oxides have been investigated for application in DSSCs. The electric resistivity of these materials may be easily tuned via altering their composition, which makes them a favorable candidate for photoanodes in DSSCs. For example, zinc stannate (Zn_2SnO_4 or $ZnSnO_3$) is a promising transparent oxide semiconductor because of its suitable band gap and high electron mobility.[182] Amorphous porous sub-micrometer Zn_2SnO_4 fiber photoanodes were constructed between the mixed inorganic precursors of $Zn(OAc)_2$-$Sn(OAc)_4$ and a polymer matrix.[183] The resulting DSSCs with a 3 μm-thick Zn_2SnO_4 photoanode showed a promising photovoltaic conversion up to 3.7% under standard AM 1.5G

sunlight (100 $mW \cdot cm^{-2}$).[183] When employing amorphous $ZnSnO_3$ (another known zinc stannate) as a photoanode, inferior electron transport properties were observed to that of crystalline $ZnSnO_3$ samples.[184] Nevertheless, amorphous $ZnSnO_3$ is still worth scrutinizing as a potential photoanode because of its good transparency, conduction, stability against acidic dye molecules, and identical constituent elements to Zn_2SnO_4. In particular, understanding the differences in the optical and electronic properties of the amorphous and crystalline phases of this material is critical for future applications in DSSCs.

SEM image of Zn
2
SnO
4
fi bers calcined at 450 ° C

3.3.2 Amorphous Counter Electrodes

The counter electrode is also an important component and plays a vital role in the performance of DSSCs. Platinum is one of the traditional counter electrodes that serves as both an electron collector and an electrocatalyst for the regeneration of triiodide (I_3^-) in the electrolyte.[176] However, because platinum is expensive and easily corroded by the I-based electrolyte in liquid-state DSSCs,[185] development of low cost alternative counter electrodes is of great interest. CoS has been proposed as a promising substitute due to its superior electrocatalytic activity, low cost, and abundant feedstock.[186, 187] Amorphous CoS fabricated *via* an electrochemical milling process was used as the counter electrode in DSSCs, and the resulting cells possessed higher electrocatalytic performance than platinized electrode towards the reduction of I_3^-.[188] High exchange current densities were achieved for the counter electrode

of CoS with crude morphology. This morphology opened the surface of CoS to the surroundings, increasing the contact between the CoS and I_3^-, and thus enhancing the properties in DSSCs. By preparing the CoS using porous CoO as the precursor, much higher conversion efficiency was achieved due to higher active surface area as well as the lower charge transfer resistance of CoS than Pt electrode, as shown in **Fig. 11a** and **11b**.[188] Amorphous indium zinc oxide (IZO) was found to be a relatively conductive film because it lacks grains or grain boundaries that can result in stress and film cracking.[189] Despite these advantages, its intrinsically low electronic conductivity remains an issue, but the incorporation of noble metals into IZO can address this problem. Sun et al. prepared an Au/amorphous IZO bilayer at room temperature and used it as the counter electrode in DSSCs.[161] High conductivity of 1.2×10^5 $S\cdot cm^{-1}$ (**Fig. 11c**) and mobility of 65.6 $cm^2\cdot V^{-1}\cdot s^{-1}$ (**Fig. 11d**) were achieved due to the formation of Au transport paths.[161] The figure of merit (FOM, $\Phi_{TC}= T^{10}$/sheet resistance) for Au-IZO ($\Phi_{TC}= 4.0\times10^{-2}$) is 57 times higher than that of the IZO sample and 3 times higher than that of ITO ($\Phi_{TC}=1.5\times10^{-2}$). The Au-IZO-based DSSC showed a photovoltaic efficiency of 3.73% under AM1.5 illumination (100 $mW\cdot cm^{-2}$).[161] Similarly, a Pt/amorphous porous NiO bilayer was fabricated and used as the counter electrode of a DSSC, and the resulting cell showed enhanced short-circuit current density and efficiency, both of which were ascribed to the increased active surface area.[190]

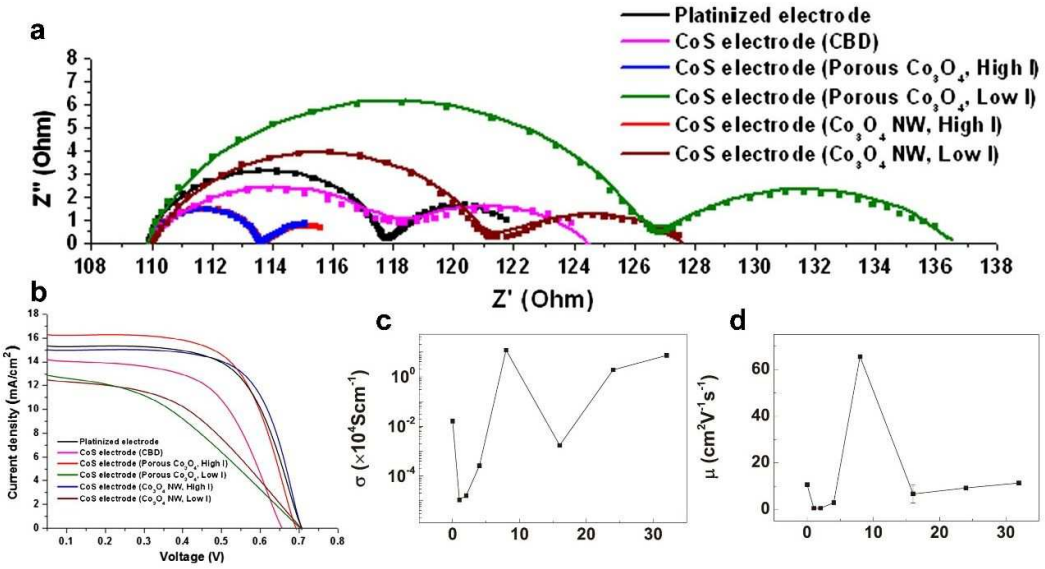

Fig. 11 (a) Nyquist plots of Pt & CoS electrodes. CoS counter electrodes were prepared by chemical bath deposition method (CBD), and electrochemical method with porous Co_3O_4 or Co_3O_4 nanowire (NW) precursors, respectively. (b) J-V curves of the DSSCs with various electrodes. Reproduced from ref. 188 with permission from Elsevier, copyright 2016. Variation of (c) conductivity, σ and (d) mobility, μ for the Au-IZO samples as a function of Au nominal thickness. Reproduced from ref. 161 with permission from Elsevier, copyright 2015.

3.4 Quantum Dot-Sensitized Solar Cells (QDSCs)

Semiconductor quantum dots (QDs) have drawn considerable interest because of the ability to easily tune their bandgap by varying both size and composition, as well as the ability to form intermediate bands.[191-193] As the size of a QD approaches the exciton Bohr radius, quantum confinement effects dominate and electron energy levels are treated as discrete instead of a continuous band. This ability to tune energy levels has led to the incorporation of self-assembled QDs or colloidal QDs as sensitizers in solar cells to boost performance.

Unfortunately, charge recombination at the semiconductor/sensitizer/electrolyte interfaces in QDSCs has been found to be more prevalent as compared to conventional DSSCs due to the existence of the surface trap states in the QDs which act as recombination centers.[194, 195] Electrons transported in the semiconductor layer injected from the excited QDs may recombine with either the holes at the valence band of QDs or with the oxidized species in the redox electrolyte through direct contact.[194, 196] Interfacial engineering of the QDs by coating them with a buffer layer is a widely accepted method to inhibit such recombination in QDSCs.[197-199] Furthermore, the introduction of a buffer layer facilitates the utilization of the I^-/I^{3-} redox couple for a higher open circuit voltage and fill factor compared to cells with the commonly used polysulfide electrolyte.[200, 201] Some of the works selected for this review focused on employing amorphous semiconductor phase such as TiO_2, ZnS as the buffer layers in QDSCs.[198, 202] We will introduce these buffer layers below individually.

3.4.1 Amorphous TiO_2 as Buffer Layer

An amorphous TiO_2 layer was inserted in QDSCs to suppress interfacial charge recombination and decreasing trap state defects induced by the large lattice mismatch between interfaces.[21] Schematic architectures of the different QDSCs are shown in **Fig. 12a**. The position of the amorphous TiO_2 buffer layer (i.e. between crystalline TiO_2 and ZnS/SiO_2 coating layer, or outside the crystalline TiO_2 layer) was found to have a great impact on QDSC performance, particularly their photovoltage (**Fig. 12b**).[203] The amorphous TiO_2 layer located at the interface between the QD-sensitized photoanode and ZnS/SiO_2 layer was found to inhibit

charge recombination at the interface[203] and passivate QD surface states that act as charge traps.[198] The density of trap states induced by the lattice mismatch at the device interfaces also decreased after incorporation of an amorphous TiO_2. The QDSCs with an amorphous TiO_2 buffer layer displayed were found to show superior photovoltaic performance to that of cells made with a crystalline buffer layer.[203] For example, an amorphous TiO_x buffer layer was made via dip-coating and used between a graphene photoanode and QD sensitizers.[204] **Fig. 12c** demonstrates the photogenerated electron transfer processes in this QDSC architecture. The amorphous TiO_2 buffer layer inhibited recombination of the electrons and holes at the graphene-QD and oxidized species-electrolyte interfaces.[204] The transport of electrons from TiO_2 to graphene via a rapid transfer process. Due to the high conductivity of graphene and the energy difference from TiO_2, electrons injected from QD sensitizer transferred directly to graphene through TiO_2 conducting band, rather than trapped by the trap states in the amorphous TiO_2 layer.[204] The addition of the TiO_x interlayer was observed to both eliminated the decay of photocurrent and lead to a longer electron lifetime (**Fig. 12d**). It was found to provide a barrier that suppressed charge recombination by separating graphene from the oxidized QDs and redox couples in the electrolyte. As a result, the photocurrent and photovoltage of the QDSCs were both greatly enhanced with the use of an amorphous TiO_x buffer layer.[204] In addition, an amorphous TiO_2 coating can protect the QDs from the very corrosive redox couple.[198] By blocking trap states where holes can accumulate with an amorphous TiO_2 coating, degradation of QDs can be avoided, thus further enhancing the photo-stability of QDSCs.[198]

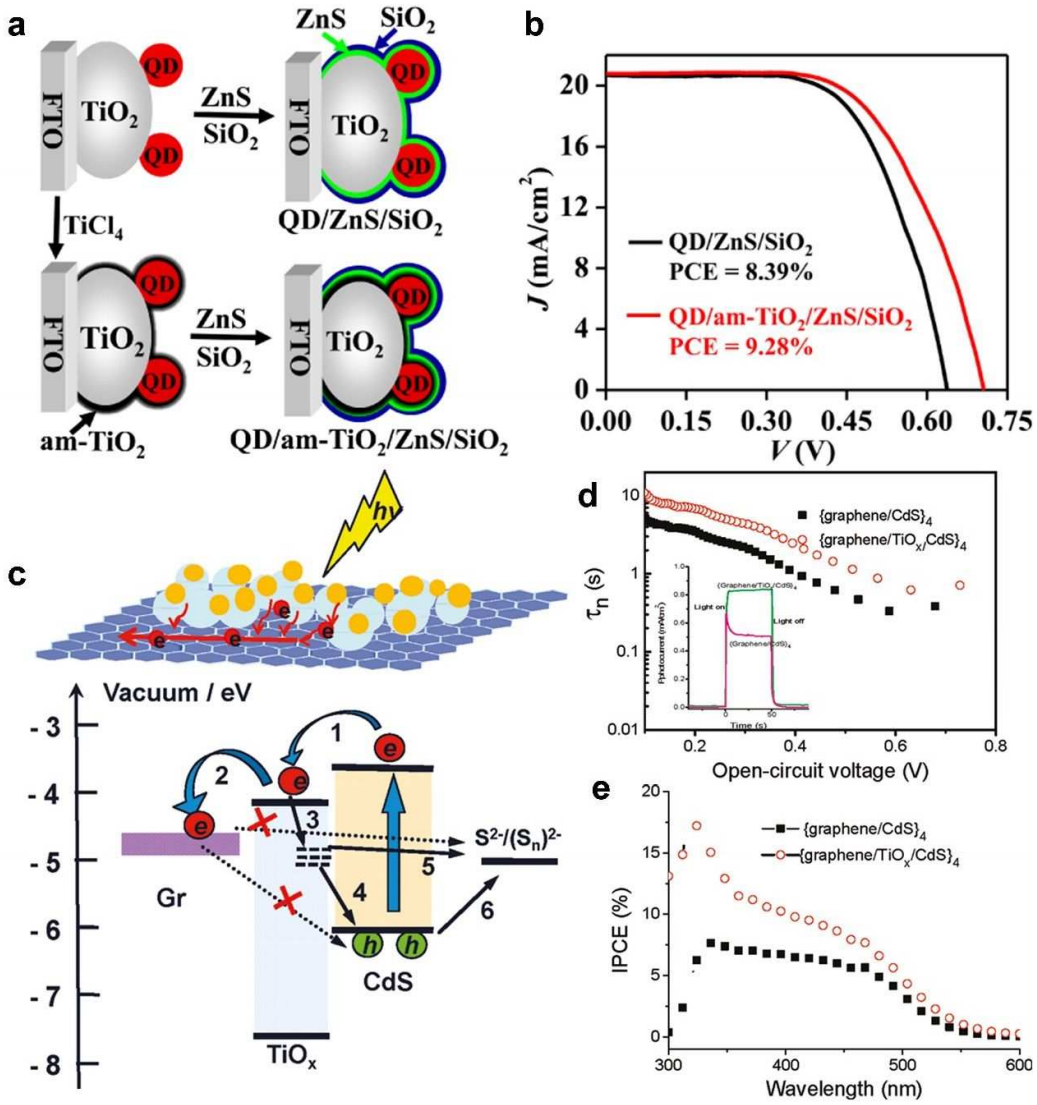

Fig. 12 (a) The schematic architectures and (b) performance of the amorphous TiO_2-based QDSC devices. Reproduced from ref. 203 with permission from American Chemical Society, copyright 2015. (c) Schematic structure of photogenerated electron transfer processes in a layered graphene (Gr)/QDs and the energy band diagram. (d) Electron lifetime as a function of V_{oc} and (e) IPCE (incident photon to current efficiency) of the photochemical cell with and without an amorphous TiO_x layer. Reproduced from ref. 204 with permission from American Chemical Society, copyright 2011.

3.4.2 Other Amorphous Inorganic Semiconductors Used in QDSCs

Various other inorganic amorphous semiconductors have been incorporated into QDSCs. For example, inorganic amorphous ZnS was used to confine PbS QDs in QDSCs.[205] It was determined that a type I heterojunction was formed at the PbS/ZnS interface, which facilitated photogenerated carrier separation and transfer. Carriers in the PbS QDs accumulated due to the potential barrier from the ZnS shell, which reduced the cooling rate of hot carriers. Typically, conventional colloidal QDs (like PbS) have a high density of states because they use organic molecules as capping agents.[206] Using amorphous ZnS instead of organic molecules as the capping ligand can effectively reduce the states of PbS QDs by creating a bridging sulfur layer at the interface of PbS and ZnS.[207, 208] Two distinct configurations including embedding and blending structures were studied, as shown in **Fig. 13**. In embedded configuration, larger PbS QDs were isolated and dispersed in a ZnS matrix, which provided for substantial distance between the QDs. In blended configuration, smaller size PbS QDs were mixed with a ZnS matrix so that there was indiscernible distance between particles. The smaller QD size and closer distance between QDs in the second configuration displayed more efficient charge injection and transport, and thus resulted in QDSCs with superior photovoltaic performance.[205] In another study, the insertion of an amorphous ZnO interlayer between the cathode and active layer was demonstrated to improve the efficiency of QDSCs.[209] The ZnO buffer layer was found to both reduce recombination by preventing direct contact of the active layer and metal electrode and facilitate electron extraction toward the cathode because of more suitable energy

alignment.[209] Compared to crystalline ZnO, amorphous ZnO is superior in acting as a cathode interfacial layer and moisture scavenger because of its tight coverage and high surface area.[209]

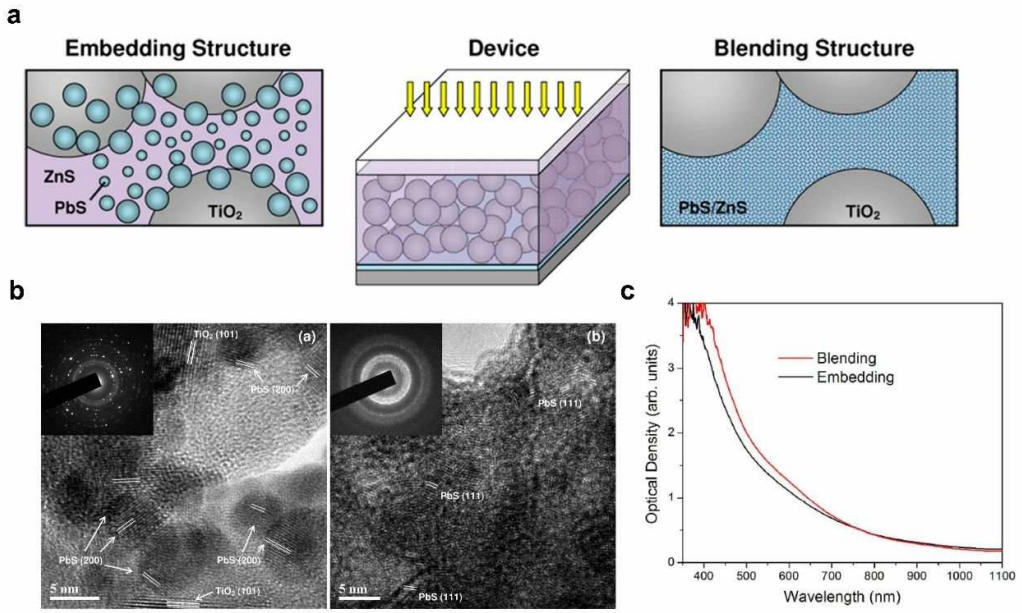

Fig. 13 (a) Illustration of device structure with PbS quantum dots embedded in and blending with amorphous ZnS. (b) TEM images of PbS quantum dots embedded in and blending with ZnS dielectric matrix prepared in methanol and aqueous solution, respectively. Insets are the corresponding selected area electron diffraction patterns. (c) Absorbance spectra of completely filled bulk heterojunctions with embedding and blending structures. Reproduced from ref. 205 with permission from American Chemical Society, copyright 2014.

4. Amorphous Inorganic Semiconductors for Photoelectrocatalytic Water Splitting

4.1 Amorphous Semiconductor-Based Photoanodes

Photoelectrocatalytic (PEC) splitting of water to O_2 and H_2 is an attractive approach for

capturing and storing solar energy for fuel production.[3, 210] High-efficiency PEC solar-driven water splitting requires semiconductor materials with a suitable bandgap to absorb a large portion of the solar spectrum. These materials must also have the capacity to deliver a substantial amount of current, good stability in an aqueous environment, and photovoltage required to drive the fuel-forming anodic and cathodic half reactions. Among the state-of-the-art PEC systems, the most prevalent shortcoming is the stability of the electrodes.[211] Many II-VI semiconductors, such as CdS, ZnSe, GaAs, and GaP, have been employed as photoanodes for efficient photocatalytic water splitting because of their negative potentials of valence-band edges.[212] Notably, the electrolysis of water is generally performed in strongly alkaline or strongly acidic media due to their high conductivity, minimal pH gradients during operation, and rapid water oxidation ability. II-VI semiconductor materials are often unstable in aqueous electrolytes in these pH ranges, which can cause either anodic photocorrosion or photo-passivation of the materials.[3, 34, 35, 213, 214] Various coating strategies have been explored to improve the stability of the semiconductors for applications in photocatalytic water splitting, including deposition of metal (Pd, Pt, Ni, Ir etc.) or metal oxide (NiO_x, MnO_x, RuO_x, IrO_x, etc.) thin films onto the semiconductor photoanodes.[19, 210, 215, 216] Despite these advancements, imperfections in the protective coatings of materials can lead to the sudden system failure. Unfortunately, the improved stability of semiconductor photoanodes generally comes at the price of decreased efficiency of water oxidation. To this end, amorphous semiconductors have been explored as a component in PEC to improve the stability of photoanodes against both photocorrosion and photopassivation.[3]

4.1.1 Amorphous TiO_2 Photoanodes

Recently, amorphous TiO_2 films have been used as coatings to protect a variety of photoanode materials under oxygen evolution reaction (OER) conditions in alkaline electrolytes.[3, 18, 23, 34, 35] Amorphous TiO_2 is more widely available in nature and can be prepared into different forms at room temperature, which make it a good alternative to its crystalline counterpart. Notably, carrier conduction in the amorphous TiO_2 has been attributed to hopping channels provided by impurities such as oxygen vacancies and their defect states.[3, 8, 217-220]

Both the preparation technique and thickness of the TiO_2 protection layers greatly impact water oxidation. Si photoanodes were protected by coating them with CVD- crystalline TiO_2.[221] The cracks and pinhole-free TiO_2 coating was found to prevent dissolution of the substrates, but the thick protection layer inhibited electron transfer from the electrolyte to the Si substrate, resulting in poor device performance.[221] An ALD-crafted conformal pinhole-free layer of 2-nm thin crystalline TiO_2 was also used to stabilize Si photoanodes for water oxidation.[19] Deposition of this electrically insulating film was found to both prevent oxidation of the Si photoanode and accelerating tunneling of photogenerated holes between the catalyst layers and the underlying substrate (**Fig. 14a-14c**).[19] However, as this barrier became thicker, the hole conduction via a tunneling mechanism was suppressed, which induced a large series resistance to the PEC device and increased OER and additional voltage losses.[222] To mitigate the negative effects of the crystalline TiO_2 layer thickness on water oxidation performance, an intentionally electronic-defect rich unannealed amorphous TiO_2 film was used as a protective layer that

allowed for the passage of current as a "leaky" dielectric.[3, 223] While charge transport in crystalline TiO_2 is dominated by barrier tunneling that necessitates thin films,[19, 222, 224, 225] transport in amorphous TiO_2 protection layers are dominated by other mechanisms and thus (**Fig. 14d**) can maintain good performance in hundred-nanometer-thick films,[3, 18, 34, 35, 226] as shown in **Fig. 14e-14h**. Amorphous ALD-TiO_2 protection layers in PECs with thicknesses ranging from 4 to 143 nanometers were shown to provide electronic defects to promote hole conduction and were sufficiently transparent to allow light penetration to the protected semiconductors. Dual-protected Si photoanodes were created by sputtering 100 nm Ni films onto the TiO_2, and these Si photoanodes yielded continuously O_2 production for more than 100 hours, and the photocurrent only decreased by ~10% while the fill factor decreased less than 5%. Improved stability was also observed in analogous n-p^+-GaAs/amorphous TiO_2/Ni-film and n-GaP/TiO_2/Ni-film photoanodes.[3, 34] An *ab initio* molecular dynamics model was built for amorphous TiO_2, and it was used to study the mechanism of hole diffusion across amorphous TiO_2 layers.[227] It was found that in amorphous TiO_2, O-O peroxy linkages facilitate hole diffusion. The hole diffusion was triggered through an exchange mechanism involving O-O pairs with energy barriers lower than 0.5 eV.[227]

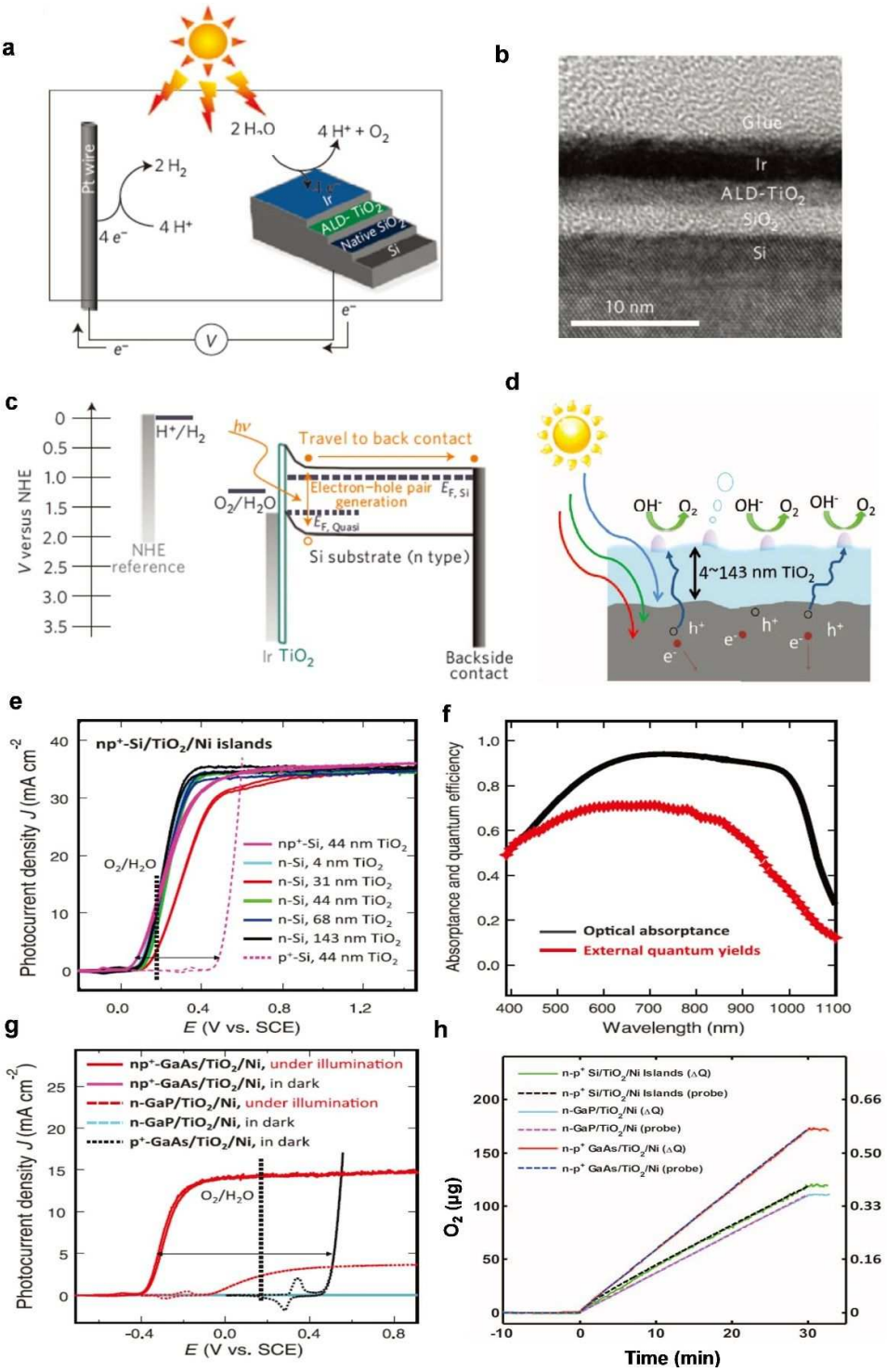

Fig. 14 (a) Schematic and (b) TEM of the Si photoanode coated with ALD-crystalline TiO_2. (c) Energy band diagram of the anode at 1V versus NHE in pH 0 solution. Reproduced from ref. 19 with permission from American Chemical Society, copyright 2011. (d) Cross-sectional

schematic of a photoanode stabilized with amorphous ALD-TiO_2. Photoelectrocatalytic behavior of amorphous TiO_2-coated (e) Si, (g) GaP and GaAs photoanodes in 1.0 M KOH. (f) Normal-incidence optical absorptance and external quantum yields for n-Si photoelectrodes. (h) O_2 detected for different photoanodes. Reproduced from ref. 3 with permission from American Association for the Advancement of Science, copyright 2014.

In addition to ALD- amorphous TiO_2 films, electrochemical deposited (ECD) amorphous TiO_2 has also been utilized as a protective layer to improve the stability of photoanodes in PEC devices. Amorphous TiO_2 layers with thicknesses ranging from 80-120 nm were coated via electrodeposition on the photoanode of W-doped $BiVO_4$/FTO, and they improved photoelectrocatalytic performance and enhanced stability.[52] The beneficial effect from the ECD-amorphous TiO_2 protection overlayer was attributed to its reaction with surface defects and their deactivation with regards to surface recombination.[228] An electrodeposited amorphous TiO_2 layer was found to passivate the surface of gold electrode, and minimize background current.[53] A Pt/amorphous TiO_2/n-Si photoanode was tested for photoelectrocatalytic OER, and no current decay was observed for more than 12 h and it produced 19 $mA \cdot cm^{-2}$ of photocurrent density under 100 $mW \cdot cm^{-2}$ xenon lamp irradiation.[229] A $SrTaO_2N$/TiOx/Ni(OH)x/CoPi photoanode is fabricated with an amorphous ECD-TiOx blocking layer. Such an amorphous layer between $SrTaO_2N$ and Ni(OH)x can not only suppress the recombination of photogenerated electron-hole pairs, but protect the oxynitride from corrosion in the PEC application.[220]

4.1.2 Black TiO_2 Photoanodes

As mentioned above, amorphous phase semiconductors have been employed in many fields because they possess unique electronic structures which, in some cases, can create effective catalytic centers.[7, 230, 231] Recently, combining crystalline and amorphous materials has been shown to improve catalytic performance due to a synergistic effect between the two phases. Crystalline TiO_2 quantum dots (nanocrystals) coated with an amorphous black hydrogenated TiO_2:H surface layer were fabricated by hydrogenating crystalline TiO_2 at 20 bar and 200°C for 5 days.[75, 232, 233] These samples were then used as electrodes, and enhanced PEC performance was achieved. Photos of the samples and their properties are shown in **Fig. 15a** and **15b**.[75] The inherent disorder in the amorphous phase was found to broaden the tails of states, extending into the otherwise forbidden band gap.[75] The hydrogen concentration was found to be the highest in the disordered layer, which also had more dangling bonds than the crystalline core. Dangling bonds and defects in amorphous nanoparticles have been reported to serve as effective electron traps, preventing recombination of electrons and holes.[234] Defect-rich black TiO_2:H nanoparticles are known to shift optical absorption from ultraviolet to near infrared and display both excellent photoactivity and stability in photocatalytic hydrogen generation .[75, 235] The enhanced light absorption of hydrogenated black TiO_2:H can be attributed to its surface disorder and the formation of oxygen vacancies.[75, 235, 236] Due to lattice disorder, the Ti 3d orbitals and hybridized O 2p orbitals and Ti 3d orbitals up-shift the valance band edge of TiO_2, deriving the mid-gap states (**Fig. 15c**).[75] The visible and near infrared-light absorption of black TiO_2:H has been observed to result from the transitions from the TiO_2

valence band to the oxygen vacancy levels or from the oxygen vacancies to the TiO_2 conduction band.[77, 237, 238] The doped H, as a shallow donor, has been found to accelerate charge transport at the semiconductor and electrolyte interface.[45] Amorphous black TiO_2:H displayed a comparable photocurrent density to that of crystalline TiO_2 materials (674 $\mu A/cm^2$) at an applied voltage of 1.23 V vs. RHE.[45]

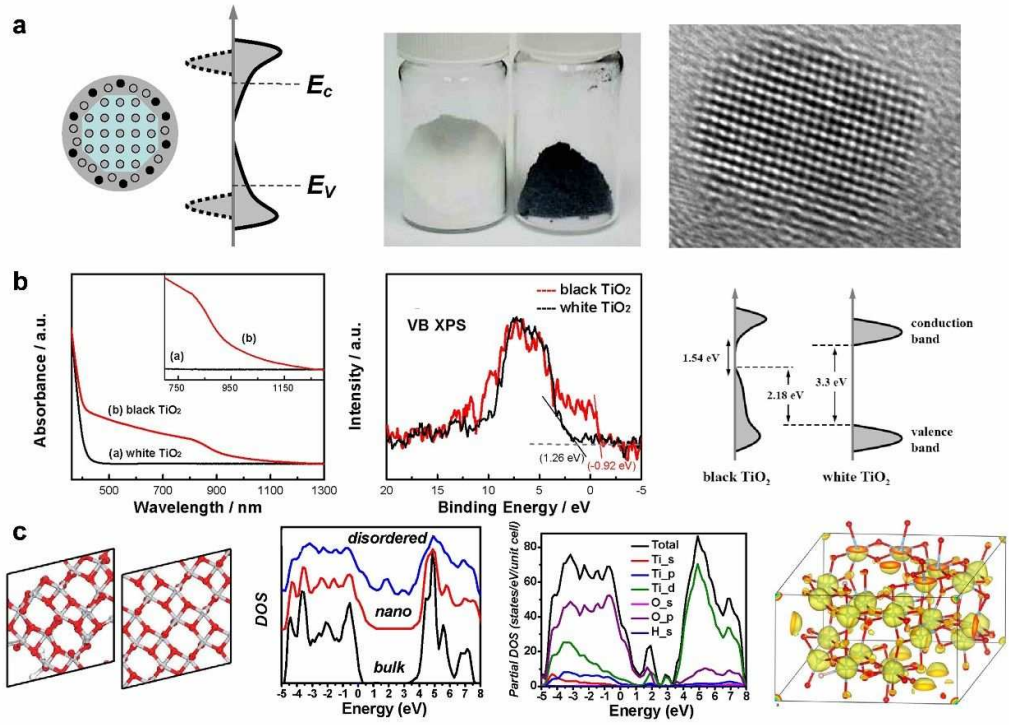

Fig. 15 (a) Schematic illustration of the structure and electronic density of states of a disorder-engineered semiconductor nanocrystal with dopant incorporation (left), a photo comparing un-modified white and disorder-engineered black TiO_2:H nanocrystals (center), and HRTEM images of TiO_2:H with the crystalline core and the disordered outer layer (right). (b) Spectral absorbance and valence band XPS spectra of the white TiO_2 and black TiO_2:H (left and center,

respectively); Schematic illustration of the density of states of TiO_2:H and white TiO_2 nanocrystals (right). (c) Schematic illustration of a supercell for TiO_2:H and anatase TiO_2; calculated DOS of TiO_2:H (left panel), TiO_2 nanocrystal, and a bulk crystal (second panel); Decomposition of the total DOS of TiO_2:H into partial DOS of the Ti, O, and H orbitals (third panel); Three-dimensional plot of calculated charge density distribution of a mid-gap electronic state of disorder-engineered (at about 1.8 eV) TiO_2 nanocrystals (right panel). Reproduced from ref. 75 with permission from American Association for the Advancement of Science, copyright 2011.

To improve the stability of photoelectrocatalytic electrodes, hydrogen treated amorphous TiO_2:H was studied in comparison with thermally treated amorphous TiO_2 under vacuum. In both treatments, 28.7 nm thick amorphous TiO_2 films were formed on a single crystal Si substrate.[239] The vacuum thermally-treated TiO_2 possessed localized Ti^{3+}, Ti^{2+}, and O^- species due to electrons being transferred from an anionic to cationic network with a constant atom ratio of O to Ti. In contrast, the atomic hydrogen treatment removed O atoms and decreased the atom ratio of O to Ti in amorphous TiO_2 and created O vacancies surrounded by Ti cations with either a Ti^{3+} or Ti^{2+} valence. As a result, the vacuum heat treated amorphous TiO_2 was found to significantly prevent the electrode from photocorrosion and improve the stability of devices. The hydrogen treatment was not found to increase the stability of TiO_2. [239] These results indicate that different synthesis strategies generate different defects which may play

distinct role on the device performance. Thus, it is important to design and control the defect types during the preparation of the amorphous semiconductors.

4.1.3 Other Amorphous Semiconductor Photoanodes

For photoanodes in state-of-the art PEC systems, most decreases in water splitting efficiency can be traced to carrier recombination, charge transport losses, and chemical/photo-corrosion. Currently, few photoanode materials can simultaneously alleviate or diminish all the loss processes, so new semiconductor materials-based photoanodes need to be developed.[240] The combination of different phases and/or semiconductors opens up new avenues to overcome these losses.[241, 242] High-performance photoanodes with a maximum photocurrent of 2.52 mA/cm^2 at 1.23 V_{RHE} under AM1.5G illumination were achieved by combining nanometer-thick amorphous layers with small crystalline nanoparticles (similar to the structure of TiO_2:H mentioned above).[243] Amorphous layers of NiO_x and $Co(OH)_2$ were shown to reduce photocorrosion and increase the water oxidation kinetics.[243] A photoanode made of an amorphous NiO/single crystalline ZnO core-shell nanorod array exhibited a remarkable cathodic shift in the onset potential for water oxidation compared to that of a bare ZnO photoanode.[244] The crystalline ZnO nanorod core acted as a photon absorber and charge transporter, while the amorphous NiO shell served as an electrocatalyst that promoted surface oxygen evolution reaction.[244] Similarly, when an amorphous $CuSnO_3$ film with an n-type band gap of 2.3 eV was utilized as a top layer on a WO_3-based heterojunction photoanode, the onset potential and photocurrent density of the PEC device was improved due to the formation of a

type II heterojunction between of the $CuSnO_3$ and WO_3.[245] Hematite (α-Fe_2O_3) is an attractive semiconductor for water oxidation due to its high absorption of visible light and chemical stability in alkaline media. Photoanodes made from α-Fe_2O_3 combined with a thin amorphous nickel hydroxide layer (such as NiOOH [246] or $Ni(OH)_2$ [247]) displayed enhanced photocurrent and a cathodic shift of onset potential. Such enhanced performance can be attributed to the high specific surface area of amorphous nickel hydroxides, the reduced resistance and its ion-permeability which stores holes produced in α-Fe_2O_3.[246] The resistance reduction was assigned to a higher superficial contact area at the electrode/electrolyte interface as well as passivation of the superficial trap sites.[247]

Elemental combination at the atomic level may also be a valid method to address water splitting efficiency losses by modifying the intrinsic bonding structure and imparting novel physical and chemical properties.[248, 249] Partial substitution of Si atoms for the Zn or Ge atoms in Zn_2GeO_4 has been shown to distort bonding structure and form amorphous $Zn_{1.7}Si_{0.3}GeO_4$ (ZSGO) or crystalline $Zn_2(GeO_4)_{0.88}(SiO_4)_{0.12}$ (ZGSO) nanowires with tunable band structures, respectively.[234] Photoanodes made from amorphous ZSGO nanowire arrays exhibited a better efficiency and stability in photoelectrocatalytic water splitting than crystalline ZGSO nanowires because of its higher light-harvesting capability, lower charge recombination, faster charge separation, and higher specific catalytic activity.[250]

4.2 Amorphous Semiconductor-Based Photocathodes

Like photoanodes, preventing photocathodes from photocorrosion in aqueous

electrolytes is also a critical issue that needs to be addressed for PEC water splitting applications. Incorporation of wide-band gap semiconductor coatings and proper electrocatalysts onto the solar energy absorbing material is an innovative approach to stabilize the photoelectrode and reduce the interfacial kinetic barrier. Recently, passivation of the photocathode was attempted by introducing an amorphous semiconductor overlayer on top of the absorber semiconductor (for example, Cu_2O).[211, 251, 252] The protective amorphous overlayer must have chemical stability and favorable band alignment to create a p-n junction, which facilitates charge extraction and protects the absorber material from the aqueous electrolyte.

4.2.1 Amorphous TiO_2 and Black TiO_2 Photocathodes

ALD amorphous TiO_2 is a promising candidate to protect photocathodes in PEC devices because it is chemically stable under basic conditions, creates a conformal layer, with controllable thickness, and can modify the electrode surface.[3, 19, 253, 254] Turner et al. used a 35 nm ALD-TiO_2 layer to protect a p-$GaInP_2$ photocathode functionalized by a cobaloxime molecular catalyst ($GaInP_2$-TiO_2-cobaloxime).[12] The surface modification strategy for the p-$GaInP_2$ photoelectrodes is shown in **Fig. 16**. The amorphous TiO_2 layer, which is inactive towards HER, was demonstrated to act as an antireflective coating[255] and allow transport of photoexcited electrons.[256] The inactive amorphous TiO_2 can facilitate the cobaloxime catalyst, which can lower the kinetic barrier and provide high activity for water reduction.[12] The modified $GaInP_2$-TiO_2-cobaloxime electrode possessed remarkable photocurrent stability (5%

loss over 20 min) compared to that made with bare $GaInP_2$ (almost no photocurrent after 20 min).[12] $GaInP_2$ electrodes coated with only Pt were also studied as a reference, and they exhibited an unstable current and diminished catalytic activity.[257, 258] The decrease in performance was attributed to inadequate and nonuniform surface coverage of the catalyst and the formation of a passivated Pt hydrated species. When 35 nm of amorphous ALD-TiO_2 was deposited as an intermediate layer between the $GaInP_2$ and Pt, stable photocurrent density and robust catalytic activity was realized.[12] In another study, improved catalytic activity and stability were achieved when an amorphous TiO_2 buffer layer was inserted between ferroelectric $BiFeO_3$ (BFO) and a Pt catalyst (**Fig. 17a** and **17b**).[259] An upward barrier (i.e. upward band edge bending) formed between the BFO and Pt (**Fig. 17c** and **17d**), which impeded electron transfer from the electrode to the electrolyte. The insertion of amorphous TiO_2, with its good conductivity and its suitable work function,[260] has been reported to improve stability of photocathodes during photoelectrocatalytic water splitting by removing the upward barrier and facilitating photogenerated carrier separation. Moreover, tunneling has been reported at the amorphous TiO_2/electrode (i.e., Pt) contact due to the ultra-low thickness of amorphous TiO_2.[260] Similarly, an identical amorphous TiO_2 buffer layer between $PbTiO_3$ and Pt was also shown to facilitate removal of the upward barrier between $PbTiO_3$ and Pt.[261]

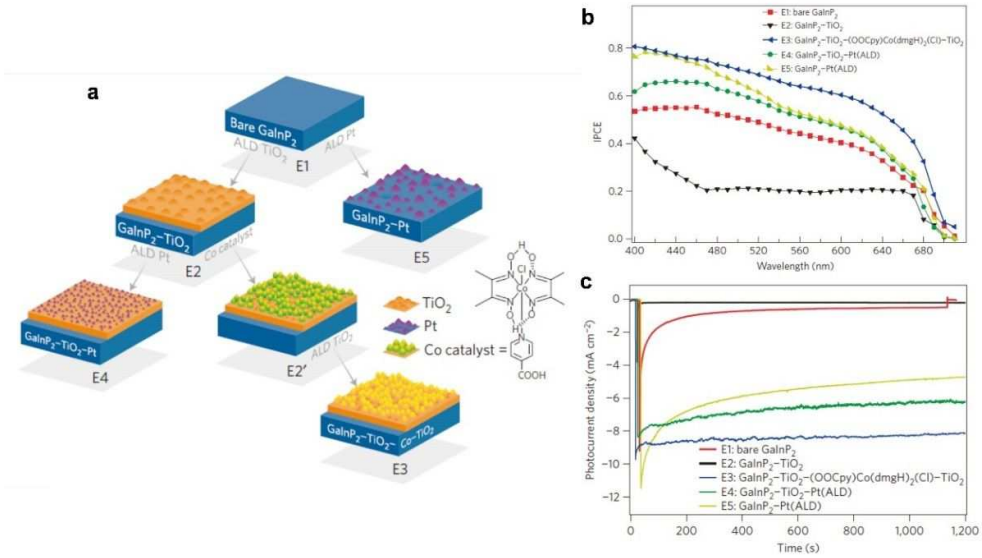

Fig. 16 (a) Modification strategies for p-$GaInP_2$ photoelectrodes. (b) IPCE of electrodes at -1 V versus Ag/AgCl in pH=13 aqueous solution. (c) Current density-time profile of electrodes at -1 V versus Ag/AgCl under 1-sun illumination. Reproduced from ref. 12 with permission from Springer Nature, copyright 2016.

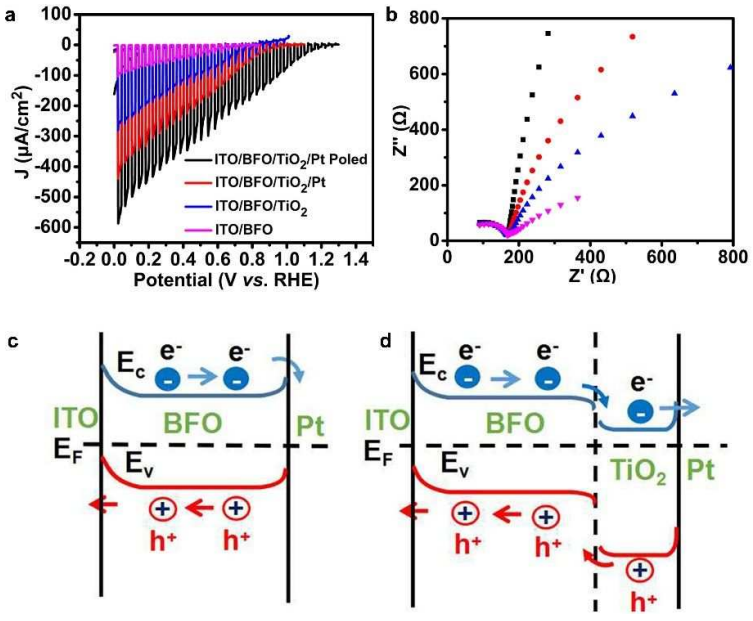

Fig. 17 (a) J-V curves, (b) EIS curves for ITO/BFO/Pt and ITO/BFO and ITO/BFO/TiO_2/Pt photoelectrodes. Schematic band diagrams for (c) ITO/BFO/Pt and (d) ITO/BFO/TiO_2/Pt

photocathodes. Reproduced from ref. 259 with permission from AIP Publishing, copyright 2017.

The combination of amorphous TiO_2 with other materials was also investigated to further improve the stability of electrodes in PEC applications. For example, graphene has been widely used to inhibit corrosion of metals.[262, 263] A CVD graphene was employed as a protective layer against photocorrosion for a Cu_2O photocathode.[252] The deposition of graphene layers onto the rough surface of Cu_2O was observed to induce the formation of microcracks, which facilitated deleterious direct contact between the electrolyte and Cu_2O.[252] To block the microcracks and form a protective bilayer, an additional amorphous TiO_2 layer was deposited on the top of the graphene. The TiO_2/graphene protected Cu_2O photocathode generated twice the photocurrent as compared to the bare Cu_2O electrode, which was attributed to the type II band structure and electron selective nature of the protective amorphous TiO_2/graphene bilayer.[252]

Recently, a black TiO_2 composed of crystalline TiO_2 with graded oxygen defects was employed as a protected layer in silicon-based photocathodes.[264] The graded oxygen defects can activate and enhance the PEC behaviors of Si-based photocathodes by forming electrically conducting channels that allow photogenerated electrons to reach the surface of a photocathode with low resistance. The protection layer, with its high-density structure, was found to enhance the lifetime of the photocathodes in both strong acid and alkaline electrolyte solutions. The silicon-based photocathode with the black amorphous-crystalline TiO_2 protective layer showed a current density of ~35.3 mA cm^{-2} and stability of over 100 h at 10 mA cm^{-2} in 1.0 M NaOH

electrolyte. In contrast, no photoelectrocatalytic behavior was observed for the photocathode using a pure crystalline TiO_2 protection layer.[264] This was ascribed to an up-shift in the valence band edge of TiO_2 which resulted from the oxygen defects in the disordered structure (amorphous phase) of black TiO_2.[75, 265] The tail effect narrowed the bandgap of the black TiO_2. The difference of CB minimum and VB maximum between Si and black TiO_2 (**Fig. 18**) allows for electrons to move easily through the conduction band, whereas the transport of holes from Si to TiO_2 is blocked due to a large barrier in the valance band.[264]

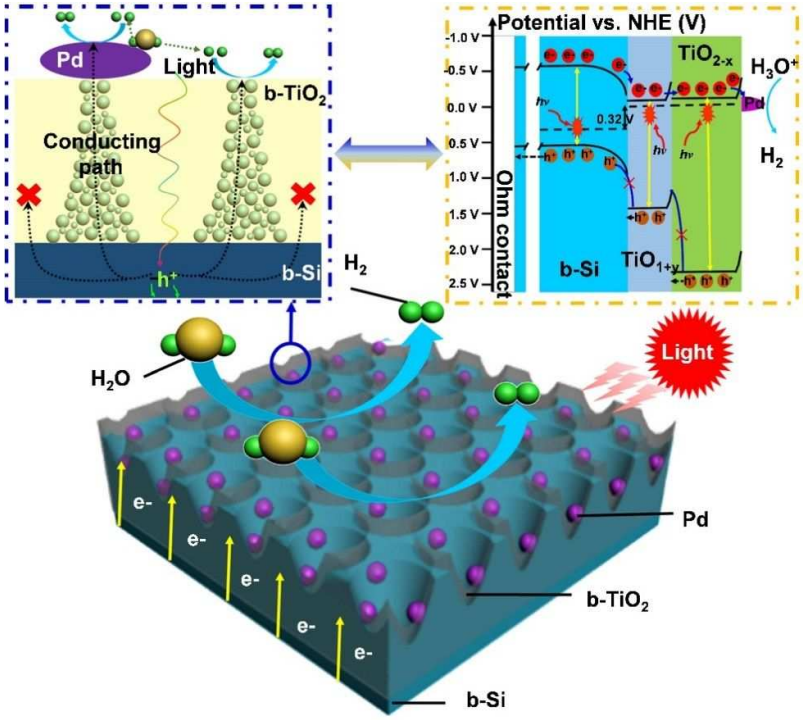

Fig. 18 Schematic and the proposed energy band diagram of Pd nanoparticle/black TiO_2 (b-TiO_2)/black Si (b-Si) photocathode for water reduction. TiO_{1+y} and TiO_{2-x} are the b-TiO_2 layer composed of two kinds of stoichiometric Ti:O as well as graded oxygen defects. Reproduced from ref. 264 with permission from AIP Publishing, copyright 2018.

4.2.2 Amorphous MoS_x Photocathodes

Amorphous molybdenum sulfide (MoS_x) has been proven to be a highly active catalyst for HER in acidic solutions.[266-268] This class of catalyst is especially competitive for the development of cost-effective PEC hydrogen generation devices because MoS_x can be prepared in simple and mild conditions using readily available and inexpensive precursors with excellent chemical stability. The free energy of the hydrogen adsorption on the edge sites of MoS_x is theoretically close to that of Pt, which suggests MoS_x is a promising HER catalyst.[269] Hu et al. showed that an amorphous MoS_x catalyst could deliver a current density of 20 mA/cm^2 at an overpotential of 170 mV and a loading of 0.2 mg/cm^2.[267] A Cu_2O electrode combined with amorphous MoS_x catalyst (the devices structure is shown in **Fig. 19a-19d**) was found to produce a maximum photocurrent of 14.7 mA/cm^2 and exhibit a maximum solar to hydrogen efficiency of 18% under 1 sun irradiation.[4] Such performance is comparable to that of Pt nanoparticles[211, 270] and RuO_x[271] deposited on a Cu_2O photocathode. In addition, the MoS_x catalyst showed improved stability in PEC hydrogen production under acidic conditions in comparison with Pt, as shown in **Fig. 19e**.[4] Gu and Turner et al. deposited a bilayer of amorphous TiO_x and MoS_x onto $GaInP_2$ as a photocathode, and it showed high catalytic activity and stability (remaining 80% of initial photocurrent density during a 20 h durability test) similar to that of crystalline MoS_2 (for the hydrogen evolution reaction).[257] Despite the excellent catalytic activity and stability, it is still difficult to recognize the atomic structure and clarify the detailed catalytic mechanisms due to the disordered structure of amorphous MoS_x. For example, H_2 evolution by amorphous MoS_x may proceed via a different mechanism than

that of MoS_2 crystals.[272-274]

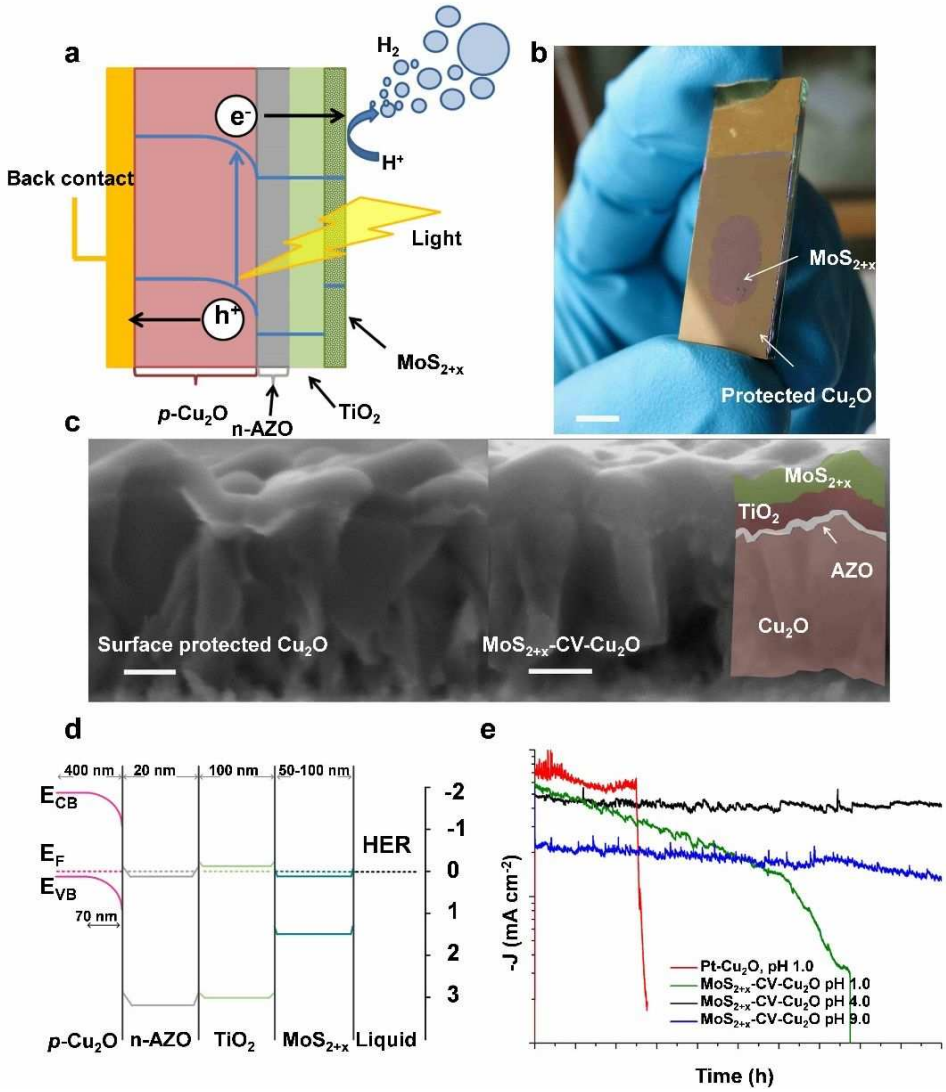

Fig. 19 (a) Schematic structure and (b) an image of the MoS_x-CA-Cu_2O photocathode; Scale bar, 5 mm. The area covered with the MoS_x catalyst (66 mg cm^2) is in the middle of the photoelectrode and is approximately 0.48 cm^2. (c) Cross-sectional SEM image of the protective layers, Scale bars, 200 nm. (d) Band energy for the Cu_2O photocathode with Al-doped ZnO (AZO) and TiO_2 and the MoS_x catalyst film biased at 0V versus RHE, assuming the pinning of the band edges of the semiconductor at the interfaces; (e) Photocathode stability at 0 V versus

RHE for Cu_2O photocathodes modified by different HER catalysts under constant AM 1.5 illumination. Reproduced from ref. 4 with permission from AIP, copyright 2014.

The edges of MoS_2 single crystals have undercoordinated Mo and/or S atoms that have been recognized as active sites.[275] Similarly, unsaturated S atoms in amorphous MoS_x were identified as the catalytically active sites for the hydrogen evolution reaction.[266] Lin et al. synthesized nanocomposites of amorphous MoS_2 and multi-walled carbon nanotubes (MWCNTs) for the hydrogen evolution reaction.[276] Based on the capacitance and impedance measurements, MoS_x with an amorphous structure exhibited higher activity than crystalline MoS_x due to the fact that the former had a higher number of exposed edges with unsaturated sulfur atoms.[276] Tran et al. prepared active amorphous MoS_x consisting of discrete thiomolybdate $[Mo_3S_{13}]^{2-}$ building blocks (characterized by transmission electron microscopy) which share terminal disulfide ligands, as shown in **Fig. 20**.[274] The thiomolybdate can be viewed as a fragment of the MoS_2 structure with a significant number of active sites because most sulfur atoms in the structure exhibit a structural motif similar to that observed at MoS_2 edges.[277] Elimination of terminal disulfide ligands generated the actual catalytic centers for proton reduction, which were found to hydrate and generate molybdenum oxysulfide sites.[278]

The morphology of amorphous MoS_2 in photocathodes has a significant impact on the performance of PECs.[279] A conformal film-like morphology was prepared by electrodeposition starting from cathodic potential. The film was more suitable for efficient catalytic activation than a nonuniform particulate structure prepared by the same method but

starting from anodic potential.[279] The morphology difference was caused by the different initial reactions. Under cathodic potential, MoS_2 yields through the reduction of MoS_4^{2-}, while the initial reaction under anodic potential generates MoS_3 through the oxidation of MoS_4^{2-}. As a result, the TiO_2/Sb_2Se_3 photocathode with film-like morphology MoS_x demonstrated 4 times higher photocurrent density (4.8 mA cm^{-2} at 0 V_{RHE}) than its nonuniform counterpart (1.1 mA cm^{-2} at 0 V_{RHE}). Clearly, more study into the effects of morphology of amorphous semiconductors on their performance in photoelectrodes is needed.

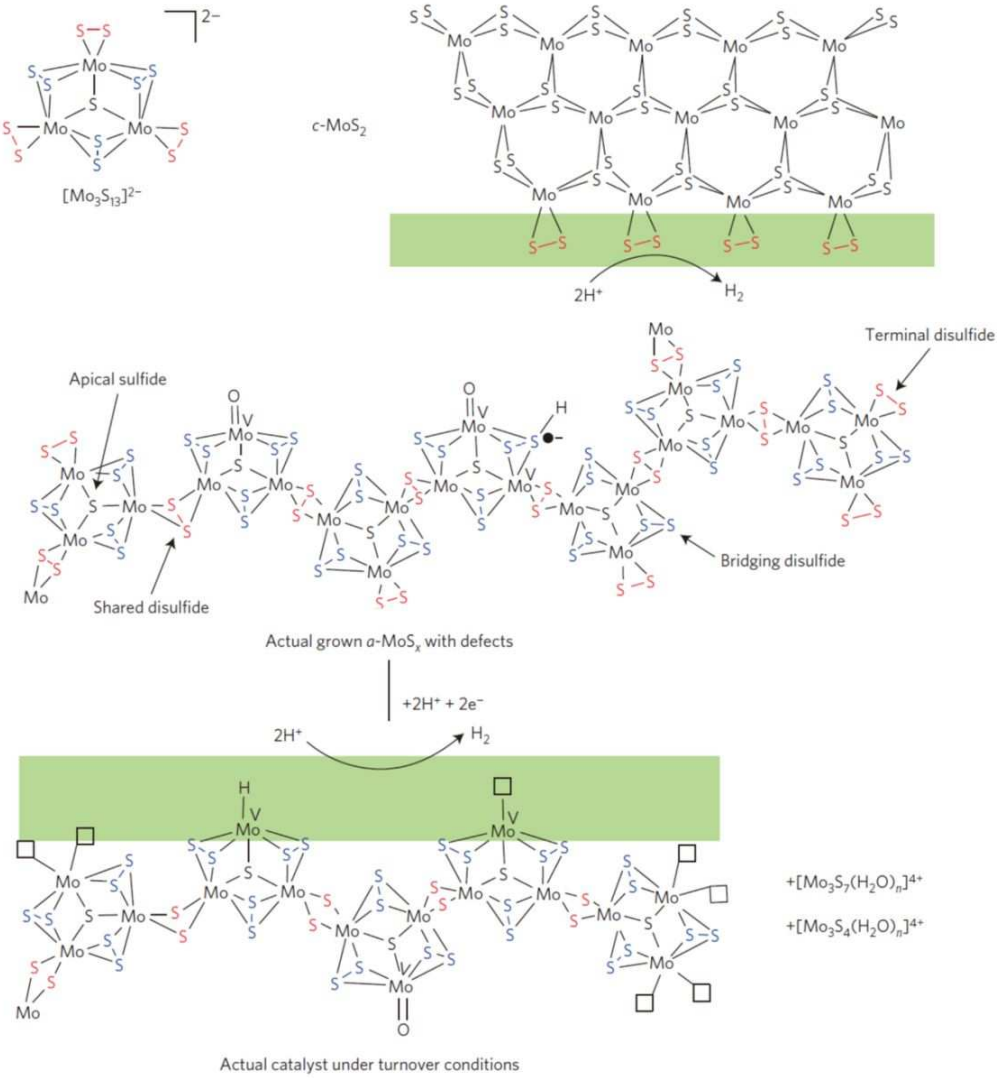

Fig. 20 Structures of MoS_x materials. Top left: $[Mo_3S_{13}]^{2-}$ cluster. Top right: crystal MoS_2, wherein the Mo edge contains $Mo(S_2)$ catalytic active sites. Center: amorphous MoS_x coordination polymer with $[Mo_3S_{13}]^{2-}$ building block units sharing two of their three terminal disulfide bonds to form a polymeric chain. Some defect sites are present within the polymer. Bottom: MoS_x under catalytic H_2 evolution turnover conditions. Within a-MoS_x, four different ligands are thus identified: apical sulfide μ-S^{2-}, bridging disulfides $(S\text{-}S)^{2-}_{br}$, shared $(S\text{-}S)^{2-}_{sh}$ and terminal disulfides $(S\text{-}S)^{2-}_{t}$. Reproduced from ref. 274 with permission from Springer Nature, copyright 2016.

4.2.3 Other Amorphous Inorganic Semiconductor Photocathodes

To improve PEC device efficiency, organic PEC and hybrid organic/inorganic PEC systems based on organic semiconducting polymers as absorbers for H_2 production have emerged.[10, 280-282] Fonzo et al. demonstrated a hybrid organic/inorganic photocathode (**Fig. 21a** and **21b**) in which a P3HT:PCBM blend photoactive material was sandwiched between an amorphous TiO_2 electron selective layer (ESL) and a compact amorphous WO_3 hole selective layer (HSL).[10] One of the drawbacks of WO_3 as a HSL is its wide band-gap, which induces a low charge carrier concentration and inefficient electron injection. Using an electrochemical intercalation process can improve charge carrier concentration by several orders of magnitude by inducing protonated and partially reduced states in WO_3.[283] Amorphous WO_3 was protonated by the intercalation of H^+ cations into the oxide lattice to form metal-like hydride

phases (H_yWO_x) during forward scans (toward the cathodic potential). The intercalation of protons increased the majority carrier concentration and improved electron charge transport, leading to higher conductivity.[284] As shown in **Fig. 21c**, the work function was reduced because the intercalation of protons strengthened the n-type nature of amorphous WO_3 and created sub-bandgap defect states. The intercalated H_yWO_x phases, where hydrogen atoms form interstitial or bound states, can form gap states via oxygen vacancies[285, 286] or polarons (**Fig. 21e**).[287] The amorphous structure of WO_3 allows the intercalated protons to be completely extracted from the lattice without damaging the film.[288] The increased electron injection barrier induced by the deep intercalation and reduction in the organic/inorganic PEC of P3HT:PCBM caused a slow-paced degradation of the photocurrent in aqueous acidic electrolyte.[10] Moreover, the thickness of the amorphous WO_3 had great impact on the performance of HER and determined the transparency of films, as is shown in **Fig. 21f**. The device with 100 nm of amorphous WO_3 was determined to possess the optimal thickness.

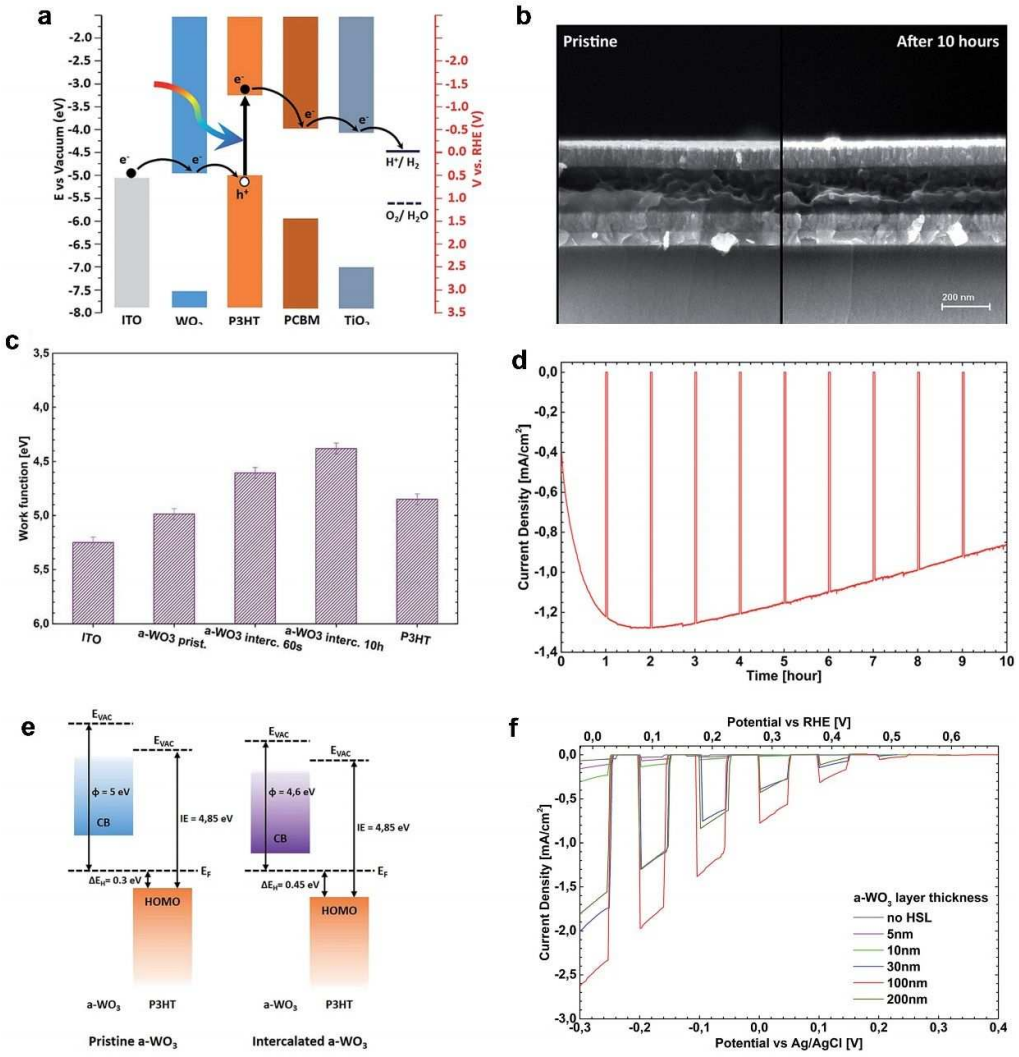

Fig. 21 (a) Schematic of the energetic structure of the hybrid photocathode. (b) Scanning electron micrograph cross-sectional image of the photocathode composed of ITO, WO_3, P3HT:PCBM, TiO_2, Pt layer from bottom to top. (c) Work function of ITO/WO_3 (100 nm) films before and after electrochemical intercalation. (d) Photocurrent density during potentiostatic operation for the full hybrid photoelectrode architecture ITO/WO_3/P3HT:PCBM/TiO_2/Pt. (e) Energy level alignment of the WO_3/P3HT interfaces before and after the electrochemical intercalation process. (f) Photoelectrocatalytic device characterization *versus* the thickness of the amorphous WO_3 hole selective layer. Reproduced

from ref. 10 with permission from Royal Society of Chemistry, copyright 2017.

ZrO_2 has also been used as a photocathode in water splitting applications due to its good photo-reduction ability, compatible band-edge positions, low cost, and satisfactory stability in both acidic and alkaline media.[289, 290] However, its large bandgap limits photoconversion efficiency in the visible region of the solar spectrum. Using ZrO_2 with a crystalline-core/amorphous-shell structure was found to boost efficiency because the abundant surface defects and lattice dislocations of amorphous shell were observed to create new states in the bandgap[291] and form a large number of reaction sites.[5] An amorphous shell can absorb light in the visible range more strongly than a crystalline counterpart, resulting in the generation of a large number of charge carriers inside the shell.[292] Then the carriers transport into the crystalline core for improved electrical conductivity. Leung et al. developed a HF post-treatment to synthesize a thin amorphous ZrO_2 shell with a high amount of oxygen deficiencies on the surface of crystalline ZrO_2 nanowires.[290] The amorphous ZrO_2 significantly improved carrier transport and provided an abundance of active sites. The as-grown amorphous-crystalline ZrO_2 hierarchical nanowire photocathode showed a photocurrent density of -12.9 $mA \cdot cm^{-2}$ at 0 V_{RHE}. Intriguingly, channel cracks and buckling occurred in the films as shown in **Fig. 22**, where the underside surface was also coated with an amorphous layer.[290] Such a layer allowed direct contact between the film and the Si substrate, which in turn reduced the diffusion length of photogenerated carriers and improved the charge carrier collection. On the

other hand, an increase in contact with the electrolytes can increase the back electron transfer from solution to collector.[293]

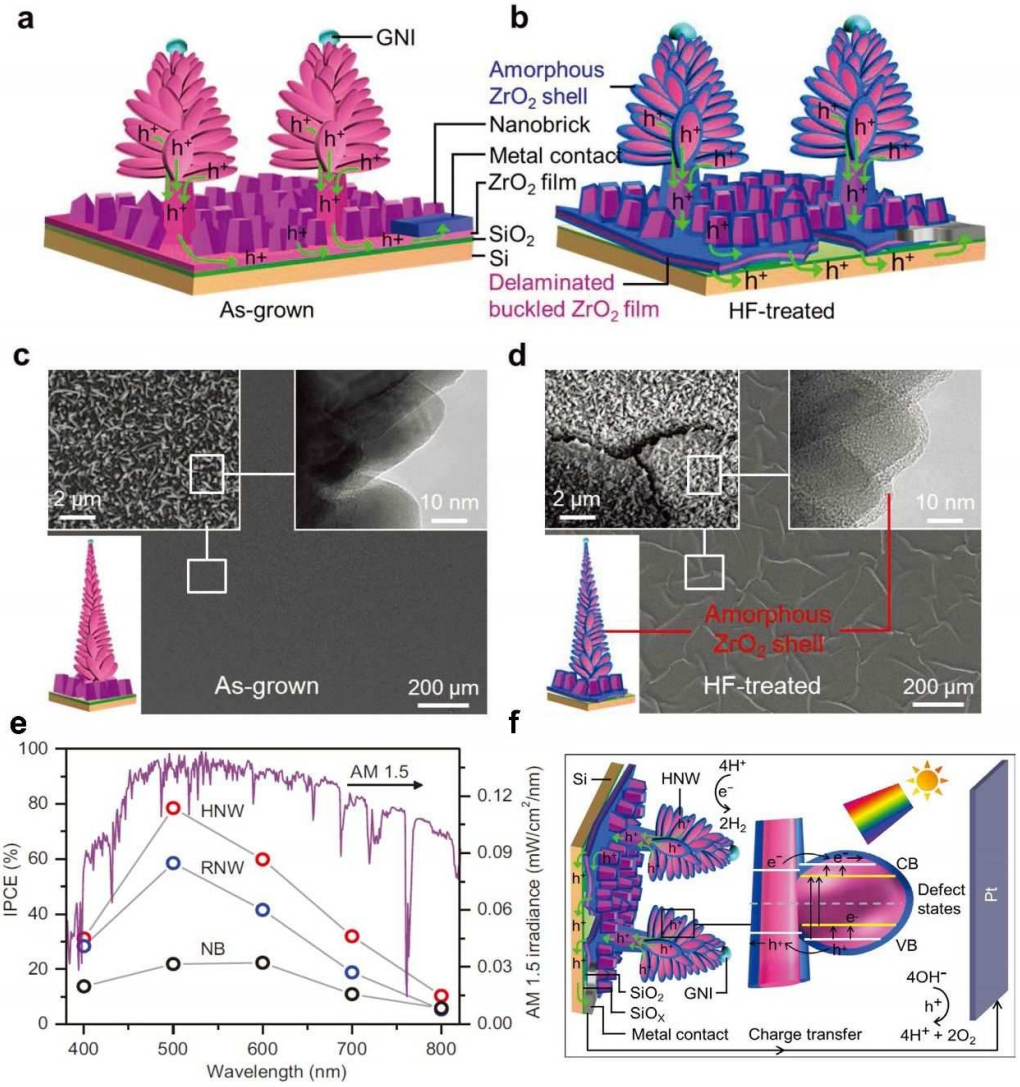

Fig. 22 Schematic and SEM of hierarchical nanowire film **(**a, c) before and (b, d) after the HF treatment. (e) IPCE profiles of HF-treated ZrO_2 hierarchical nanowire (HNW), regular nanowire (RNW), and nanobrick (NB) films as functions of wavelength. (f) Schematic for the charge separation and transfer process in the nanoplates of the HF-treated ZrO_2 hierarchical nanowires in a photoelectrocatalytic water splitting reaction driven by visible light irradiation.

Reproduced from ref. 290 with permission from John Wiley and Sons, copyright 2017.

5. Photocatalytic Decomposition of Organic Contaminants

5.1 Amorphous-Crystalline TiO_2 as Photocatalyst for Organic Contaminant Degradation

Amorphous TiO_2 has been reported to be an inefficient photocatalyst for degradation of organic contaminants. Garshev et al. found that amorphous TiO_2 readily adsorbed organic contaminant molecules but exhibited negligible photocatalytic activity.[294] The partial removal of the amorphous phase led to a significant increase in activity.[294] Tanaka et al. also observed negligible activity for organic compound degradation when using amorphous TiO_2 in comparison with crystalline TiO_2 samples.[24] In photocatalytic degradation of organic contaminants, the adsorption of molecules on a TiO_2 surface is important.[295-298] Despite inactive photocatalytic properties, amorphous TiO_2 possesses better adsorption of organic molecules compared to their crystalline counterpart.[299] A density functional tight-binding study of organic molecule attachment to TiO_2 *via* carboxylic groups (acetic acid) was reported for crystalline and amorphous surfaces of titania. Amorphous TiO_2 achieved strong anchoring of organic molecules.[299] In addition, when compared to crystalline TiO_2, crystalline/amorphous TiO_2 has a lower energy bandgap, which can generate active species (i.e., hydroxyl radicals, superoxide anions) during photocatalytic degradation of organic contaminants under visible and infrared illumination.[300] Thus, the coexistence and arrangement of crystalline and amorphous phases may play an important role in the photocatalytic performance of TiO_2.[301]

Acid treatment has been shown to create amorphous surfaces on crystalline TiO_2 and further increase its adsorption and photocatalytic ability.[302, 303] Acid treatment of TiO_2 nanoparticles has been found to increase the concentration of hydroxyl group on their surfaces.[299] These hydroxyl groups serve as Brønsted acid sites (proton donor) whose dissociation can result in a drop in the pH level of solutions and thus protonate the target molecules. Apart from using acid treatment to fabricate amorphous-crystalline structures, Kim et al. synthesized a reduced TiO_2 composed of amorphous, rutile, and anatase phases at room temperature using lithium (Li) and ethylenediamine (EDA) as etching agents to treat P25.[300] The reduced TiO_2 with amorphous structure was found to generate reactive oxygen radicals (such as hydroxyl radicals) in the photocatalytic degradation of organic pollutants under solar irradiation. The oxygen defects on the amorphous surface of reduced TiO_2 were observed to function as hole traps, which inhibited carrier recombination and reduced its bandgap.[300]

5.2 Amorphous TiO_2-Based Composite Photocatalysts for Organic Contaminant Degradation

As noted above, the introduction of an amorphous phase can facilitate the partial oxidation reaction of organic molecules.[22] Selective aerobic oxidation of benzylic alcohols with moderate to high yields (32-100%) was realized *via* incorporation of amorphous TiO_2 within a mesoporous metal-organic framework (MOF).[304] The mild reaction condition (under sunlight irradiation in an oxygen atmosphere) led to the reaction of other electron-rich and electron-poor benzylic alcohols. Similarly, when coating amorphous TiO_2 into a mesoporous

organosilicate framework (channel), the photocatalytic performance was improved during aerobic regeneration of carbonyl compounds from oximes under sunlight irradiation compared to the catalyst without amorphous TiO_2.[305]

The photocatalytic activity of amorphous and crystalline TiO_2 have been enhanced *via* noble metal deposition and by incorporation of a sensitizer. Homogeneous loading of noble metals (e.g. Ad, Pt, Au, Pd etc.) onto TiO_2 matrices can tune the photophysical properties of the final material. [306-308] Compared to TiO_2, the higher work functions of the noble metals induced Schottky barriers at the TiO_2-metal interface.[309] This barrier suppressed electron migration from TiO_2 to the metal via a tunneling effect and prevented electron transfer from the fermi level of metal to the conduction band of TiO_2. As a result, the photocatalytic activity of the noble metal-loaded TiO_2 can be optimized. Based on a colloidal synthesis route, an amorphous TiO_2 matrix may be loaded with Pt nanoclusters[307] or Ag nanoparticles.[308] The photocatalytic activity of the Pt/Ag-amorphous TiO_2 towards the degradation of organic dyes was improved compared to other reported Pt/Ag-crystalline TiO_2. Amorphous TiO_2 matrix leads to dispersed impregnation of Ag nanoparticles, and thus forms multiple metal-metal oxide interfaces, which results in the decreased recombination of the photo-generated electrons and holes at the interface. Anchoring sensitizers onto the semiconductor surface has also been proven to be an efficient approach to develop a cost-effective visible light active semiconductor photocatalysts. Electrons are first generated by light absorption in the photosensitizer and then injected into the conduction band of the semiconductor where they react with target molecules. A useful molecular sensitizer should anchor firmly on the semiconductor, be highly stable,

efficiently absorb light in the visible region, and possess a sufficiently negative excited-state redox potential for electron injection into the conduction band of the semiconductor. Silver halides (AgX, X: Br, I) are well-known as visible-light photosensitive materials. Loading AgX onto the surface of TiO_2 has been shown to inhibit the decomposition of the photosensitizer *via* electrons transformation to O_2 instead of Ag^+.[310] Compared with anatase and P25, amorphous TiO_2 was found to be optimal for preserving the stability and high activity of AgI under visible light irradiation for the photodecompostion of organic dyes and photoreduction of Cr(VI),[311] which was attributed to the large surface area, negative shift of flat band potential, and lower charge transfer resistance of amorphous TiO_2.[311] Excellent photocatalytic activity for degradation of organic pollutants was also achieved by anchoring other sensitizers such as curcumin [312] and CdS quantum dots [313] onto amorphous TiO_2.

6. Photocatalytic CO_2 Reduction Based on Amorphous Phase Photocatalysts

Semiconducting photocatalysis converting CO_2 into high value-added carbon-based fuels, such as methane or methanol, is a potential method to harvest and utilize solar energy.[314] The major challenge of CO_2 photoreduction, however, is its low yield, poor selectivity, and difficultly of activating its highly-stable C=O bonds.[315, 316] Theoretical and experimental results have suggested that oxygen vacancies (V_o) in semiconductors are highly reactive and are capable of activating and even splitting CO_2.[26, 317-321] Black hydrogenated TiO_2:H is known to possess abundant surface defects (such as oxygen vacancies or disordered shells) which efficiently enhance its catalytic performance and result in the intermediate state (Ti−H).[322, 323]

In situ diffuse reflectance infrared Fourier transform spectroscopy (DRIFTS) showed that hydrogenated TiO_2:H with an amorphous shell can efficiently accelerate the adsorption and chemical activation of CO_2 molecules. This in turn facilitated electron injection from TiO_2:H to the adsorbed CO_2 molecule which formed excited CO_2^- (**Fig. 23**). Crystalline-core/amorphous-shell TiO_2:H catalysts produced 9 times more CH_4 than crystalline TiO_2.[26, 320] Another Al-reduced black titania with crystalline-core/amorphous-shell structure (TiO_2@TiO_{2-x}) was found to be efficient in photocatalytic reduction of CO_2 to CH_4.[320] The numerous surface V_o in the unique TiO_2 material facilitated the adsorption and chemical activation of CO_2 molecules. Photocatalytic reduction of CO_2 was also studied using black brookite nanosheets formed by introducing a large amount of Ti^{3+} defects in a brookite phase.[324] The black brookite TiO_{2-x} displayed drastically enhanced visible-light absorption and exhibited excellent photocatalytic activity toward CO_2 reduction due to its enhanced light absorption, efficient charge separation, and well aligned band edges. Selectivity of CO_2 reduction products can be improved by utilizing amorphous TiO_2 phases as the photocatalysts.[325, 326] Black TiO_2 exhibited a threefold increase in CH_4 production rate over pure TiO_2.[327] Better selectivity has also been realized by fluorinating black TiO_{2-x}.[315] Fluorination enabled the replacement of oxygen vacancies with F atoms in the lattice interval of TiO_{2-x}. The electronegativity of the doped fluorine atoms was observed to attract electrons from neighboring Ti^{3+}, which generated a built-in electric field between substitutional F and Ti^{3+}.[315] Thus, the Ti^{3+} impurity level is upward in the electric field, leading to the enhanced reduction potential of photoexcited electrons. The fluorinated black TiO_{2-x} increased CH_4 production yield 13-fold, from 0.125 to 1.63 μmol/g·h,

under solar light illumination. Additionally, CH_4 selectivity was increased 3-fold, from 25.7% to 85.8%.[315]

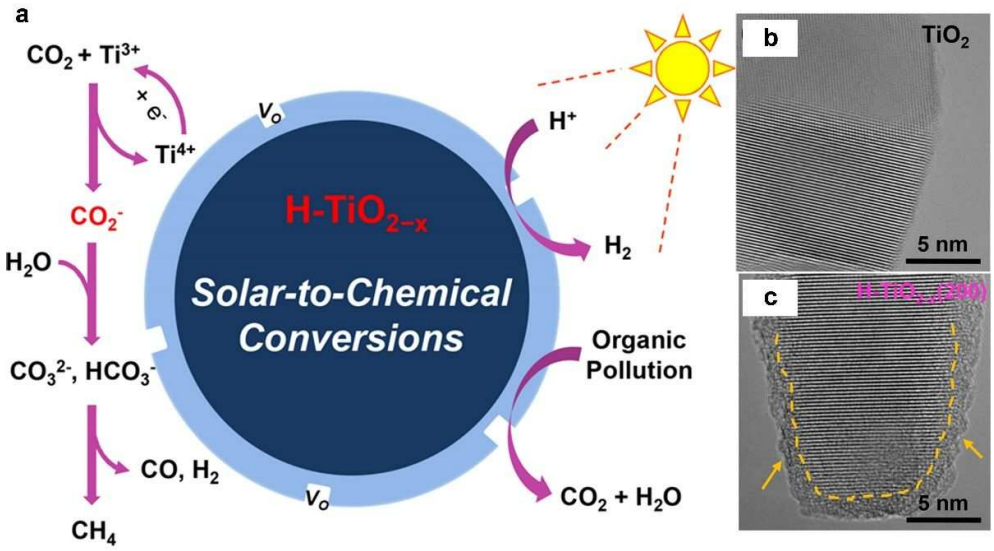

Fig. 23 (a) Possible reaction pathways for the photoreduction of CO_2 with H_2O using TiO_2:H. HRTEM images of (b) pristine TiO_2 and (c) TiO_2:H samples. The amorphous shells are marked with arrows. Reproduced from ref. 26 with permission from American Chemical Society, copyright 2017.

Oxygen vacancies have been explored for their catalytic enhancement in other amorphous semiconductors. For example, V_O were generated in an amorphous Zn-Ge-O semiconductor *via* a photocorrosion reaction to activate oxygen atoms in CO_2 molecules.[321] As shown in **Fig. 24**, charge carriers can be photogenerated in the amorphous α-Zn-Ge-O semiconductor photocatalyst. The photogenerated holes in the valence band can then oxidize the lattice oxygen

in Zn-Ge-O catalysts. The newly formed V_o is then able to react with the O of CO_2, filling the vacancy sites of α-Zn-Ge-O. The photogenerated electrons in the conduction band also reduce the C atoms of CO_2 to solid C.[321] The defect reaction is sustained by continuous photogenerated hole oxidation of surface oxygen atoms on amorphous Zn-Ge-O.[321]

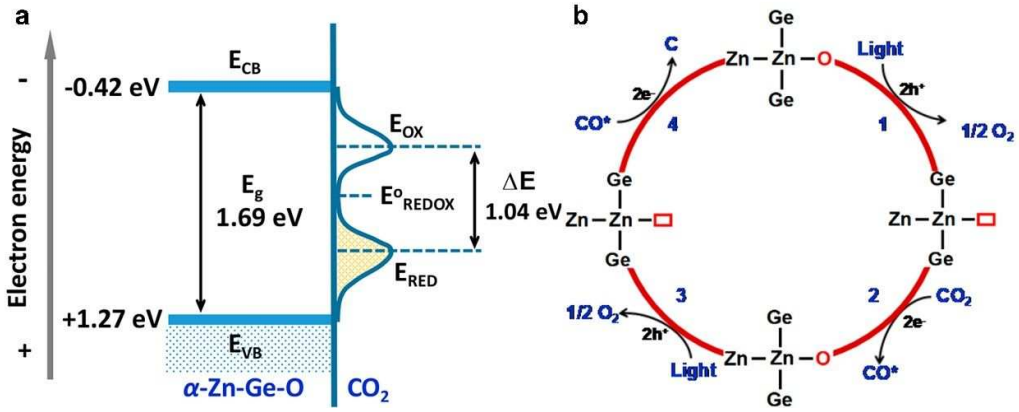

Fig. 24 (a) Energy levels for redox electron transfer reaction for CO_2 splitting on α-Zn-Ge-O photocatalyst. (b) Proposed mechanism for CO_2 splitting into solid carbon and O_2 over α-Zn-Ge-O under irradiation. Reproduced from ref. 321 with permission from American Chemical Society, copyright 2018.

7. Conclusion and Outlook

In this review, recent advances in amorphous inorganic semiconductor-based materials for applications in solar cells, photoelectrocatalysis and photocatalysis have been summarized. Amorphous phase materials have been found to improve efficiency and stability in three primary ways. First, a layer of amorphous phase provides sufficient surface coverage and simultaneously minimizes the resistance of charge transfer between the material and liquid

solutions.[52] Amorphous materials have a high specific surface area that physically bridges the gaps between the bulk heterojunctions to maintain electrical contact and lower interfacial resistance. The introduction of amorphous phases to photoconversion devices increases their efficiency by maximizing light collection and photoconversion by rapidly extracting photogenerated charges from photo-absorbing materials and by inhibiting change carrier recombination. Second, amorphous semiconductors are more conductive because electrons in the band tail states can easily be excited into a high-mobility state. While crystalline semiconductors must rely on band gap conductivity, amorphous phases can also use hopping conductivity. In hopping conductivity, electrons in localized states can transport through the band gap into delocalized states. Improved conductivity of amorphous semiconductors suppresses tunneling barriers, increases photocurrent, and decreases the required overpotential.[19, 20] The low tail and midgap states in amorphous phases can suppress charge recombination and yield electron-selective interfacial layers.[153, 154] Furthermore, hole diffusion can be triggered across amorphous semiconductor layers through O-O peroxy linkages.[227] Lastly, an amorphous phase coating can protect devices from corrosive redox coupling. The ability to tune the energy levels and distribute defect states in coatings offers the opportunity to better stabilize photoconversion devices. Despite these advances, studies of amorphous inorganic semiconductor materials for photoconversion applications are still in their infancy, and many issues and challenges need to be overcome.

First, the structural framework of functional amorphous semiconductors, such as defect types, compositions, active sites should be scrutinized. The photo-absorption and conversion

performances of solar cells, PECs, and photocatalysts rely heavily on the surface microstructure of materials. The same amorphous semiconductors with different microstructures (such as defect types) may result in vastly different performances in solar cells[149, 150, 171, 174], photoelectrocatalysis[239] and photocatalysis[24, 294, 300, 301]. More in-depth investigation into midgap states, which are created by defects in amorphous semiconductors, should be conducted. There are two kinds of midgap states in amorphous phase, shallow level states and deep level states, depending on their relative energetic positions from the band edge (**Fig. 25**). The ionization energy of shallow states is about K_bT (K_b is the Boltzmann's constant and T is the temperature), but it is several K_bT for deep states. Shallow states generally act as dopants and are classified as donors or acceptors based on whether their energy level sits just below the conduction band or just above the valence band, respectively. Donors can donate electrons to the conduction band, whereas acceptors accept an electron from the valence band, achieving the separation of electrons and holes. In contrast, deep states generally serve as recombination centers because their ability to capture electrons and holes is equal. Therefore, to optimize the performance of prepare amorphous semiconductors, it is critical to maximize shallow states and minimize deep ones. Another aspect of the framework of amorphous semiconductors that needs further investigation is compositional tuning.[8] From a technological viewpoint, it should be easier to tune the optical band gaps, trap states and work functions for amorphous semiconductors with multiple cation compositions (such as ternary and quaternary components). Thus, the structural framework of amorphous semiconductors can be rationally designed by tuning their compositions to create more active sites and optimize the physical

properties for a variety of applications.

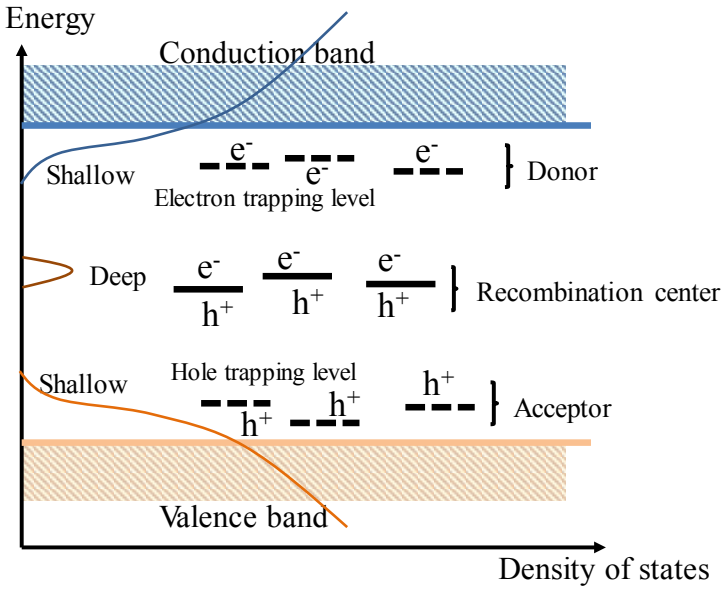

Fig. 25 Schematic spatial and energy diagram of an amorphous inorganic semiconductor with localized trap states in the bandgap.

Second, more attention and exploration of the electronic and optical properties of amorphous semiconductors are needed to fully understand their role in photoabsorption and photoconversion. Such study will further reveal new potential applications for amorphous materials. Detailed experimental techniques and theoretical studies will be beneficial for investigating how the electronic interactions between amorphous materials or amorphous/crystalline interfaces affect charge extraction and transport. Several experimental techniques have already been developed to scrutinize the electronic and optical properties of amorphous semiconductors, including space-charge limited current measurements, impedance

spectroscopy, photoemission spectroscopy, deep level transient spectroscopy, photothermal deflection spectroscopy, electric force microscopy and Kelvin probe force microscopy. These techniques have enabled the extraction of trap parameters like trap states and their energetic/spatial distribution. In depth understanding of all trap parameters is critical because traps significantly contribute to carrier pathways in amorphous semiconductors. A challenge for this study, however, is that the lack of periodicity and complex atomic structure of amorphous semiconductors are difficult to model and explore through DFT. However, electronic states in amorphous semiconductors can be treated by tight-binding approximations and Hartree–Fock calculations.[328, 329] These approaches have given insights into how spatial fluctuations of structural parameters (such as bond length, bond angle, and dihedral angle) result in band tails by broadening the bottom of the conduction band and the top of valence band. While some progress has been made towards exploration of the electronic and optical properties of amorphous semiconductors, new techniques and models are needed to fully characterize and understand local spatial distribution and atomic structure.

Third, unlike crystalline materials, amorphous inorganic semiconductors lack standardization during preparations, resulting in different results batch-to-batch. The type and density of defects are difficult to control precisely because they are determined by many factors such as chemicals, instruments, reaction temperature, humidity, etc. Small fluctuations in these reaction conditions could lead to significant microstructure change in inorganic semiconductors, which further affect their performance. Compared with other techniques for the preparation of amorphous semiconductors (see section 2 of the manuscript), ALD is the

best choice for precise control of the microstructures of amorphous inorganic semiconductors.

Fourth, the boundary between crystalline and amorphous phases is ambiguous. While it is well known that the major difference between amorphous and crystalline materials is long-ranged structural order, the phase-transition region between amorphous and crystalline phases is wide, which obscures clear delineation. Crystallinity can range from 0% (ideal amorphous phase) to 100% (ideal crystalline phase), but most materials fall somewhere between these extremes with both crystalline and amorphous structures (see Fig. 26). Currently, no valid technique can quantify the extent of structural similarity/difference between amorphous and crystalline phases. This is partly due to the limited experimental characterization of amorphous structures and the inability of structural models to simulate the correct amount of randomness in amorphous systems. Elliott et al. developed a Smooth Overlap of Atomic Positions (SOAP) method to quantify the structural similarity between amorphous and crystalline TiO_2,[330] which may provide a method for quantifying and defining the boundary between amorphous and crystalline phases in the future.

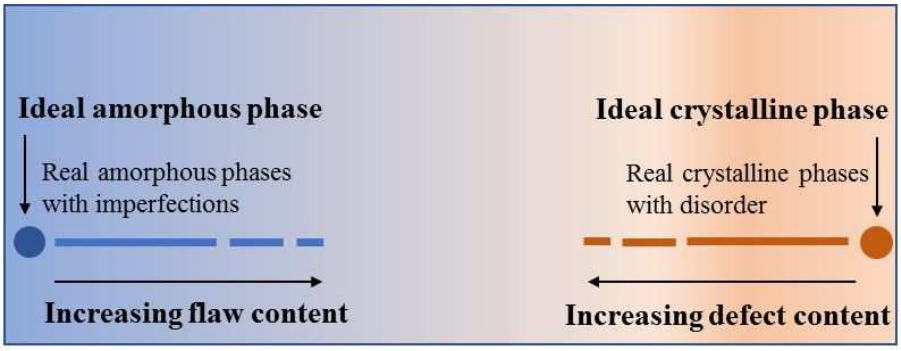

Fig. 26 A view of the structure of solids along an undefined variable. The solid blue and brown circles indicate the positions of the ideal amorphous and crystalline phases, respectively; the

lines indicate the coexist of both amorphous and crystalline structures in real solids. Reproduced from ref. 331 with permission from Multidisciplinary Digital Publishing Institute, copyright 2011.

Though rapid progress has been made towards the implementation of crystalline semiconductor-based materials for photoconversion applications, much less effort has been focused on amorphous semiconductors. Research and development of amorphous semiconductor-based materials is expected to evolve rapidly and these materials are expected to be beneficial and highly competitive for use in solar cells, photoelectrocatalysis, and photocatalysis.

Acknowledgments: This work is supported by by the AFOSR (FA9550-19-1-0317), the NSF (CMMI 1914713, CBET 1803495, and ECCS 1914562) and the Natural Science Foundation of Jiangsu Province in China (BK20201202).

References

1. J. Barbe, M. L. Tietze, M. Neophytou, B. Murali, E. Alarousu, A. El Labban, M. Abulikemu, W. Yue, O. F. Mohammed, I. McCulloch, A. Amassian and S. Del Gobbo, *Acs Appl Mater Inter*, 2017, **9**, 11828-11836.
2. M. A. Vargas and J. E. Rodriguez-Paez, *J Non-Cryst Solids*, 2017, **459**, 192-205.
3. S. Hu, M. R. Shaner, J. A. Beardslee, M. Lichterman, B. S. Brunschwig and N. S. Lewis, *Science*, 2014, **344**, 1005-1009.
4. C. G. Morales-Guio, S. D. Tilley, H. Vrubel, M. Gratzel and X. L. Hu, *Nat Commun*, 2014, **5**, 3059.
5. R. D. L. Smith, M. S. Prevot, R. D. Fagan, Z. P. Zhang, P. A. Sedach, M. K. J. Siu, S. Trudel and C. P. Berlinguette, *Science*, 2013, **340**, 60-63.

6. B. Wang, M. Zhang, X. Cui, Z. W. Wang, M. Rager, Y. K. Yang, Z. G. Zou, Z. L. Wang and Z. Q. Lin, *Angew Chem Int Edit*, 2020, **59**, 1611-1618.
7. S. Y. Guo, S. Han, B. Chi, J. Pu and J. Li, *Acs Appl Mater Inter*, 2014, **6**, 4743-4751.
8. K. Kaur and C. V. Singh, *Enrgy Proced*, 2012, **29**, 291-299.
9. M. Ponce-Mosso, M. Perez-Gonzalez, P. E. Garcia-Tinoco, H. Crotte-Ledesma, M. Morales-Luna and S. A. Tomas, *Catal Today*, 2020, **349**, 150-158.
10. A. Mezzetti, F. Fumagalli, A. Alfano, D. Iadicicco, M. R. Antognazza and F. di Fonzo, *Faraday Discuss*, 2017, **198**, 433-448.
11. E. Verlage, S. Hu, R. Liu, R. J. R. Jones, K. Sun, C. X. Xiang, N. S. Lewis and H. A. Atwater, *Energ Environ Sci*, 2015, **8**, 3166-3172.
12. J. Gu, Y. Yan, J. L. Young, K. X. Steirer, N. R. Neale and J. A. Turner, *Nat Mater*, 2016, **15**, 456-460.
13. Y. Duan, Z. Y. Yu, S. J. Hu, X. S. Zheng, C. T. Zhang, H. H. Ding, B. C. Hu, Q. Q. Fu, Z. L. Yu, X. Zheng, J. F. Zhu, M. R. Gao and S. H. Yu, *Angew Chem Int Edit*, 2019, **58**, 15772-15777.
14. A. A. Ismail and D. W. Bahnemann, *J Mater Chem*, 2011, **21**, 11686-11707.
15. S. Wang, *Corrosion Resistance and Electrocatalytic Properties of Metallic Glasses*, IntechOpen, 2016.
16. J. F. Wager, *Aip Adv*, 2017, **7**.
17. D. Adler, *J Chem Educ*, 1980, **57**, 560-564.
18. S. Hu, M. H. Richter, M. F. Lichterman, J. Beardslee, T. Mayer, B. S. Brunschwig and N. S. Lewis, *J Phys Chem C*, 2016, **120**, 3117-3129.
19. Y. W. Chen, J. D. Prange, S. Duhnen, Y. Park, M. Gunji, C. E. D. Chidsey and P. C. McIntyre, *Nat Mater*, 2011, **10**, 539-544.
20. C. Di Valentin, G. Pacchioni and A. Selloni, *J Phys Chem C*, 2009, **113**, 20543-20552.
21. Z. W. Ren, J. Wang, Z. X. Pan, K. Zhao, H. Zhang, Y. Li, Y. X. Zhao, I. Mora-Sero, J. Bisquert and X. H. Zhong, *Chem Mater*, 2015, **27**, 8398-8405.
22. M. J. Torralvo, J. Sanz, I. Sobrados, J. Soria, C. Garlisi, G. Palmisano, S. Cetinkaya, S. Yurdakal and V. Augugliaro, *Appl Catal B-Environ*, 2018, **221**, 140-151.
23. M. R. Shaner, S. Hu, K. Sun and N. S. Lewis, *Energ Environ Sci*, 2015, **8**, 203-207.
24. K. Tanaka, M. F. V. Capule and T. Hisanaga, *Chem Phys Lett*, 1991, **187**, 73-76.
25. Z. Wang, C. Y. Yang, T. Q. Lin, H. Yin, P. Chen, D. Y. Wan, F. F. Xu, F. Q. Huang, J. H. Lin, X. M. Xie and M. H. Jiang, *Energ Environ Sci*, 2013, **6**, 3007-3014.
26. G. H. Yin, X. Y. Huang, T. Y. Chen, W. Zhao, Q. Y. Bi, J. Xu, Y. F. Han and F. Q. Huang, *Acs Catal*, 2018, **8**, 1009-1017.
27. S. Sallis, K. T. Butler, N. F. Quackenbush, D. S. Williams, M. Junda, D. A. Fischer, J. C. Woicik, N. J. Podraza, B. E. White, A. Walsh and L. F. J. Piper, *Appl Phys Lett*, 2014, **104**.
28. R. Atta-Fynn, P. Biswas and D. A. Drabold, *Phys Rev B*, 2004, **69**, 245204.
29. K. Prasai, P. Biswas and D. A. Drabold, *Semicond Sci Tech*, 2016, **31**, 073002.
30. J. Li and D. A. Drabold, *Phys Rev B*, 2003, **68**, 033103.
31. M. Jorgensen, K. Norrman and F. C. Krebs, *Sol Energ Mat Sol C*, 2008, **92**, 686-714.

32. R. W. Johnson, A. Hultqvist and S. F. Bent, *Mater Today*, 2014, **17**, 236-246.
33. Y. C. Zhang, C. Guerra-Nunez, I. Utke, J. Michler, P. Agrawal, M. D. Rossell and R. Erni, *Chem Mater*, 2017, **29**, 2232-2238.
34. E. Verlage, S. Hu, R. Liu, R. J. R. Jones, K. Sun, C. X. Xiang, N. S. Lewis and H. A. Atwater, *Energ Environ Sci*, 2015, **8**, 3166-3172.
35. M. F. Lichterman, A. I. Carim, M. T. McDowell, S. Hu, H. B. Gray, B. S. Brunschwig and N. S. Lewis, *Energ Environ Sci*, 2014, **7**, 3334-3337.
36. I. S. Kim, R. T. Haasch, D. H. Cao, O. K. Farha, J. T. Hupp, M. G. Kanatzidis and A. B. F. Martinson, *Acs Appl Mater Inter*, 2016, **8**, 24310-24314.
37. W. S. Lau, J. Zhang, X. Wan, J. K. Luo, Y. Xu and H. Wong, *Aip Adv*, 2014, **4**, 027120.
38. N. A. Al-Ahmadi, *Heliyon*, 2020, **6**.
39. J. P. C. Baena, L. Steier, W. Tress, M. Saliba, S. Neutzner, T. Matsui, F. Giordano, T. J. Jacobsson, A. R. S. Kandada, S. M. Zakeeruddin, A. Petrozza, A. Abate, M. K. Nazeeruddin, M. Gratzel and A. Hagfeldt, *Energ Environ Sci*, 2015, **8**, 2928-2934.
40. D. M. Hausmann and R. G. Gordon, *J Cryst Growth*, 2003, **249**, 251-261.
41. H. Frankenstein, C. Z. Leng, M. D. Losego and G. L. Frey, *Organic Electronics*, 2019, **64**, 37-46.
42. T. Moehl, J. Suh, L. Severy, R. Wick-Joliat and S. D. Tilley, *Acs Appl Mater Inter*, 2017, **9**, 43614-43622.
43. P. O. Oviroh, R. Akbarzadeh, D. Q. Pan, R. A. M. Coetzee and T. C. Jen, *Sci Technol Adv Mat*, 2019, **20**, 465-496.
44. D. Munoz-Rojas and J. MacManus-Driscoll, *Mater Horiz*, 2014, **1**, 314-320.
45. J. H. Liang, N. Wang, Q. X. Zhang, B. F. Liu, X. B. Kong, C. C. Wei, D. K. Zhang, B. J. Yan, Y. Zhao and X. D. Zhang, *Nano Energy*, 2017, **42**, 151-156.
46. P. L. Qin, G. J. Fang, N. H. Sun, X. Fan, Q. Zheng, F. Chen, J. W. Wan and X. Z. Zhao, *Thin Solid Films*, 2011, **519**, 4334-4341.
47. T. Harata, M. Aono, N. Kitazawa and Y. Watanabe, *Appl Phys Lett*, 2014, **105**, 051905.
48. T. Harata, M. Aono, H. Kishimura, N. Kitazawa and Y. Watanabe, *E-J Surf Sci Nanotec*, 2015, **13**, 352-356.
49. C. Iwasaki, M. Aono, N. Tamura, N. Kitazawa and Y. Watanabe, *Jpn J Appl Phys*, 2012, **51**, 10NE26.
50. C. Hom-On, M. Horprathum, P. Eiamchai, S. Limwichean, V. Patthanasettakul, N. Nuntawong, C. Chananonnawathorn, T. Lertvanithphol, N. Triroj and P. Jaroenapibal, *Mater Today-Proc*, 2018, **5**, 15228-15232.
51. K. Zakrzewska, K. Kollbek, M. Sikora, C. Kapusta, J. Szlachetko, M. Sitarz, M. Ziabka and M. Radecka, *Int J Hydrogen Energ*, 2015, **40**, 815-824.
52. D. Eisenberg, H. S. Ahn and A. J. Bard, *J Am Chem Soc*, 2014, **136**, 14011-14014.
53. J. Kim, B. K. Kim, S. K. Cho and A. J. Bard, *J Am Chem Soc*, 2014, **136**, 8173-8176.
54. S. Kawai, R. Yamazaki, S. Sobue, E. Okuno and M. Ichimura, *Apl Mater*, 2014, **2**, 032110.
55. J. R. de Andrade, I. Cesarino, R. Zhang, J. Kanicki and A. Pawlicka, *Mol Cryst Liq Cryst*, 2014, **604**, 71-83.

56. P. M. S. Monk, *Crit Rev Solid State*, 1999, **24**, 193-226.
57. D. DeMeo, S. MacNaughton, S. Sonkusale and T. E. Vandervelde, *Nanowires-Implementations and Applications*, 2011, DOI: Book_Doi 10.5772/1025, 141-156.
58. P. Jackson, D. Hariskos, R. Wuerz, O. Kiowski, A. Bauer, T. M. Friedlmeier and M. Powalla, *Phys Status Solidi-R*, 2015, **9**, 28-31.
59. D. H. Shin, S. T. Kim, J. H. Kim, H. J. Kang, B. T. Ahn and H. Kwon, *Acs Appl Mater Inter*, 2013, **5**, 12921-12927.
60. W. N. Mu and S. Z. Shi, *Polym Polym Compos*, 2014, **22**, 699-704.
61. P. Roy and S. K. Srivastava, *Thin Solid Films*, 2006, **496**, 293-298.
62. A. Y. Jaber, S. N. Alamri and M. S. Aida, *Thin Solid Films*, 2012, **520**, 3485-3489.
63. M. Ouafi, B. Jaber, L. Atourki, N. Zayyoun, A. Ihlal, A. Mzerd and L. Laanab, *Int J Photoenergy*, 2018, 4549154.
64. K. L. Choy, *Prog Mater Sci*, 2003, **48**, 57-170.
65. D. B. Li, L. Hu, Y. Xie, G. D. Niu, T. F. Liu, Y. H. Zhou, L. Gao, B. Yang and J. Tang, *Acs Photonics*, 2016, **3**, 2122-2128.
66. S. Han, W. S. Shin, M. Seo, D. Gupta, S. J. Moon and S. Yoo, *Org Electron*, 2009, **10**, 791-797.
67. S. C. Jung, B. H. Kim, S. J. Kim, N. Imaishi and Y. I. Cho, *Chem Vapor Depos*, 2005, **11**, 137-141.
68. K. L. Ou, D. Tadytin, K. X. Steirer, D. Placencia, M. Nguyen, P. Lee and N. R. Armstrong, *J Mater Chem A*, 2013, **1**, 6794-6803.
69. H. K. Ha, M. Yoshimoto, H. Koinuma, B. K. Moon and H. Ishiwara, *Appl Phys Lett*, 1996, **68**, 2965-2967.
70. S. S. Pan, X. L. Liu, M. Guo, S. F. Yu, H. T. Huang, H. T. Fan and G. H. Li, *J Mater Chem A*, 2015, **3**, 11437-11443.
71. W. Zhou, W. Li, J. Q. Wang, Y. Qu, Y. Yang, Y. Xie, K. F. Zhang, L. Wang, H. G. Fu and D. Y. Zhao, *J Am Chem Soc*, 2014, **136**, 9280-9283.
72. H. G. Yang, C. H. Sun, S. Z. Qiao, J. Zou, G. Liu, S. C. Smith, H. M. Cheng and G. Q. Lu, *Nature*, 2008, **453**, 638-641.
73. Y. Li, J. Zhu, Y. Huang, F. Liu, M. Lv, S. H. Chen, L. H. Hu, J. W. Tang, J. X. Yao and S. Y. Dai, *Rsc Adv*, 2015, **5**, 28424-28429.
74. Z. Wang, C. Y. Yang, T. Q. Lin, H. Yin, P. Chen, D. Y. Wan, F. F. Xu, F. Q. Huang, J. H. Lin, X. M. Xie and M. H. Jiang, *Adv Funct Mater*, 2013, **23**, 5444-5450.
75. X. B. Chen, L. Liu, P. Y. Yu and S. S. Mao, *Science*, 2011, **331**, 746-750.
76. Y. Yan, B. Hao, D. Wang, G. Chen, E. Markweg, A. Albrecht and P. Schaaf, *J Mater Chem A*, 2013, **1**, 14507-14513.
77. Q. Kang, J. Y. Cao, Y. J. Zhang, L. Q. Liu, H. Xu and J. H. Ye, *J Mater Chem A*, 2013, **1**, 5766-5774.
78. S. Tominaka, Y. Tsujimoto, Y. Matsushita and K. Yamaura, *Angew Chem Int Edit*, 2011, **50**, 7418-7421.
79. Z. Zhao, H. Q. Tan, H. F. Zhao, Y. Lv, L. J. Zhou, Y. J. Song and Z. C. Sun, *Chem Commun*, 2014, **50**, 2755-2757.

80. L. X. Zheng, H. Cheng, F. X. Liang, S. W. Shu, C. K. Tsang, H. Li, S. T. Lee and Y. Y. Li, *J Phys Chem C*, 2012, **116**, 5509-5515.
81. L. R. Grabstanowicz, S. M. Gao, T. Li, R. M. Rickard, T. Rajh, D. J. Liu and T. Xu, *Inorg Chem*, 2013, **52**, 3884-3890.
82. B. Bharti, S. Kumar, H. N. Lee and R. Kumar, *Sci Rep-Uk*, 2016, **6**, 32355.
83. P. L. Burn and P. Meredith, *Npg Asia Mater*, 2014, **6**, e79
84. W. Q. Wu, D. H. Chen, F. Z. Huang, Y. B. Cheng and R. A. Caruso, *J Power Sources*, 2016, **329**, 17-22.
85. K. Wang, Y. T. Shi, Q. S. Dong, Y. Li, S. F. Wang, X. F. Yu, M. Y. Wu and T. L. Ma, *J Phys Chem Lett*, 2015, **6**, 755-759.
86. A. Kogo, Y. Sanehira, Y. Numata, M. Ikegami and T. Miyasaka, *Acs Appl Mater Inter*, 2018, **10**, 2224-2229.
87. Y. Numata, R. Ishikawa, Y. Sanehira, A. Kogo, H. Shirai and T. Miyasaka, *J Mater Chem A*, 2018, **6**, 9583-9591.
88. N. Vaenas, D. Konios, T. Stergiopoulos and E. Kymakis, *Rsc Adv*, 2015, **5**, 107771-107776.
89. C. Chen, Y. Jiang, Y. H. Wu, J. L. Guo, X. Y. Kong, X. Y. Wu, Y. Z. Li, D. F. Zheng, S. J. Wu, X. S. Gao, Z. P. Hou, G. F. Zhou, Y. W. Chen, J. M. Liu, K. Kempa and J. W. Gao, *Sol Rrl*, 2020, **4**.
90. K. Wang, Y. T. Shi, B. Li, L. Zhao, W. Wang, X. Y. Wang, X. G. Bai, S. F. Wang, C. Hao and T. L. Ma, *Adv Mater*, 2016, **28**, 1891-1897.
91. V. O. Eze, Y. Seike and T. Mori, *Organic Electronics*, 2017, **46**, 253-262.
92. M. M. Tavakoli, P. Yadav, R. Tavakoli and J. Kong, *Adv Energy Mater*, 2018, **8**.
93. P. Pinpithak, H. W. Chen, A. Kulkarni, Y. Sanehira, M. Ikegami and T. Miyasaka, *Chem Lett*, 2017, **46**, 382-384.
94. X. F. Ling, J. Y. Yuan, D. A. Liu, Y. J. Wang, Y. N. Zhang, S. Chen, H. H. Wu, F. Jin, F. P. Wu, G. Z. Shi, X. Tang, J. W. Zheng, S. Z. Liu, Z. K. Liu and W. L. Ma, *Acs Appl Mater Inter*, 2017, **9**, 23181-23188.
95. C. Y. Zhang, Y. T. Shi, S. Wang, Q. S. Dong, Y. L. Feng, L. D. Wang, K. Wang, Y. Y. Shao, Y. Liu and S. F. Wang, *J Mater Chem A*, 2018, **6**, 17882-17888.
96. Z. G. Rao, B. K. Du, C. Huang, L. L. Shu, P. Lin, N. Q. Fu and S. M. Ke, *J Alloy Compd*, 2019, **789**, 276-281.
97. K. Jung, J. Lee, C. Im, J. Do, J. Kim, W. S. Chae and M. J. Lee, *Acs Energy Lett*, 2018, **3**, 2410-2417.
98. W. Q. Wu, J. F. Liao, J. X. Zhong, Y. F. Xu, L. Z. Wang and J. S. Huang, *Angew Chem Int Edit*, 2020, DOI: 10.1002/anie.202005680.
99. Q. L. Jiang, X. Sheng, Y. X. Li, X. J. Feng and T. Xu, *Chem Commun*, 2014, **50**, 14720-14723.
100. M. Gillet, K. Aguir, C. Lemire, E. Gillet and K. Schierbaum, *Thin Solid Films*, 2004, **467**, 239-246.
101. K. Mahmood, B. S. Swain, A. R. Kirmani and A. Amassian, *J Mater Chem A*, 2015, **3**, 9051-9057.

102. C. M. Chen, Z. K. Lin, W. J. Huang and S. H. Yang, *Nanoscale Res Lett*, 2016, **11**, 464-475.
103. W. J. Ke, D. W. Zhao, C. R. Grice, A. J. Cimaroli, J. Ge, H. Tao, H. W. Lei, G. J. Fang and Y. F. Yan, *J Mater Chem A*, 2015, **3**, 17971-17976.
104. Y. H. Shao, Z. G. Xiao, C. Bi, Y. B. Yuan and J. S. Huang, *Nat Commun*, 2014, **5**, 5784.
105. J. Xu, A. Buin, A. H. Ip, W. Li, O. Voznyy, R. Comin, M. J. Yuan, S. Jeon, Z. J. Ning, J. J. McDowell, P. Kanjanaboos, J. P. Sun, X. Z. Lan, L. N. Quan, D. H. Kim, I. G. Hill, P. Maksymovych and E. H. Sargent, *Nat Commun*, 2015, **6**, 7081.
106. K. Wojciechowski, S. D. Stranks, A. Abate, G. Sadoughi, A. Sadhanala, N. Kopidakis, G. Rumbles, C. Z. Li, R. H. Friend, A. K. Y. Jen and H. J. Snaith, *Acs Nano*, 2014, **8**, 12701-12709.
107. W. R. Zhou, J. M. Zhen, Q. Liu, Z. M. Fang, D. Li, P. C. Zhou, T. Chen and S. F. Yang, *J Mater Chem A*, 2017, **5**, 1724-1733.
108. W. J. Ke, G. J. Fang, Q. Liu, L. B. Xiong, P. L. Qin, H. Tao, J. Wang, H. W. Lei, B. R. Li, J. W. Wan, G. Yang and Y. F. Yan, *J Am Chem Soc*, 2015, **137**, 6730-6733.
109. J. X. Song, E. Q. Zheng, J. Bian, X. F. Wang, W. J. Tian, Y. Sanehira and T. Miyasaka, *J Mater Chem A*, 2015, **3**, 10837-10844.
110. Q. Jiang, L. Q. Zhang, H. L. Wang, X. L. Yang, J. H. Meng, H. Liu, Z. G. Yin, J. L. Wu, X. W. Zhang and J. B. You, *Nat Energy*, 2017, **2**, 1-7.
111. W. Hui, Y. G. Yang, Q. Xu, H. Gu, S. L. Feng, Z. H. Su, M. R. Zhang, J. O. Wang, X. D. Li, J. F. Fang, F. Xia, Y. D. Xia, Y. H. Chen, X. Y. Gao and W. Huang, *Adv Mater*, 2020, **32**.
112. L. B. Xiong, Y. X. Guo, J. Wen, H. R. Liu, G. Yang, P. L. Qin and G. J. Fang, *Adv Funct Mater*, 2018, **28**, 1802757.
113. Q. S. Dong, Y. T. Shi, K. Wang, Y. Li, S. F. Wang, H. Zhang, Y. J. Xing, Y. Du, X. G. Bai and T. L. Ma, *J Phys Chem C*, 2015, **119**, 10212-10217.
114. W. J. Ke, D. W. Zhao, A. J. Cimaroli, C. R. Grice, P. L. Qin, Q. Liu, L. B. Xiong, Y. F. Yan and G. J. Fang, *J Mater Chem A*, 2015, **3**, 24163-24168.
115. L. Cojocaru, S. Uchida, P. V. V. Jayaweera, S. Kaneko, J. Nakazaki, T. Kubo and H. Segawa, *Chem Lett*, 2015, **44**, 1750-1752.
116. M. Park, J. Y. Kim, H. J. Son, C. H. Lee, S. S. Jang and M. J. Ko, *Nano Energy*, 2016, **26**, 208-215.
117. M. De Bastiani, G. Dell'Erba, M. Gandini, V. D'Innocenzo, S. Neutzner, A. R. S. Kandada, G. Grancini, M. Binda, M. Prato, J. M. Ball, M. Caironi and A. Petrozza, *Adv Energy Mater*, 2016, **6**, 1501453.
118. D. Yang, R. X. Yang, K. Wang, C. C. Wu, X. J. Zhu, J. S. Feng, X. D. Ren, G. J. Fang, S. Priya and S. Z. Liu, *Nat Commun*, 2018, **9**, 3239.
119. H. B. Song, X. J. Zhan, D. B. Li, Y. Zhou, B. Yang, K. Zeng, J. Zhong, X. S. Miao and J. Tang, *Sol Energ Mat Sol C*, 2016, **146**, 1-7.
120. B. X. Chen, C. Uher, L. Iordanidis and M. G. Kanatzidis, *Chem Mater*, 1997, **9**, 1655-1658.

121. A. L. Roest, J. J. Kelly, D. Vanmaekelbergh and E. A. Meulenkamp, *Phys Rev Lett*, 2002, **89**, 036801
122. Y. Zhou, L. Wang, S. Y. Chen, S. K. Qin, X. S. Liu, J. Chen, D. J. Xue, M. Luo, Y. Z. Cao, Y. B. Cheng, E. H. Sargent and J. Tang, *Nat Photonics*, 2015, **9**, 409-415.
123. T. Minemoto, T. Matsui, H. Takakura, Y. Hamakawa, T. Negami, Y. Hashimoto, T. Uenoyama and M. Kitagawa, *Sol Energ Mat Sol C*, 2001, **67**, 83-88.
124. Lattante，S., *Electronics*, 2014, **3**, 132-164.
125. D. J. Bindl, M. Y. Wu, F. C. Prehn and M. S. Arnold, *Nano Lett*, 2011, **11**, 455-460.
126. M. Notarianni, K. Vernon, A. Chou, M. Aljada, J. Z. Liu and N. Motta, *Sol Energy*, 2014, **106**, 23-37.
127. Q. F. Zhang, S. Yodyingyong, J. T. Xi, D. Myers and G. Z. Cao, *Nanoscale*, 2012, **4**, 1436-1445.
128. S. K. Hau, H. L. Yip and A. K. Y. Jen, *Polym Rev*, 2010, **50**, 474-510.
129. J. Kalowekamo and E. Baker, *Sol Energy*, 2009, **83**, 1224-1231.
130. O. A. Abdulrazzaq, V. Saini, S. Bourdo, E. Dervishi and A. S. Biris, *Particul Sci Technol*, 2013, **31**, 427-442.
131. G. E. Morse, A. Tournebize, A. Rivaton, T. Chasse, C. Taviot-Gueho, N. Blouin, O. R. Lozman and S. Tierney, *Phys Chem Chem Phys*, 2015, **17**, 11884-11897.
132. J. Kesters, P. Verstappen, J. Raymakers, W. Vanormelingen, J. Drijkoningen, J. D'Haen, J. Manca, L. Lutsen, D. Vanderzande and W. Maes, *Chem Mater*, 2015, **27**, 1332-1341.
133. M. P. de Jong, L. J. van IJzendoorn and M. J. A. de Voigt, *Appl Phys Lett*, 2000, **77**, 2255-2257.
134. H. K. Kim, K. S. Lee and J. H. Kwon, *Appl Phys Lett*, 2006, **88**.
135. Y. Y. Choi, C. K. H., L. H., Lee H., Kang J. W. and K. H. K., *Sol. Energy Mater. Sol. Cells*, 2011, **95**, 1615.
136. C. K. H., J. J. A. and K. H. K., *Sol. Energy Mater. Sol. Cells*, 2010, **94**, 1822-1830.
137. H. M. Lee, S. B. Kang, K. B. Chung and H. K. Kim, *Appl Phys Lett*, 2013, **102**, 021914.
138. N. J. Zhou, D. B. Buchholz, G. Zhu, X. G. Yu, H. Lin, A. Facchetti, T. J. Marks and R. P. H. Chang, *Adv Mater*, 2014, **26**, 1098-1104.
139. J. Liu, D. B. Buchholz, R. P. H. Chang, A. Facchetti and T. J. Marks, *Adv Mater*, 2010, **22**, 2333-2337.
140. D. Y. Cho, K. H. Kim, T. W. Kim, Y. J. Noh, S. I. Na, K. B. Chung and H. K. Kim, *Organic Electronics*, 2015, **24**, 227-233.
141. Y. Y. Choi, K. H. Choi, H. Lee, H. Lee, J. W. Kang and H. K. Kim, *Sol Energ Mat Sol C*, 2011, **95**, 1615-1623.
142. B. R. Lee, J. S. Goo, Y. W. Kim, Y. J. You, H. Kim, S. K. Lee, J. W. Shim and T. G. Kim, *J Power Sources*, 2019, **417**, 61-69.
143. N. J. Zhou, M. G. Kim, S. Loser, J. Smith, H. Yoshida, X. G. Guo, C. Song, H. Jin, Z. H. Chen, S. M. Yoon, A. J. Freeman, R. P. H. Chang, A. Facchetti and T. J. Marks, *P Natl Acad Sci USA*, 2015, **112**, 7897-7902.
144. R. E. L., Z. B. and A. N. R., *J. Phys. Chem. Lett*, 2011, **2**, 1337-1450.

145. R. Steim, F. R. Kogler and C. J. Brabec, *J Mater Chem*, 2010, **20**, 2499-2512.
146. T. Kuwabara, T. Nakayama, K. Uozumi, T. Yamaguchi and K. Takahashi, *Sol Energ Mat Sol C*, 2008, **92**, 1476-1482.
147. M. Takahashi, K. Tsukigi, T. Uchino and T. Yoko, *Thin Solid Films*, 2001, **388**, 231-236.
148. K. Pomoni, A. Vomvas and C. Trapalis, *Thin Solid Films*, 2005, **479**, 160-165.
149. Z. H. Lin, C. Y. Jiang, C. X. Zhu and J. Zhang, *Acs Appl Mater Inter*, 2013, **5**, 713-718.
150. K. S. Yeo, S. Nakao, Y. Hirose, T. Hasegawa and Y. Matsuo, *Organic Electronics*, 2013, **14**, 1715-1719.
151. H. S. Yang, J. Kim, K. Yamamoto, X. Xing and H. Hosono, *Appl Surf Sci*, 2018, **434**, 995-1000.
152. H. Hosono, J. Kim, Y. Toda, T. Kamiya and S. Watanabe, *P Natl Acad Sci USA*, 2017, **114**, 233-238.
153. T. Kamiya and H. Hosono, *Npg Asia Mater*, 2010, **2**, 15-22.
154. J. D. Perkins, T. Gennett, J. E. Leisch, R. Sundaramoorthy, I. L. Repins, M. F. A. M. van Hest and D. S. Ginley, *Ieee Phot Spec Conf*, 2010, 989-991.
155. A. Walsh, J. L. F. Da Silva, Y. F. Yan, M. M. Al-Jassim and S. H. Wei, *Phys Rev B*, 2009, **79**, 073105.
156. M. Y. Chan, C. S. Lee, S. L. Lai, M. K. Fung, F. L. Wong, H. Y. Sun, K. M. Lau and S. T. Lee, *J Appl Phys*, 2006, **100**, 094506.
157. A. G. F. Janssen, T. Riedl, S. Hamwi, H. H. Johannes and W. Kowalsky, *Appl Phys Lett*, 2007, **91**, 073519.
158. C. Tao, S. P. Ruan, G. H. Xie, X. Z. Kong, L. Shen, F. X. Meng, C. X. Liu, X. D. Zhang, W. Dong and W. Y. Chen, *Appl Phys Lett*, 2009, **94**, 043311.
159. P. Hones, C. Zakri, P. E. Schmid, F. Levy and O. R. Shojaei, *Appl Phys Lett*, 2000, **76**, 3194-3196.
160. P. L. Qin, G. J. Fang, Q. He, N. H. Sun, X. Fan, Q. Zheng, F. Chen, J. W. Wan and X. Z. Zhao, *Sol Energ Mat Sol C*, 2011, **95**, 1005-1010.
161. J. Sun, C. H. Tang, J. M. Xu, X. S. Yin, S. Nie, H. Q. Wang, K. Sun, S. J. Cho and H. Gong, *Int J Hydrogen Energ*, 2015, **40**, 10194-10199.
162. N. Khongchareon, S. Choopun, N. Hongsith, A. Gardchareon, S. Phadungdhitidhada and D. Wongratanaphisan, *Electrochim Acta*, 2013, **106**, 195-200.
163. T. H. Meen, J. K. Tsai, Y. S. Tu, T. C. Wu, W. D. Hsu and S. J. Chang, *Nanoscale Res Lett*, 2014, **9**, 523.
164. M. D. Ye, X. R. Wen, M. Y. Wang, J. Iocozzia, N. Zhang, C. J. Lin and Z. Q. Lin, *Mater Today*, 2015, **18**, 155-162.
165. X. J. Feng, K. Zhu, A. J. Frank, C. A. Grimes and T. E. Mallouk, *Angew Chem Int Edit*, 2012, **51**, 2727-2730.
166. J. Wang and Z. Q. Lin, *Chem-Asian J*, 2012, **7**, 2754-2762.
167. S. Colodrero, A. Forneli, C. Lopez-Lopez, L. Pelleja, H. Miguez and E. Palomares, *Adv Funct Mater*, 2012, **22**, 1303-1310.
168. R. D. Eithiraj and K. R. Geethalakshmi, *Chem Phys Lett*, 2013, **585**, 138-142.

169. A. Walker, H. Snaith, F. D. Angelis and C. E. D., *Unconventional Thin Film Photovoltaics: RSC Energy and Environment Series*, Royal Society of Chemistry, 2016.
170. V. Johansson, L. Ellis-Gibbings, T. Clarke, M. Gorlov, G. G. Andersson and L. Kloo, *Phys Chem Chem Phys*, 2014, **16**, 711-718.
171. K. Al-Attafi, A. Nattestad, Q. J. Wu, Y. Ide, Y. Yamauchi, S. X. Dou and J. H. Kim, *Chem Commun*, 2018, **54**, 381-384.
172. N. Kakuta, T. Oku, A. Suzuki, K. Kikuchi and S. Kikuchi, *J. Cera. Pro. Rese.*, 2012, **13**.
173. D. S. Zhang, H. Y. Hu, L. F. Li and S. D. L., *Journal of Nanomaterials*, 2008, 271631.
174. S. Kurian, P. Sudhagar, J. Lee, D. Song, W. Cho, S. Lee, Y. S. Kang and H. Jeon, *J Mater Chem A*, 2013, **1**, 4370-4375.
175. N. A. Ovramenko, L. I. Shvets, F. D. Ovcharenko and B. Y. Kornilovich, *Inorg Mater+*, 1979, **15**, 1560-1562.
176. P. Pinceloup, C. Courtois, J. Vicens, A. Leriche and B. Thierry, *J Eur Ceram Soc*, 1999, **19**, 973-977.
177. T. Ohno, K. Sarukawa, K. Tokieda and M. Matsumura, *J Catal*, 2001, **203**, 82-86.
178. B. Yacoubi, L. Samet, J. Bennaceur, A. Lamouchi and R. Chtourou, *Mat Sci Semicon Proc*, 2015, **30**, 361-367.
179. J. G. Wang and D. S. Bai, *J Electrochem Soc*, 2014, **161**, H265-H268.
180. T. Oku, N. Kakuta, K. Kobayashi, A. Suzuki and K. Kikuchi, *Prog Nat Sci*, 2011, **21**, 122-126.
181. C. H. Han, H. S. Lee, K. W. Lee, S. D. Han and I. Singh, *B Korean Chem Soc*, 2009, **30**, 219-223.
182. M. A. Alpuche-Aviles and Y. Y. Wu, *J Am Chem Soc*, 2009, **131**, 3216-3224.
183. S. H. Choi, D. Hwang, D. Y. Kim, Y. Kervella, P. Maldivi, S. Y. Jang, R. Demadrille and I. D. Kim, *Adv Funct Mater*, 2013, **23**, 3146-3155.
184. S. Hisatome and M. Takemoto, *Electrochemistry*, 2016, **84**, 130-132.
185. S. N. Yun, P. D. Lund and A. Hinsch, *Energ Environ Sci*, 2015, **8**, 3495-3514.
186. F. De Rossi, L. Di Gaspare, A. Reale, A. Di Carlo and T. M. Brown, *J Mater Chem A*, 2013, **1**, 12941-12947.
187. M. K. Wang, A. M. Anghel, B. Marsan, N. L. C. Ha, N. Pootrakulchote, S. M. Zakeeruddin and M. Gratzel, *J Am Chem Soc*, 2009, **131**, 15976-15977.
188. P. Hasin, *Sol Energy*, 2016, **135**, 398-407.
189. J. H. Bae, J. M. Moon, J. W. Kang, H. D. Park, J. J. Kim, W. J. Cho and H. K. Kim, *J Electrochem Soc*, 2007, **154**, J81-J85.
190. S. S. Kim, K. W. Park, J. H. Yum and Y. E. Sung, *Sol Energ Mat Sol C*, 2006, **90**, 283-290.
191. G. H. Carey, A. L. Abdelhady, Z. J. Ning, S. M. Thon, O. M. Bakr and E. H. Sargent, *Chem Rev*, 2015, **115**, 12732-12763.
192. T. Sogabe, Q. Shen and K. Yamaguchi, *J. of Photonics for Energy*, 2016, **6**, 040910.
193. O. E. Semonin, J. M. Luther and M. C. Beard, *Mater Today*, 2012, **15**, 508-515.
194. G. Hodes, *J Phys Chem C*, 2008, **112**, 17778-17787.

195. Z. X. Pan, I. Mora-Sero, Q. Shen, H. Zhang, Y. Li, K. Zhao, J. Wang, X. H. Zhong and J. Bisquert, *J Am Chem Soc*, 2014, **136**, 9203-9210.
196. I. Mora-Sero, S. Gimenez, F. Fabregat-Santiago, R. Gomez, Q. Shen, T. Toyoda and J. Bisquert, *Accounts Chem Res*, 2009, **42**, 1848-1857.
197. L. J. Diguna, Q. Shen, J. Kobayashi and T. Toyoda, *Appl Phys Lett*, 2007, **91**, 023116.
198. M. Shalom, S. Dor, S. Ruhle, L. Grinis and A. Zaban, *J Phys Chem C*, 2009, **113**, 3895-3898.
199. E. Barea, X. Q. Xu, V. Gonzalez-Pedro, T. Ripolles-Sanchis, F. Fabregat-Santiago and J. Bisquert, *Energ Environ Sci*, 2011, **4**, 3414-3419.
200. O. Niitsoo, S. K. Sarkar, C. Pejoux, S. Ruhle, D. Cahen and G. Hodes, *J Photoch Photobio A*, 2006, **181**, 306-313.
201. Y. L. Lee, B. M. Huang and H. T. Chien, *Chem Mater*, 2008, **20**, 6903-6905.
202. M. Shalom, J. Albero, Z. Tachan, E. Martinez-Ferrero, A. Zaban and E. Palomares, *J Phys Chem Lett*, 2010, **1**, 1134-1138.
203. Z. W. Ren, J. Wang, Z. X. Pan, K. Zhao, H. Zhang, Y. Li, Y. X. Zhao, I. Mora-Sero, J. Bisquert and X. H. Zhong, *Chem Mater*, 2015, **27**, 8398-8405.
204. H. B. Yang, C. X. Guo, G. H. Guai, Q. L. Song, S. P. Jiang and C. M. Li, *Acs Appl Mater Inter*, 2011, **3**, 1940-1945.
205. L. D. Sun and Q. Wang, *Acs Appl Mater Inter*, 2014, **6**, 14239-14246.
206. A. A. Patel, F. X. Wu, J. Z. Zhang, C. L. Torres-Martinez, R. K. Mehra, Y. Yang and S. H. Risbud, *Journal of Physical Chemistry B*, 2000, **104**, 11598-11605.
207. J. Tang, K. W. Kemp, S. Hoogland, K. S. Jeong, H. Liu, L. Levina, M. Furukawa, X. H. Wang, R. Debnath, D. K. Cha, K. W. Chou, A. Fischer, A. Amassian, J. B. Asbury and E. H. Sargent, *Nat Mater*, 2011, **10**, 765-771.
208. A. H. Ip, S. M. Thon, S. Hoogland, O. Voznyy, D. Zhitomirsky, R. Debnath, L. Levina, L. R. Rollny, G. H. Carey, A. Fischer, K. W. Kemp, I. J. Kramer, Z. J. Ning, A. J. Labelle, K. W. Chou, A. Amassian and E. H. Sargent, *Nat Nanotechnol*, 2012, **7**, 577-582.
209. F. A. Roghabadi, V. Ahmadi, B. A. Nejand and K. O. Aghmiuni, *Chemsuschem*, 2017, **10**, 2352-2359.
210. J. W. Sun, D. K. Zhong and D. R. Gamelin, *Energ Environ Sci*, 2010, **3**, 1252-1261.
211. A. Paracchino, N. Mathews, T. Hisatomi, M. Stefik, S. D. Tilley and M. Gratzel, *Energ Environ Sci*, 2012, **5**, 8673-8681.
212. Y. B. Wu, M. K. Y. Chan and G. Ceder, *Phys Rev B*, 2011, **83**, 235301
213. M. G. Walter, E. L. Warren, J. R. McKone, S. W. Boettcher, Q. X. Mi, E. A. Santori and N. S. Lewis, *Chem Rev*, 2010, **110**, 6446-6473.
214. Vonkujaw.R, *Z Phys Chem-Leipzig*, 1967, **235**, 140-&.
215. Y. Nakato, T. Ohnishi and H. Tsubomura, *Chem Lett*, 1975, **4**, 883-886.
216. R. C. Kainthla, B. Zelenay and J. O. Bockris, *J Electrochem Soc*, 1987, **134**, 841-845.
217. M. T. McDowell, M. F. Lichterman, A. I. Carim, R. Liu, S. Hu, B. S. Brunschwig and N. S. Lewis, *Acs Appl Mater Inter*, 2015, **7**, 15189-15199.
218. H. H. Pham and L. W. Wang, *Phys Chem Chem Phys*, 2015, **17**, 541-550.

219. G. J. Liu, S. Ye, P. L. Yan, F. Q. Xiong, P. Fu, Z. L. Wang, Z. Chen, J. Y. Shi and C. Li, *Energ Environ Sci*, 2016, **9**, 1327-1334.
220. Z. L. Ma, T. Thersleff, A. L. Gorne, N. Cordes, Y. B. Liu, S. Jakobi, A. Rokicinska, Z. G. Schichtl, R. H. Coridan, P. Kustrowski, W. Schnick, R. Dronskowski and A. Slabon, *Acs Appl Mater Inter*, 2019, **11**, 19077-19086.
221. P. A. Kohl, S. N. Frank and A. J. Bard, *J Electrochem Soc*, 1977, **124**, 225-229.
222. A. G. Scheuermann, J. D. Prange, M. Gunji, C. E. D. Chidsey and P. C. McIntyre, *Energ Environ Sci*, 2013, **6**, 2487-2496.
223. S. Duenas, H. Castan, H. Garcia, E. San Andres, M. Toledano-Luque, I. Martil, G. Gonzalez-Diaz, K. Kukli, T. Uustare and J. Aarik, *Semicond Sci Tech*, 2005, **20**, 1044-1051.
224. L. Liu, H. L. Hou, L. Wang, R. Xu, Y. Lei, S. H. Shen, D. J. Yang and W. Y. Yang, *Nanoscale*, 2017, **9**, 15650-15657.
225. Y. H. Yu, Z. Zhang, X. Yin, A. Kvit, Q. L. Liao, Z. Kang, X. Q. Yan, Y. Zhang and X. D. Wang, *Nat Energy*, 2017, **2**, 17045.
226. M. T. McDowell, M. F. Lichterman, J. M. Spurgeon, S. Hu, I. D. Sharp, B. S. Brunschwig and N. S. Lewis, *J Phys Chem C*, 2014, **118**, 19618-19624.
227. Z. D. Guo, F. Ambrosio and A. Pasquarello, *J Mater Chem A*, 2018, **6**, 11804-11810.
228. S. S. Kalanur, I. H. Yoo, J. Park and H. Seo, *J Mater Chem A*, 2017, **5**, 1455-1461.
229. H. S. Ahn and A. J. Bard, *Angew Chem Int Edit*, 2015, **54**, 13753-13757.
230. S. Y. Guo, S. Han, H. F. Mao, S. M. Dong, C. C. Wu, L. C. Jia, B. Chi, J. Pu and J. Li, *J Power Sources*, 2014, **245**, 979-985.
231. X. B. Zhang, J. M. Yan, S. Han, H. Shioyama and Q. Xu, *J Am Chem Soc*, 2009, **131**, 2778-2779.
232. M. W. Shah, Y. Q. Zhu, X. Y. Fan, J. Zhao, Y. X. Li, S. Asim and C. Y. Wang, *Sci Rep-Uk*, 2015, **5**, 15804.
233. C. C. Wang, C. Y. Chou, S. R. Yi and H. D. Chen, *Int J Hydrogen Energ*, 2019, **44**, 28685-28697.
234. T. He, L. H. Zu, Y. Zhang, C. L. Mao, X. X. Xu, J. H. Yang and S. H. Yang, *Acs Nano*, 2016, **10**, 7882-7891.
235. G. M. Wang, H. Y. Wang, Y. C. Ling, Y. C. Tang, X. Y. Yang, R. C. Fitzmorris, C. C. Wang, J. Z. Zhang and Y. Li, *Nano Lett*, 2011, **11**, 3026-3033.
236. Y. H. Hu, *Angew Chem Int Edit*, 2012, **51**, 12410-12412.
237. W. T. Kim, C. D. Kim and Q. W. Choi, *Phys Rev B*, 1984, **30**, 3625-3628.
238. A. Naldoni, M. Allieta, S. Santangelo, M. Marelli, F. Fabbri, S. Cappelli, C. L. Bianchi, R. Psaro and V. Dal Santo, *J Am Chem Soc*, 2012, **134**, 7600-7603.
239. M. Hannula, H. Ali-Loytty, K. Lahtonen, E. Sarlin, J. Saari and M. Valden, *Chem Mater*, 2018, **30**, 1199-1208.
240. R. Liu, Z. Zheng, J. Spurgeon and X. G. Yang, *Energ Environ Sci*, 2014, **7**, 2504-2517.
241. L. X. Meng, S. Y. Wang, F. R. Cao, W. Tian, R. Long and L. Li, *Angew Chem Int Edit*, 2019, **58**, 6761-6765.
242. H. W. Zhang, L. Ma, J. T. Ming, B. Q. Liu, Y. B. Zhao, Y. D. Hou, Z. X. Ding, C. Xu,

Z. Z. Zhang and J. L. Long, *Appl Catal B-Environ*, 2019, **243**, 481-489.
243. S. Landsmann, Y. Surace, M. Trottmann, S. Dilger, A. Weidenkaff and S. Pokrant, *Acs Appl Mater Inter*, 2016, **8**, 12149-12157.
244. Y. C. Mao, Y. G. Cheng, J. Q. Wang, H. Yang, M. Y. Li, J. Chen, M. J. Chao, Y. X. Tong and E. J. Liang, *New J Chem*, 2016, **40**, 107-112.
245. B. N. Kim, G. K. Seo, S. W. Hwang, H. Yu, B. Ahn, H. Seo and I. S. Cho, *Ceram Int*, 2018, **44**, 1843-1849.
246. F. Malara, A. Minguzzi, M. Marelli, S. Morandi, R. Psaro, V. Dal Santo and A. Naldoni, *Acs Catal*, 2015, **5**, 5292-5300.
247. Q. Liu, F. R. Cao, F. L. Wu, H. Lu and L. Li, *Adv Mater Interfaces*, 2016, **3**, 1600256.
248. X. L. Guo, L. L. Wang and Y. W. Tan, *Nano Energy*, 2015, **16**, 320-328.
249. S. U. M. Khan, M. Al-Shahry and W. B. Ingler, *Science*, 2002, **297**, 2243-2245.
250. G. Lin, G. P. Dong, D. Z. Tan, X. F. Liu, Q. A. Zhang, D. P. Chen, J. R. Qiu, Q. Z. Zhao and Z. Z. Xu, *J Alloy Compd*, 2010, **504**, 177-180.
251. K. M. Haynes, C. M. Perry, M. Rivas, T. D. Golden, A. Bazan, M. Quintana, V. N. Nesterov, S. A. Berhe, J. Rodriguez, W. Estrada and W. J. Youngblood, *Acs Appl Mater Inter*, 2015, **7**, 830-837.
252. C. Das, B. Ananthoju, A. K. Dhara, M. Aslam, S. K. Sarkar and K. R. Balasubramaniam, *Adv Mater Interfaces*, 2017, **4**, 1700271.
253. A. Niilisk, M. Moppel, M. Pars, I. Sildos, T. Jantson, T. Avarmaa, R. Jaaniso and J. Aarik, *Cent Eur J Phys*, 2006, **4**, 105-116.
254. Y. H. Lai, D. W. Palm and E. Reisner, *Adv Energy Mater*, 2015, **5**, 1501668.
255. S. Y. Lien, D. S. Wuu, W. C. Yeh and J. C. Liu, *Sol Energ Mat Sol C*, 2006, **90**, 2710-2719.
256. A. Heller, *Science*, 1984, **223**, 1141-1148.
257. J. Gu, J. A. Aguiar, S. Ferrere, K. X. Steirer, Y. Yan, C. X. Xiao, J. L. Young, M. Al-Jassim, N. R. Neale and J. A. Turner, *Nat Energy*, 2017, **2**, 16192.
258. L. D. Burke and M. B. C. Roche, *J Electroanal Chem*, 1984, **164**, 315-334.
259. H. Y. Shen, X. X. Zhou, W. Dong, X. D. Su, L. Fang, X. Wu and M. R. Shen, *Appl Phys Lett*, 2017, **111**, 123901.
260. B. Seger, T. Pedersen, A. B. Laursen, P. C. K. Vesborg, O. Hansen and I. Chorkendorff, *J Am Chem Soc*, 2013, **135**, 1057-1064.
261. M. Zhang, C. X. Jiang, W. Dong, F. G. Zheng, L. Fang, X. D. Su and M. R. Shen, *Appl Phys Lett*, 2013, **103**, 102902.
262. D. Prasai, J. C. Tuberquia, R. R. Harl, G. K. Jennings and K. I. Bolotin, *Acs Nano*, 2012, **6**, 1102-1108.
263. M. J. Nine, M. A. Cole, D. N. H. Tran and D. Losic, *J Mater Chem A*, 2015, **3**, 12580-12602.
264. J. Y. Zheng, Y. H. Lyu, R. L. Wang, C. Xie, H. J. Zhou, S. P. Jiang and S. Y. Wang, *Nat Commun*, 2018, **9**, 3572.
265. Z. Wang, C. Y. Yang, T. Q. Lin, H. Yin, P. Chen, D. Y. Wan, F. F. Xu, F. Q. Huang, J. H. Lin, X. M. Xie and M. H. Jiang, *Adv Funct Mater*, 2013, **23**, 5444-5450.

266. D. Merki, S. Fierro, H. Vrubel and X. L. Hu, *Chem Sci*, 2011, **2**, 1262-1267.
267. H. Vrubel and X. L. Hu, *Acs Catal*, 2013, **3**, 2002-2011.
268. H. G. Yu, P. A. Xiao, P. Wang and J. G. Yu, *Appl Catal B-Environ*, 2016, **193**, 217-225.
269. B. Hinnemann, P. G. Moses, J. Bonde, K. P. Jorgensen, J. H. Nielsen, S. Horch, I. Chorkendorff and J. K. Norskov, *J Am Chem Soc*, 2005, **127**, 5308-5309.
270. A. Paracchino, V. Laporte, K. Sivula, M. Gratzel and E. Thimsen, *Nat Mater*, 2011, **10**, 456-461.
271. S. D. Tilley, M. Schreier, J. Azevedo, M. Stefik and M. Graetzel, *Adv Funct Mater*, 2014, **24**, 303-311.
272. H. Vrubel, D. Merki and X. L. Hu, *Energ Environ Sci*, 2012, **5**, 6136-6144.
273. Y. F. Huang, R. J. Nielsen, W. A. Goddard and M. P. Soriaga, *J Am Chem Soc*, 2015, **137**, 6692-6698.
274. P. D. Tran, T. V. Tran, M. Orio, S. Torelli, Q. D. Truong, K. Nayuki, Y. Sasaki, S. Y. Chiam, R. Yi, I. Honma, J. Barber and V. Artero, *Nat Mater*, 2016, **15**, 640-646.
275. T. F. Jaramillo, K. P. Jorgensen, J. Bonde, J. H. Nielsen, S. Horch and I. Chorkendorff, *Science*, 2007, **317**, 100-102.
276. T. W. Lin, C. J. Liu and J. Y. Lin, *Appl Catal B-Environ*, 2013, **134**, 75-82.
277. Q. Ding, B. Song, P. Xu and S. Jin, *Chem-Us*, 2016, **1**, 699-726.
278. J. Kibsgaard, T. F. Jaramillo and F. Besenbacher, *Nat Chem*, 2014, **6**, 248-253.
279. J. Tan, W. Yang, Y. Oh, H. Lee, J. Park and J. Moon, *Acs Appl Mater Inter*, 2018, **10**, 10898-10908.
280. F. Fumagalli, S. Bellani, M. Schreier, S. Leonardi, H. C. Rojas, A. Ghadirzadeh, G. Tullii, A. Savoini, G. Marra, L. Meda, M. Gratzel, G. Lanzani, M. T. Mayer, M. R. Antognazza and F. Di Fonzo, *J Mater Chem A*, 2016, **4**, 2178-2187.
281. T. Bourgeteau, D. Tondelier, B. Geffroy, R. Brisse, C. Laberty-Robert, S. Campidelli, R. de Bettignies, V. Artero, S. Palacin and B. Jousselme, *Energ Environ Sci*, 2013, **6**, 2706-2713.
282. M. T. Greiner, M. G. Helander, W. M. Tang, Z. B. Wang, J. Qiu and Z. H. Lu, *Nat Mater*, 2012, **11**, 76-81.
283. M. Vasilopoulou, L. C. Palilis, D. G. Georgiadou, A. M. Douvas, P. Argitis, S. Kennou, L. Sygellou, G. Papadimitropoulos, I. Kostis, N. A. Stathopoulos and D. Davazoglou, *Adv Funct Mater*, 2011, **21**, 1489-1497.
284. J. Zhao, E. Olide and F. E. Osterloh, *J Electrochem Soc*, 2015, **162**, H65-H71.
285. S. J. Calero, P. Ortiz, A. F. Onate and M. T. Cortes, *Int J Hydrogen Energ*, 2016, **41**, 4922-4930.
286. W. G. Xie, M. Z. Su, Z. B. Zheng, Y. Wang, L. Gong, F. Y. Xie, W. H. Zhang, Z. Luo, J. Y. Luo, P. Y. Liu, N. S. Xu, S. Z. Deng, H. J. Chen and J. Chen, *Acs Nano*, 2016, **10**, 1662-1670.
287. M. F. Saenger, T. Hoing, B. W. Robertson, R. B. Billa, T. Hofmann, E. Schubert and M. Schubert, *Phys Rev B*, 2008, **78**, 245205.
288. R. Giannuzzi, M. Balandeh, A. Mezzetti, L. Meda, P. Pattathil, G. Gigli, F. Di Fonzo

and M. Manca, *Adv Opt Mater*, 2015, **3**, 1614-1622.
289. J. Highfield, *Molecules*, 2015, **20**, 6739-6793.
290. M. A. Rahman, J. P. Thomas and K. T. Leung, *Adv Energy Mater*, 2018, **8**, 1701234.
291. H. W. Yeon, S. M. Lim, J. K. Jung, H. Yoo, Y. J. Lee, H. Y. Kang, Y. J. Park, M. Kim and Y. C. Joo, *Npg Asia Mater*, 2016, **8**, e250.
292. Y. P. Dan, K. Seo, K. Takei, J. H. Meza, A. Javey and K. B. Crozier, *Nano Lett*, 2011, **11**, 2527-2532.
293. M. J. Kang and Y. S. Kang, *J Mater Chem A*, 2015, **3**, 15723-15728.
294. V. A. Lebedev, D. A. Kozlov, I. V. Kolesnik, A. S. Poluboyarinov, A. E. Becerikli, W. Grunert and A. V. Garshev, *Appl Catal B-Environ*, 2016, **195**, 39-47.
295. Z. W. Yang, B. Wang, H. Cui, H. An, Y. Pan and J. P. Zhai, *J Phys Chem C*, 2015, **119**, 16905-16912.
296. Z. W. Yang, B. Wang, J. Zhang, H. Cui, Y. Pan, H. An and J. P. Zhai, *Phys Chem Chem Phys*, 2015, **17**, 18670-18676.
297. B. Wang, Z. W. Yang, H. An, J. P. Zhai, Q. Li and H. Cui, *Appl Surf Sci*, 2015, **324**, 817-824.
298. B. Wang, C. Li, H. Cui, J. Zhang, J. P. Zhai and Q. Li, *J Mater Sci*, 2014, **49**, 1336-1344.
299. S. Manzhos, G. Giorgi and K. Yamashita, *Molecules*, 2015, **20**, 3371-3388.
300. Y. Kim, H. M. Hwang, L. Wang, I. Kim, Y. Yoon and H. Lee, *Sci Rep-Uk*, 2016, **6**, 25212.
301. L. Hao, S. Q. Tang, J. C. Yan, L. J. Cheng, S. J. Guan, Q. Zhao, Z. Zhu and Y. Lu, *Mat Sci Semicon Proc*, 2019, **89**, 161-169.
302. J. Soria, J. Sanz, M. J. Torralvo, I. Sobrados, C. Garlisi, G. Palmisano, S. Cetinkaya, S. Yurdakal and V. Augugliaro, *Appl Catal B-Environ*, 2017, **210**, 306-319.
303. G. Xiong, Q. Y. Jia, Y. Y. Cao, L. P. Liu and Z. D. Guo, *Rsc Adv*, 2017, **7**, 24046-24054.
304. S. Abedi and A. Morsali, *Acs Catal*, 2014, **4**, 1398-1403.
305. S. Abedi, B. Karimi, F. Kazemi, M. Bostina and H. Vali, *Org Biomol Chem*, 2013, **11**, 416-419.
306. E. V. Chulkov, A. G. Borisov, J. P. Gauyacq, D. Sanchez-Portal, V. M. Silkin, V. P. Zhukov and P. M. Echenique, *Chem Rev*, 2006, **106**, 4160-4206.
307. V. Sharma, S. Kumar and V. Krishnan, *Mater Chem Phys*, 2016, **179**, 129-136.
308. V. Sharma, G. Harith, S. Kumar, R. Sharma, K. L. Reddy, A. Bahuguna and V. Krishnan, *Mater Technol*, 2017, **32**, 461-471.
309. Y. Tian and T. Tatsuma, *J Am Chem Soc*, 2005, **127**, 7632-7637.
310. H. J. Yan, S. T. Kochuveedu, L. N. Quan, S. S. Lee and D. H. Kim, *J Alloy Compd*, 2013, **560**, 20-26.
311. Q. Wang, M. M. Chen, N. X. Zhu, X. D. Shi, H. Jin, Y. Zhang and Y. Q. Cong, *J Colloid Interf Sci*, 2015, **448**, 407-416.
312. S. Buddee and S. Wongnawa, *J Sol-Gel Sci Techn*, 2015, **75**, 152-163.
313. A. S. Vorokh, N. S. Kozhevnikova, T. I. Gorbunova, O. I. Gyrdasova, I. V. Baklanova,

L. Y. Buldakova, M. Y. Yanchenko, A. M. Murzakaev, E. V. Shalaeva and A. N. Enyashin, *J Alloy Compd*, 2017, **706**, 205-214.
314. S. C. Roy, O. K. Varghese, M. Paulose and C. A. Grimes, *Acs Nano*, 2010, **4**, 1259-1278.
315. M. Y. Xing, Y. Zhou, C. Y. Dong, L. J. Cai, L. X. Zeng, B. Shen, L. H. Pan, C. C. Dong, Y. Chai, J. L. Zhang and Y. D. Yin, *Nano Lett*, 2018, **18**, 3384-3390.
316. H. Li, J. Shang, Z. H. Ai and L. Z. Zhang, *J Am Chem Soc*, 2015, **137**, 6393-6399.
317. M. S. Palmer, M. Neurock and M. M. Olken, *J Am Chem Soc*, 2002, **124**, 8452-8461.
318. Y. Tamaura and M. Tabata, *Nature*, 1990, **346**, 255-256.
319. S. N. Habisreutinger, L. Schmidt-Mende and J. K. Stolarczyk, *Angew Chem Int Edit*, 2013, **52**, 7372-7408.
320. G. H. Yin, Q. Y. Bi, W. Zhao, J. J. Xu, T. Q. Lin and F. Q. Huang, *Chemcatchem*, 2017, **9**, 4389-4396.
321. B. Wang, X. H. Wang, L. Lu, C. G. Zhou, Z. Y. Xi, J. J. Wang, X. K. Ke, G. D. Sheng, S. C. Yan and Z. G. Zou, *Acs Catal*, 2018, **8**, 516-525.
322. L. D. Li, J. Q. Yan, T. Wang, Z. J. Zhao, J. Zhang, J. L. Gong and N. J. Guan, *Nat Commun*, 2015, **6**, 5881.
323. F. C. Lei, Y. F. Sun, K. T. Liu, S. Gao, L. Liang, B. C. Pan and Y. Xie, *J Am Chem Soc*, 2014, **136**, 6826-6829.
324. X. Y. Xin, T. Xu, L. Wang and C. Y. Wang, *Sci Rep-Uk*, 2016, **6**, 23684.
325. F. Fresno, P. Renones, E. Alfonso, C. Guillen, J. F. Trigo, J. Herrero, L. Collado and V. A. D. O'Shea, *Appl Catal B-Environ*, 2018, **224**, 912-918.
326. G. Yin, M. Nishikawa, Y. Nosaka, N. Srinivasan, D. Atarashi, E. Sakai and M. Miyauchi, *Acs Nano*, 2015, **9**, 2111-2119.
327. A. Razzaq, A. Sinhamahapatra, T. H. Kang, C. A. Grimes, J. S. Yu and S. I. In, *Appl Catal B-Environ*, 2017, **215**, 28-35.
328. R. G. Hennig, P. A. Fedders and A. E. Carlsson, *Phys Rev B*, 2002, **66**.
329. F. Spiegelman, N. Tarrat, J. Cuny, L. Dontot, E. Posenitskiy, C. Marti, A. Simon and M. Rapacioli, *Adv Phys-X*, 2020, **5**.
330. J. Mavracic, F. C. Mocanu, V. L. Deringer, G. Csanyi and S. R. Elliott, *J Phys Chem Lett*, 2018, **9**, 2985-2990.
331. Z. H. Stachurski, *Materials*, 2011, **4**, 1564-1598.